



**THE EXPERIMENTAL AND NUMERICAL
INVESTIGATION OF THE STRUCTURAL
PERFORMANCE OF A 3D RC FRAME BUILT USING A
RC FORMWORK SYSTEM**

Quy Thue NGUYEN



T.C.
ULUDAG UNIVERSITY
GRADUATE SCHOOL OF NATURAL AND APPLIED SCIENCES

**THE EXPERIMENTAL AND NUMERICAL INVESTIGATION OF THE
STRUCTURAL PERFORMANCE OF A 3D RC FRAME BUILT USING A RC
FORMWORK SYSTEM**

Quy Thue NGUYEN

Asst.Prof.Dr. Serkan SAĐIROĐLU
(Advisor)

A MASTER OF SCIENCE THESIS
DEPARTMENT OF CIVIL ENGINEERING

BURSA-2018

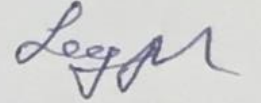
THESIS APPROVAL

A thesis study titled "The Experimental and Numerical Investigation of The Structural Performance of a 3D RC Frame Built Using a RC Formwork System" prepared by Quy Thue NGUYEN was accepted as **A MASTER'S THESIS** by Uludag University Graduate School of Natural and Applied Sciences, Department of Civil Engineering with the following jury.

Advisor : Asst.Prof.Dr. Serkan SAĞIROĞLU

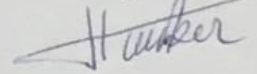
Chairman: Asst.Prof.Dr. Serkan SAĞIROĞLU
Uludağ University
Faculty of Engineering,
Department of Civil Engineering

Signature



Member : Assoc.Prof.Dr. Hakan T. TÜRKER
Uludağ University
Faculty of Engineering,
Department of Civil Engineering

Signature

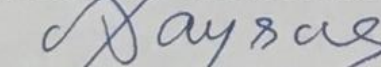


Member : Asst.Prof.Dr. A. Utku YAZGAN
Maltepe University
Faculty of Engineering,
Department of Civil Engineering

Signature



I confirm the above results.



Prof. Dr. Ali BAYRAM

Institute Director

28.12.2018

My thesis has been prepared based to the thesis writing rules of Uludag University Graduate School of Natural and Applied Sciences;

I declare,

- all of information and documents are obtained according to academic rules,
- visual, auditory and written information and results in accordance with the scientific code of ethics,
- in the case that the works of others are used, I referred to those works in accordance with the scientific norms,
- all of referred resources are shown in the reference section,
- I have not falsified the data used,
- I do not submit any part of this thesis at this university as well as different universities as a thesis.

07/08/2018

Quy Thue NGUYEN



ABSTRACT

MSc Thesis

THE EXPERIMENTAL AND NUMERICAL INVESTIGATION OF THE STRUCTURAL PERFORMANCE OF A 3D RC FRAME BUILT USING A RC FORMWORK SYSTEM

Quy Thue NGUYEN

Uludağ University
Graduate School of Natural and Applied Sciences
Department of Civil Engineering

Supervisor: Asst.Prof.Dr. Serkan SAĞIROĞLU

The effect of using reinforced concrete (RC) formwork system on the static and dynamic structural performance of a three dimensional RC frame is evaluated experimentally and numerically. A single story RC frame that is symmetric in both directions poured using RC formworks, called New Frame (NF) is compared to a reference frame built traditionally, namely Classical Frame (CF). Firstly, the dynamic characteristics of NF is compared with those of CF based on results obtained by shaker test and by modal analysis using finite element method (FEM) in Abaqus CAE. There is no significant deviation between two frames in terms of natural vibration frequencies as well as mode shapes. Secondly, static nonlinear pushover analysis (SNPA), particularly monotonic pushing, is carried out in order to determine the performance point of RC frames. Under a considered seismic condition, NF performs a lower value of spectral acceleration, about 86% of that of CF. Besides that the maximum displacement of NF exceeds the collapsed point of CF approximately 27%. Thirdly, two surface treatment methods consisting of steel shear connectors and rectangular shaped asperities are applied in order to enhance the shear capacity of inter-concrete substrates. The flexural strength of NF is improved about 12% applying a suitable ratio of shear links, about 0,48%. On the other hand, the bending capacity of NF using rectangular irregularities (5mm high 37,5mm wide and 37,5mm apart) is equal to 1,206 times the capacity of NF with smooth surfaces. Finally, the influence of normal load in columns on the inelastic behavior of studied structures is also examined in the present thesis. It is observed that larger normal force in columns upgrades the flexural behavior of structures but results in a performance point with a lower spectral acceleration value.

Key words: concrete-to-concrete interface, modal analysis, pushover analysis, Coulomb friction theory

2018, xii + 139 pages.

ÖZET

Yüksek Lisans Tezi

BETONARME KALIP SİSTEMİ KULLANILARAK İNŞA EDİLMİŞ BİR 3 BOYUTLU BETONARME ÇERÇEVENİN YAPISAL PERFORMANSININ DENEYSSEL VE SAYISAL OLARAK İNCELENMESİ

Quy Thue NGUYEN

Uludağ Üniversitesi
Fen Bilimleri Enstitüsü
İnşaat Mühendisliği Anabilim Dalı

Danışman: Dr.Öğr.Üye. Serkan SAĞIROĞLU

Betonarme (BA) kalıp sisteminin üç boyutlu bir BA çerçevenin statik ve dinamik yapısal performansına etkisi, deneysel ve sayısal olarak değerlendirilmiştir. BA kalıplar kullanılarak her iki yönde simetrik ve tek katlı olarak dökülen ve yeni çerçeve (YÇ) olarak adlandırılan BA çerçeve, klasik yöntemlerle inşa edilen ve klasik çerçeve (KÇ) olarak adlandırılan referans çerçevesi ile karşılaştırılmıştır. İlk olarak, YÇ'nin dinamik karakteristikleri, sarsma testinden elde edilen sonuçlar ve Abaqus CAE'de sonlu elemanlar metodu (SEM) kullanılarak yapılan modal analizden elde edilen sonuçlar kullanılarak, KÇ ile karşılaştırılmıştır. Doğal titreşim frekansları ve mod şekilleri bakımından iki çerçeve arasında önemli bir fark yoktur. İkinci olarak, BA çerçevelerin performans noktasını belirlemek için, doğrusal olmayan statik itme analizi (DOSİA), özellikle monotonik itme, ile gerçekleştirilmiştir. Gözönüne alınan sismik koşul altında, YÇ, KÇ'nin yaklaşık %80'i oranında daha düşük bir spektral ivme değeri vermektedir. Bunun yanı sıra, YÇ'nin maksimum yer değiştirmesi, KÇ'nin göçme noktasını yaklaşık %27 aşmaktadır. Üçüncüsü, beton yüzeyler arası kesme kapasitesini arttırmak için çelik kesme elemanları ve dikdörtgen şekilli pürüzlendirmeden oluşan iki yüzey işleme yöntemi uygulanmıştır. YÇ'nin eğilme kapasitesi, çelik kesme elemanlarının yaklaşık %0,48 gibi uygun bir oranda uygulanmasıyla yaklaşık %12 oranında geliştirilebilmektedir. Diğer taraftan, dikdörtgen yüzey pürüzleri (3,5 mm yüksekliğinde 35mm genişliğinde ve 35mm aralıklı) kullanılarak yapılan YÇ'nin eğilme kapasitesi, düz yüzeyli YÇ'nin 1,206 katına eşittir. Son olarak, kolonlardaki normal yükün çalışılan yapıların elastik olmayan davranışları üzerine etkisi de bu tezde incelenmiştir. Kolonlardaki normal kuvvet arttıkça, yapıların eğilme davranışının iyileştiği, ancak daha düşük bir spektral ivme değerine sahip bir performans noktası elde edildiği gözlemlenmiştir.

Anahtar kelimeler: beton-beton arayüzü, modal analiz, itme analizi, Coulomb sürtünme teorisi

2018, xii + 139 sayfa.

ACKNOWLEDGEMENT

To Asst.Prof.Dr. Serkan SAĐIROĐLU, my thesis supervisor, for his great guidance from the first day my master course was initiated in Department of Civil Engineering, Uludađ University, Bursa, Turkey.

To Prof. Dr. Ramazan LIVAOĐLU, my teacher, for his teaching and guiding me during my graduate education in Uludađ University.

To my teachers in the department who have given me valuable lessons in class as well as helped me a lot in living in Turkey. Besides that, the dissertation is benefited from TR 2011 01550 B patent of Turkish Patent Institute when taking advantage of the idea of applying reinforced concrete formworks on building new structures.

To T.C. Bařbakanlık Yurtdıřı Trkler ve Akraba Topluluklar Bařkanlıđı who sponsors me a tremendous chance to study and experience an interesting life in Turkey.

To my friends whom I met in Turkey, especially my brother Numan, always are beside me in any situation.

To my family, to Du and to Horse.

QUY THUE NGUYEN
07/08/2018

TABLE OF CONTENTS

	Page
ABSTRACT.....	i
ÖZET.....	ii
ACKNOWLEDGEMENT	iii
TABLE OF CONTENTS.....	iv
LIST OF SYMBOLS AND ABBREVIATIONS	vi
LIST OF FIGURES	x
LIST OF TABLES	xii
1. INTRODUCTION	1
1.1. Classical Kinds of Formwork	1
1.2. RC Formwork System.....	2
2. THEORETICAL BACKGROUND AND LITERATURE REVIEW	4
2.1. Theoretical Background.....	4
2.1.1. Friction	4
2.1.2. Concrete-to-concrete interface	10
2.1.3. Modal analysis	21
2.1.4. Concrete damage plasticity model	29
2.1.5. Nonlinear performance of existing structure	33
2.1.6. Finite element method – ABAQUS CAE	43
2.2. Literature Review.....	46
3. METHODOLOGY AND APPROACH	65
3.1. Geometrics of Specimen	65
3.2. Materials	66
3.2.1. Concrete	66
3.2.2. Steel reinforcement	69
3.3. The Concrete-to-concrete Interface	70
3.3.1. The left as –cast interface.....	70
3.3.2. Formulation of friction model in Abaqus	72
3.4. Natural Dynamic Characteristics of Structures.....	73
3.4.1. Shaker test.....	73
4. RESULTS AND DISCUSSION	77
4.1. Shaker Test.....	77
4.2. Modal Analysis-FEM.....	79
4.2.1. Assembly.....	80
4.2.2. Step selection	81
4.2.3. Meshing.....	81
4.2.4. Results of model analysis.....	81
4.3. Discussion of Natural Properties.....	82
4.4. Base Shear-Displacement Curve – FEM	84
4.4.1. Left as-cast concrete-to-concrete interface	84
4.4.2. Application of surface treatment methods	88
4.5. Performance Point.....	97
4.5.1. Selection a specific seismic conditions	97
4.5.2. Determination of performance point.....	98
4.6. The Influence of The Intensity of Normal Load on Performance Point.....	103
4.6.1. Flexural capacity	104

4.6.2. Performance point.....	107
4.7. Discussion.....	119
5. CONCLUSION.....	121
REFERENCES.....	122
APPENDICES.....	127
APPENDIX A. Dynamic Characteristics.....	128
APPENDIX B. Data of Pushover Curve and Capacity Spectrum.....	131
RESUME.....	139



LIST OF SYMBOLS AND ABBREVIATIONS

Symbols	Description
a	Acceleration
a	Distance
A	Cross sectional area
A_{vf}	Area of shear-friction reinforcement
b	Overall width of cross-section
c	Cohesion
c	Cohesion coefficient of concrete
c	Damping coefficient
c	Length of distributed normal stress
c_{cr}	Critical damping coefficient
c_o	Apparent cohesion intercept
d	Diameter
d	Height of asperity
d	The cohesion of the material
D	Damaged stiffness
d_c	Damage parameter in compression of concrete
d_t	Damage parameter in tension of the concrete
D_o	Initial stiffness
DOF	Degree of freedom
E	Elastic modulus
E_{cit}	Initial modulus of normal weight concrete
E_s	Design value of modulus of elasticity of reinforcing steel
EI	Bending stiffness
f	Frequency
f_{bo}	The initial equi-biaxial compressive stress
F	Force
f_c	Critical stress
f_{co}	Uniaxial compressive yield stress
f_{cd}	Design value of concrete compressive strength
f_{ck}	Characteristic cylinder compressive strength of concrete at 28 day age
f_{ctd}	Design value of concrete tensile strength
f_{ctk}	Characteristic axial tensile strength of concrete
f_D	Damping force
F_g	Gravitational force
f_k	Kinetic friction force
f_I	Inertia force
F_N	Normal force on surfaces
f_s	Friction force
f_s	Stress strength of steel
f_s	Internal resistant force

f_y	Specified yield strength of reinforcement
f_{yd}	Design yield strength of reinforcement
g	Gravitational acceleration
G	Young elastic modulus in shear
h	Height
h_1, h_2	Dimensions of asperity
i	The inclination of “saw teeth”
I	Second moment of area of concrete section
I_1	The first invariant of stress
J_2	The second invariant of the stress deviator
k	Flexural stiffness
k	Spring stiffness
K	Coefficient
$k_{\text{composite}}$	Flexural stiffness of composite element
k_{mon}	Flexural stiffness of monotonic element
L	Length
l_a	Asperity length
m	Mass
N	Normal load
N_{ed}	Design value of the applied axial force (tension or compression)
p	External force
p	Normal pressure
P_i	Total gravity load at story i
(p,q)	Meridional plane
S	First moment of area
S	Shearing strength
S_f	Slip of bond
T	Period
T	Torsional moment
u	Lateral displacement
u_g	Ground motion
V	Shear force
v_a	Shear resistance of the aggregate interlock mechanism
v_c	Shear resistance by normal clamping stress
v_D	Shear resistance by dowel action
V_{ed}	Design value of the applied shear force
V_i	Total calculated lateral shear force in story i
V_{max}	Shearing capacity
v_n	Nominal shear strength
V_{Rdi}	The design shear resistance at the interface
V_u	Factored shear force at section
W_{cr}	Width of crack in bond
x,y,z	Components of Cartesian coordinate
α	Angle defining the orientation of reinforcement

α	Aspect ratio of asperity
α, β, γ	Experimental parameters dependent on f_{bo}/f_{co}
$\alpha_{critical}$	Critical aspect ratio
β	Angle
β	The material friction angle
β_P	unconfined uniaxial compressive strength
γ	Shearing strain
ϵ_c	Compressive strain in the concrete
ϵ_{cu}	Ultimate compressive strength in the concrete
ϵ_t	Tensile strain in the concrete
ϵ_c^{el}	Damaged elastic strain in the concrete
ϵ_{oc}^{el}	Undamaged elastic strain in the concrete
ϵ_{ot}^{el}	Undamaged elastic strain in the concrete
ϵ_t^{el}	Damaged elastic strain in the concrete
$\tilde{\epsilon}_c^{in}$	Crushing strain in the concrete
$\tilde{\epsilon}_c^{pl}$	Plastic strain in the concrete
$\tilde{\epsilon}_t^{ck}$	Cracking strain in the concrete
$\tilde{\epsilon}_t^{pl}$	Plastic strain in the concrete
ϵ_t	Tensile strain in the concrete
ξ	Damping factor
ϵ	Eccentricity
θ	Angle
κ	Plastic-damage variable
κ	Young modulus of concrete in shear
μ	Constant coefficient of friction
μ	Ductility factor
μ_k	Kinetic coefficient of friction
μ_s	Static coefficient of friction
ν	Poisson's ratio
ν	Strength reduction factor for concrete cracked in shear
ρ	Over-dry density of concrete
ρ_s	Shear connector ratio
ρ_t	Reinforcement ratio for longitudinal reinforcement
σ	Normal stress on surfaces
σ_c	Compressive stress in the concrete
σ_{cu}	Ultimate compressive strength in the concrete
σ_{co}	Yield stress in the concrete
σ_n	Constant normal stress
σ_N	Normal clamping stress
σ_s	Tensile stress in the steel shear connector
σ_t	Tensile stress in the concrete
σ_{to}	Failure stress in the concrete

σ_y	Yield stress
$\bar{\sigma} _o$	The initial yield stress
τ	Shear stress
τ	Shearing capacity due to normal stress σ_n
τ_{oct}	Shear stress on octahedral plane/deviatory plane
τ_1, τ_2	Shear stress components at a same point
τ_{crit}	Critical shear stress
τ_{eq}	Equivalent shear stress
τ_{max}	Maximum shear stress
$\bar{\tau}_{max}$	Limit of critical shear stress
ϕ	Phase lag
ϕ_f	The peak friction angle
ϕ_μ	the angle of sliding frictional resistance
ϕ_r	The angle of residual shearing resistance
ψ	Dilative angle
ω	Frequency
Φ_n	n^{th} natural mode

Abbreviations	Description
CDPM	Concrete damage plasticity model
CF	Classical frame
CFRP	Carbon fiber reinforced polymer
CM	Compressive meridian
DOF	Degree of freedom
FRFs	Frequency response functions
MPA	Modal pushover analysis
NF	New frame
NPA	Nonlinear Pushover Analysis
NTHA	Nonlinear time history analysis
RC	Reinforced concrete
SDOF	Single degree of freedom
SLS	Serviceability limit state
TM	Tensile meridian
ULS	Ultimate limit state

LIST OF FIGURES

	Page
Figure 1.1. Classical kinds of formwork. PLYTEC formwork (2016)	1
Figure 1.2. Prefabricated products. A-Z PREZIP a.s. (2014)	2
Figure 1.3. An overview of RC formworks	3
Figure 2.1. Assembles of friction in Leonardo da Vinci’s notebooks. Walker (2007).....	4
Figure 2.2. Assembles of friction in Leonardo da Vinci’s notebooks. Walker (2007).....	5
Figure 2.3. Basic Coulombic friction model.....	7
Figure 2.4. The critical shear stress of Coulomb friction model. (a) without; and (b) with a limitation of shear stress. Dassault Systèmes (2013)	8
Figure 2.5. Apparent analogy between friction and plasticity. Drucker (1953)	9
Figure 2.6. Sticking and slipping friction. Dassault Systèmes (2013).....	9
Figure 2.7. Delaminating stress. Gromysz (2008)	10
Figure 2.8. Strain diagram of a composite section. (a) Unconnected, (b) Fully connected joint, and (c) Partly connected joint. Thermou (2015).....	11
Figure 2.9. Stiffness degradation of a composite beam. Gromysz (2008).....	12
Figure 2.10. Shear-friction mechanism. Thermou (2015)	13
Figure 2.11. Shear-friction concept. ACI 318-08 (2008).....	14
Figure 2.12. Inclined shear- friction reinforcement. ACI 318-08 (2008)	16
Figure 2.13. Different types of irregularities along interface surfaces. Patton (1966) ...	16
Figure 2.14. Shearing resistance. (a) Flat; and (b) Teeth shaped surface. Patton (1966)	17
Figure 2.15. Failure envelopes for specimens with different inclinations of teeth. Patton (1966).....	18
Figure 2.16. Shear mechanisms of rectangular shaped irregularity. (a) dilative failure; and (b) non-dilative failure. Kwon et al. (2009)	19
Figure 2.17. Indented construction joint. EN 1992-1-1 (2004)	20
Figure 2.18. An approach to modal analysis.....	22
Figure 2.19. Overview of oscillation. Peter (2001)	23
Figure 2.20. Overview of oscillation. Peter (2001)	23
Figure 2.21. Overlay the frequency trace with time trace. Peter (2001).....	24
Figure 2.22. FRFs and relative shapes. Peter (2001)	24
Figure 2.23. Example of multi degree of freedom systems. Chopra (2012).....	26
Figure 2.24. Mode shapes of a MDOF structure. Chopra (2012)	26
Figure 2.25. Test setup. Peter (2001)	27
Figure 2.26. Frequency response function. (a) Magnitude, (b) Phase lag , c) Real and d) Imaginary part. Peter (2001)	28
Figure 2.27. Waterfall plot of beam frequency response functions. Peter (2001)	29
Figure 2.28. Elastic degradation in tension (a) and compression (b) Dassault Systèmes (2013).....	30
Figure 2.29. Complete stress-strain behavior of concrete. (a) In compression. Hsu and Hsu (1994) (b) In tension. Aslani and Jowkarmeimandi (2012)	32
Figure 2.30. Transformation from $V_b-\Delta$ to S_a-S_d	36
Figure 2.31. Demand spectrum. (a) S_a-T (b) S_a-S_d . ATC 40 (1996).....	39
Figure 2.32. Construction of a 5 %-damped elastic response spectrum. ATC 40 (1996)	39
Figure 2.33. Original 5% damped and reduced response spectrum. ATC 40 (1996)	40
Figure 2.34. Bilinear representation of capacity spectrum for capacity spectrum method.	

ATC 40 (1996).....	42
Figure 2.35. Performance point determination. ATC 40 (1996).....	42
Figure 2.36. Nodes and elements of a gear tooth. Robert (1994)	44
Figure 2.37. Outline of FE analysis project. Robert (1994).....	45
Figure 2.38. Suite of finite element analysis modules. Dassault Systèmes (2013)	45
Figure 2.39. A modeling process in Abaqus. Dassault Systèmes (2013).	46
Figure 3.1. Finished dimensions of symmetric frames and cross sections in mm.....	66
Figure 3.2. Elastoplastic model of steel	70
Figure 3.3. RC formworks for bases, columns, and beams. (a) Preparation; (b) Products.	74
Figure 3.4. Pouring concrete into the RC formworks. (a) Formwork installation; (b) Pouring concrete; and c) Product.	74
Figure 3.5. Formwork installation of columns and beams.....	75
Figure 3.6. The working space of two frames when waiting for the age of concrete.	75
Figure 3.7. The working space of two frames when waiting for the age of concrete.	76
Figure 4.1. The frequency response function of Classical Frame respect to (a) x direction (b) z direction.....	78
Figure 4.2. The frequency response function of New Frame respect to (a) x direction; (b) z direction.	79
Figure 4.3. Components of NF. (a) Finished position of formworks; (b) Core part.....	80
Figure 4.4. Localization of reinforced steel in NF.....	80
Figure 4.5. Mode Shapes for classical frame. (a) Mode 1: 19,88 Hz (b) Mode 2: 19,88 Hz c) Mode 3: 25,02 Hz.....	81
Figure 4.6. Mode Shapes for new frame. (a) Mode 1: 19,85 Hz (b) Mode 2: 19,85 Hz c) Mode 3: 24,95 Hz.	82
Figure 4.7. Pushover analysis procedure.	84
Figure 4.8. Flexural behavior of CF and NF.....	87
Figure 4.9. Π shaped steel connectors. (a) Predetermined location; (b) Detailed dimensions in mm.	90
Figure 4.10. Application of Π shaped shear links. (a) on columns; and (b) on RC formwork.....	91
Figure 4.11. Flexural behavior of NF with connectors in compared with CF and NF. ..	91
Figure 4.12. Percentage of enhancement of shear connectors	92
Figure 4.13. Properties of irregularities.	95
Figure 4.14. Atomic view of saw teeth. (a) On elements; (b) On formworks; and (c) On frame.	95
Figure 4.15. Flexural behavior of NF with connectors in compared with CF and NF. ..	96
Figure 4.16. 5% Damped elastic response spectrum of Soil S_a . (a) S_a versus T; and (b) ADRS format.	98
Figure 4.17. Performance Point. (a) CF; (b) NF; (c) NF_048; and (d) NF_5TEETH .	101
Figure 4.18. Drift Comparison.....	102
Figure 4.19. Flexural performance. (a) CF series (b) NF series (c) a comparison	105
Figure 4.20. ADRS. (a) CFs; (b) NFs; and (c) an overall comparison	109
Figure 4.21. Performance Point. (a) CF_123 (b) CF_219 (c) CF_336	113
Figure 4.22. Performance Point. (a) NF_123 (b) NF_219 (c) NF_336	114
Figure 4.23. A comparison of performance point.....	116

LIST OF TABLES

	Page
Table 2.1. Soil Profile Types, ATC 40 (1996).....	36
Table 2.2. Seismic Zone Factor (Z). ATC 40 (1996).....	37
Table 2.3. Near Source Factor (N_A) and (N_V), ATC 40 (1996).....	37
Table 2.4. Seismic Source Type, ATC 40 (1996).....	37
Table 2.5. Seismic Coefficient (C_A), ATC 40 (1996).....	38
Table 2.6. Seismic Coefficient (C_V), ATC 40 (1996).....	38
Table 2.7. Minimum allowable SR_A and SR_V values, ATC 40 (1996).....	40
Table 2.8. Values for damping modification factor κ , ATC 40 (1996)	41
Table 2.9. Values for damping modification factor κ , ATC 40 (1996)	41
Table 2.10. Deformation Limits, ATC 40 (1996).....	43
Table 3.1. Mechanical properties of concrete material.....	66
Table 3.2. Proposed Abaqus input parameters of B35 concrete.	67
Table 3.3. Input parameters for CDPM	69
Table 3.4. Mechanical properties of steel	70
Table 3.5. Friction coefficient of concrete-to-concrete interface.....	71
Table 3.6. Parameters of the modified Coulombic friction model.....	72
Table 4.1. A comparison of dynamic characteristics	82
Table 4.2. FE models applied shear connectors.....	90
Table 4.3. Summary of seismic parameters.	97
Table 4.4. Performance Point Determination.....	99
Table 4.5. Performance Points	110

1. INTRODUCTION

1.1. Classical Kinds of Formwork

Formworks play an important role in forming the shape of structures and supporting concrete until reaching the required strength. Firstly, the shape and dimensions of structural elements such as columns, beams, slabs, and walls etc. are flexible so that they can be formed easily by using wood, steel or plastic formworks (Figure 1.1). Moreover, reinforced concrete (RC) structures poured in construction sites directly considered to work more effectively than buildings constructed by prefabricated elements due to the monolithic property. However, the common method has some disadvantages.



Figure 1.1. Classical kinds of formwork. PLYTEC formwork (2016)

Low quality of workmanship may cause erroneous dimensions in comparison with designed ones. As a result, the structures behave differently from the original design and the worst situation is that the built structures can collapse prematurely compared with the designed strength. Secondly, for the economic aspect, the cost paid for workmanship at construction sites as well as for materials used for formwork should be taken into account. The workmanship comprises formwork installation and dismantling them. Finally, the workmanship for formwork may lead to some problems relevant to the environment.

The aforementioned limitation of in-situ poured RC buildings may possibly be solved using prefabricated products. The method is considered as quick and convenient (Figure 1.2). However, the capacity of a unified structure caused by weak joints is mainly questionable when using precast elements especially in earthquake prone sites.



Figure 1.2. Prefabricated products. A-Z PREZIP a.s. (2014)

1.2. RC Formwork System

RC formworks (Figure 1.3) not only play the same role as the classical types of formwork but also possibly solve the previous negative aspects of the traditional methods while still remaining somewhat of monolithic properties basing on the in-situ poured frame inside the RC formwork system. First of all, the RC formworks are prefabricated and controlled under strict conditions, especially the quality of concrete and the dimensions. The present method can also keep the quality of formworks at a certain level and save vast of time wasted for workmanship. Moreover, from the engineering point of view, only RC formworks are prefabricated while the frame poured in-situ is considered as a monolithic structure. Examining the integration of RC formworks with the monolithic frame under working conditions and the contribution of them to the capacity of structure under earthquake is the main target of the thesis. It is worth noting that under seismic events, slippage at interface surfaces causes lower capacity of structural elements as well as whole structures compared to monolithic ones.

Sliding resistance between substrates plays a decisive role in keeping the monolithic character of the structure. Particularly, the shear strength of the interconnection that is considered weakest when being left as cast (smooth) is possibly enhanced by applying surfaces treatment methods such as steel shear connectors and geometrically shaped asperities. It is worth reminding that the application of surface preparation can be prefabricated conveniently.

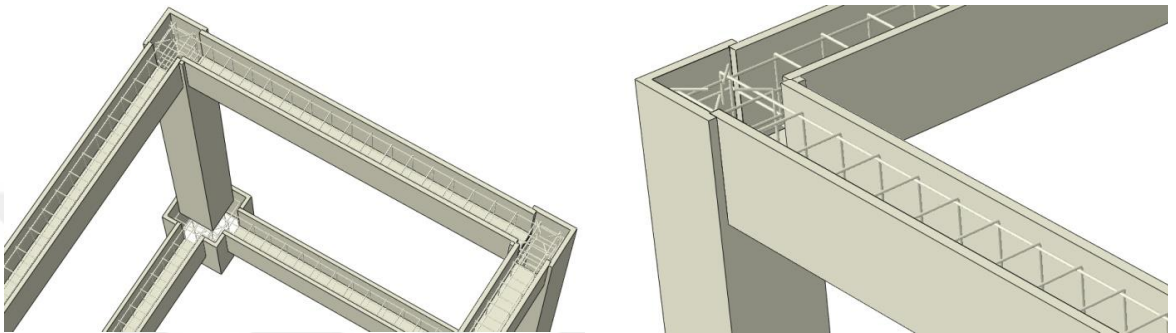


Figure 1.3. An overview of RC formworks

2. THEORETICAL BACKGROUND AND LITERATURE REVIEW

2.1. Theoretical Background

2.1.1. Friction

2.1.1.1. Developments of friction model

The presence of friction force is witnessed at the contact between dry solid surfaces when getting in touch with or without the occurrence of relative moving on each other. Leonardo da Vinci (1452–1519) found the first model of friction. The two fundamental laws of friction written in his notebooks (Figure 2.1) are reminded again by Hutchings (2016):

- The force of friction acting between two sliding surfaces is proportional to the load pressing the surfaces together (i.e. the forces have a constant ratio, often called the coefficient of friction), and
- The force of friction is independent of the apparent area of contact between the two surfaces.

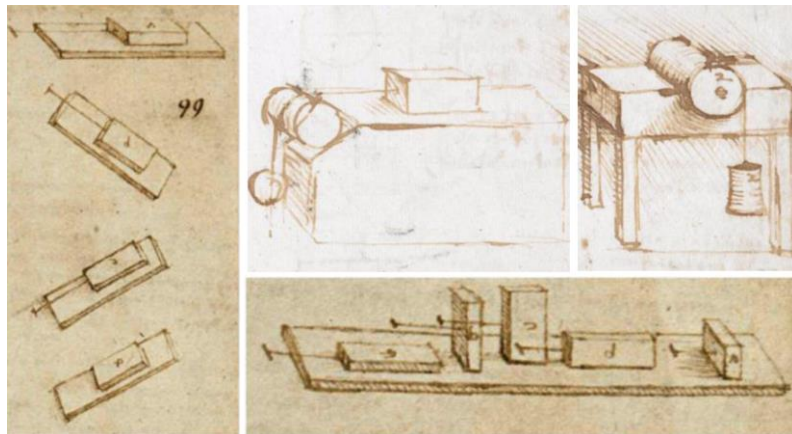


Figure 2.1. Assembles of friction in Leonardo da Vinci's notebooks. Walker (2007)

As previous authors, Walker (2007) divides friction into two regimes, widely known as static and kinetic friction force (Figure 2.2). Figure 2.2 illustrates step by step about the process from the appearance of a force, called friction force, and the transition into the kinetic regime from the static stage of the force. First of all, the friction force is zero in

Figure 2.2.a, the solid box gets balanced between the gravitational force F_g and the normal force at the surface F_N . In Figure 2.2.b, a lateral force F is applied from the value of zero in order to make the box moving relative to the surface. It is noted that the value of F is increased but is still assumed as small to move the box. At this moment, there is no lateral motion witnessed due to the fact that the box gets balanced not only in the vertical direction ($F_g = F_N$) but also horizontally by lateral force F and its opposing force appearing at the surface consequently, called static friction force f_s . The static friction force f_s increases in proportion to the increase of laterally applied force F to sustain the balanced condition of the box. The box breaks away as Figure 2.2.c and immediately initiates sliding relatively to the surface at the moment the static friction force f_s reaches a maximum value as shown in the ending point of the linear line in Figure 2.2.e.

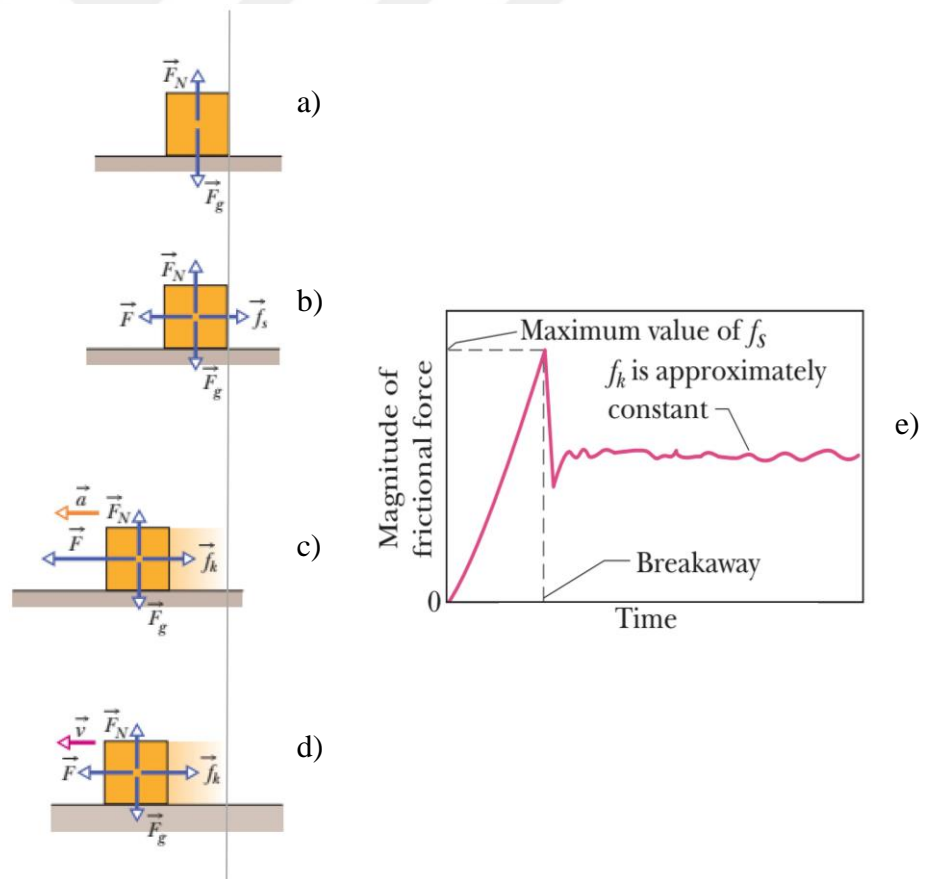


Figure 2.2. Assembles of friction in Leonardo da Vinci's notebooks. Walker (2007)

Afterward, the box starts usually moving stably with the lower value of the external applied force F considered as approximately constant throughout the time. The force f_k in the plateau regime of Figure 2.2.e balanced by the horizontal F is called kinetic friction force, f_k . It is noted that after accelerated at breakaway the box moves with a constant velocity as Figure 2.2.d under lower exerting force balancing the resulting kinetic friction force.

The magnitude of maximum static and approximate constant kinetic friction force at the interfacial contact between two dry and unlubricated bodies calculated based on empirical evaluation as:

$$f_{s,\max} = \mu_s F_N \quad (2.1)$$

$$f_k = \mu_k F_N \quad (2.2)$$

If the applied lateral force exceeds the static friction force in equation 2.1, the solid box starts moving and fall into the kinetic regime that the kinetic force and the magnitude of force needed to keep the horizontal motion as equation 2.2 is lower than the static peak. In other words, it is easier to keep the box sliding than attempt to pull it change into moving.

The coefficient of friction in both regimes, static and kinetic, is dependent on the property of both of surfaces, particularly the material at the interface substrates, the quality of surfaces etc. The frictional coefficients are determined by empirical tests. It is proved that the magnitude of frictional force depends on the magnitude of normal force perpendicular to the interfacial surface between two bodies according to Coulomb friction model.

2.1.1.2. Coulomb friction model

Coulomb establishes a simple model, so-called Coulomb friction model (Figure 2.3), in order to evaluate the friction force at the interface surface between two dry solids. Coulomb friction model independent on sliding velocity amplitude indicates only one

value of the magnitude of friction force, calculated as Equation 2.3, where the relative sliding is initiated.

$$f_s = \mu F_N \quad (2.3)$$

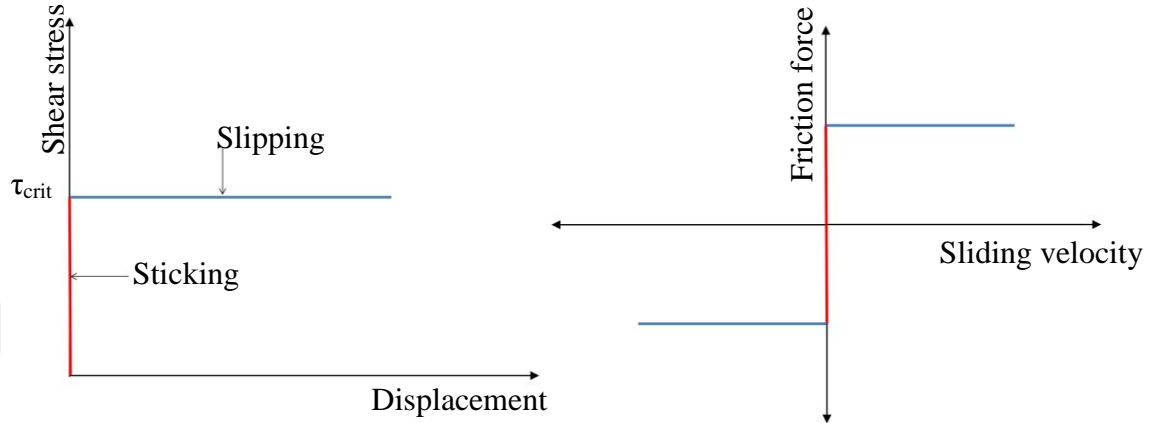


Figure 2.3. Basic Coulombic friction model

2.1.1.3. Modified Coulombic friction model

According to the isotropic Coulomb friction model (Figure 2.4), there is no relative movement until the equivalent shear stress τ_{eq} calculated considering two orthogonal components of shear stress as Equation 2.4 at interface contact reaches a critical value called critical stress.

$$\tau_{eq} = \sqrt{\tau_1^2 + \tau_2^2} \quad (2.4)$$

$$\tau_{crit} = \mu \sigma \quad (2.5)$$

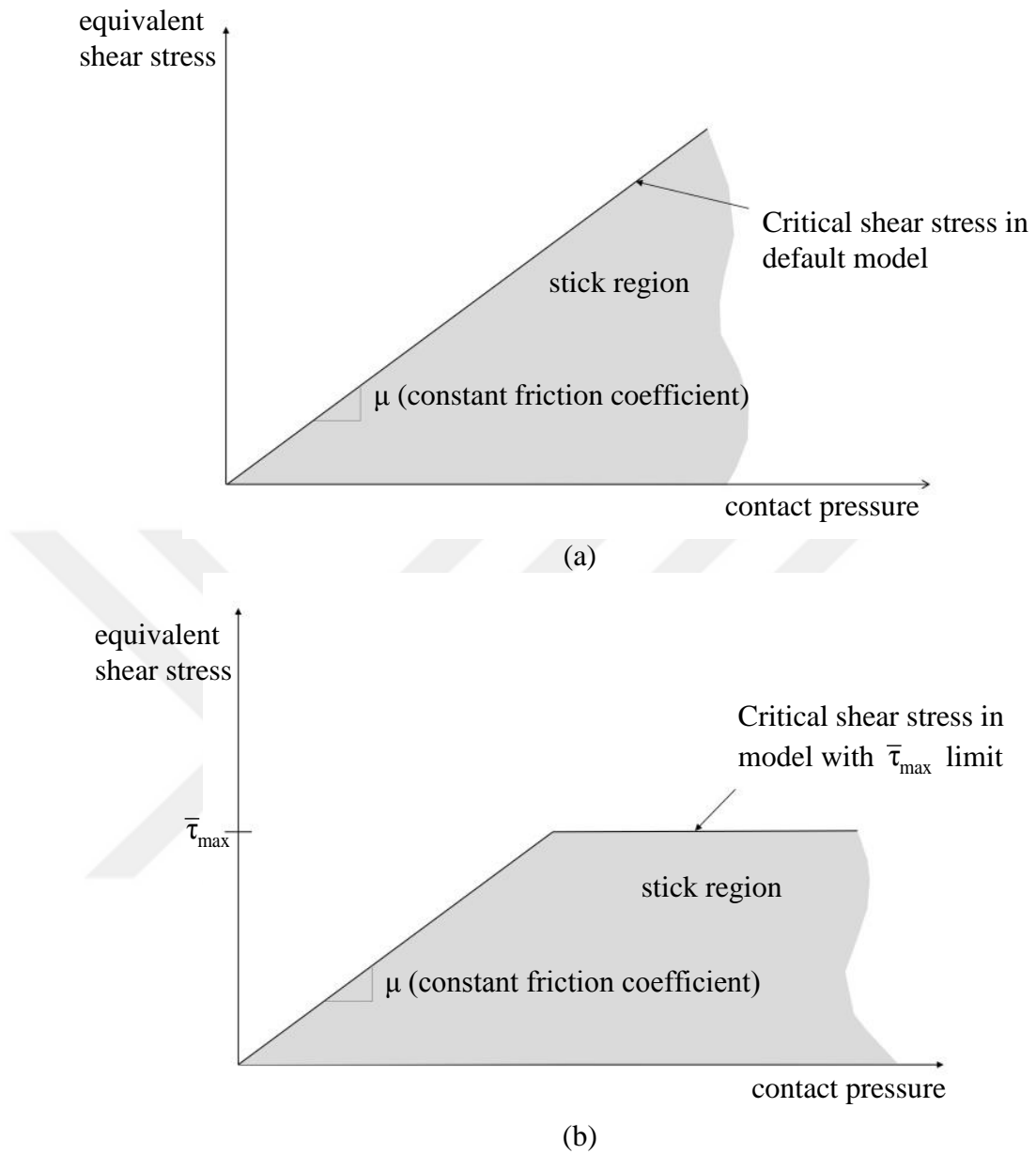


Figure 2.4. The critical shear stress of Coulomb friction model. (a) without (b) with a limitation of shear stress. Dassault Systèmes (2013)

Drucker (1953) warns a misleading when observing the similarity between the stress-strain relation for a rigid- or elastic-perfectly plastic material and the force-displacement relation for the Coulomb friction model (Figure 2.5).

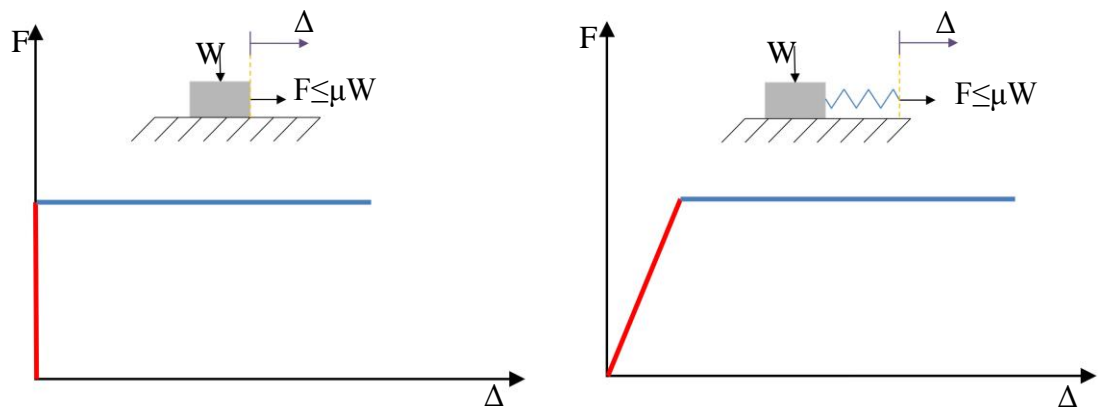


Figure 2.5. Apparent analogy between friction and plasticity. Drucker (1953)

Sticking friction and sliding friction are separated (Figure 2.6). In physics point of view, friction model accounts for sliding from the first moment of sliding seen. However, before that, initially, incremental slippage appears immediately with the presence of shear stress. In other words, although sticking as seen by eyes as the value of shear stress is less than the critical value as Figure 2.6, the micro slippage is still considered to initiate at any value of shear stress different from zero.

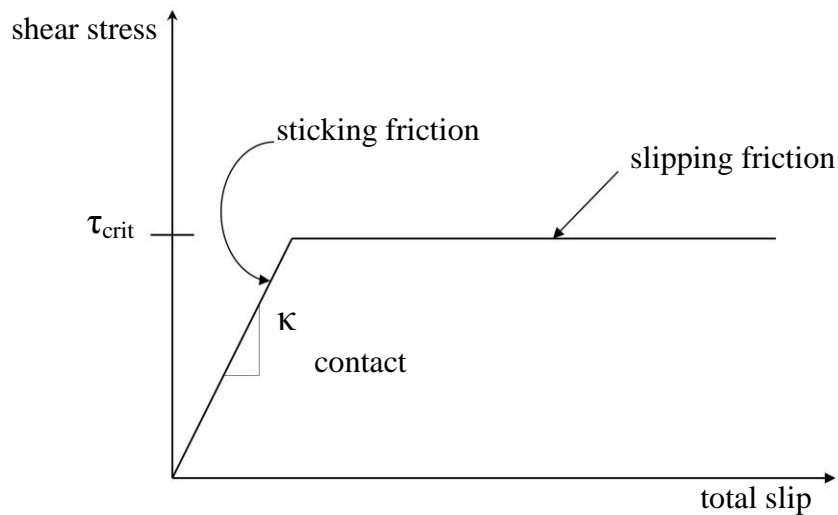


Figure 2.6. Sticking and slipping friction. Dassault Systèmes (2013)

2.1.2. Concrete-to-concrete interface

2.1.2.1. General behavior

From the strength of material point of view, a composite cross section can be considered as a monolithic section until the shear stress at the interface between substrates reaches a critical value, τ_{max} (Figure 2.7). The shear stress τ , also known as delaminating stress at interface surface between two different surfaces, is a resultant product of the shear force V acting on the section according to Equation 2.6 when the interface is acting elastically.

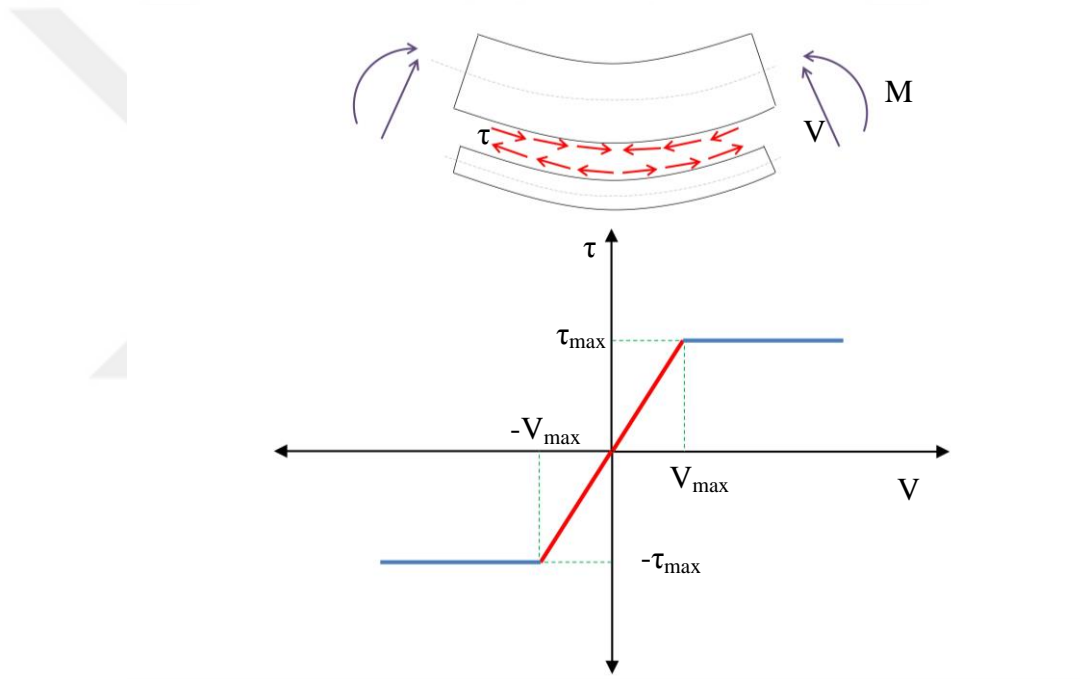


Figure 2.7. Delaminating stress. Gromysz (2008)

$$\tau = \frac{VS}{Ib} \quad (2.6)$$

At the moment the shear stress reaches the maximum magnitude τ_{max} corresponding to shear force V_{max} at the interface surfaces, the elastic regime quits. Gromysz (2008) indicates that after the moment of breakaway of two substrates, the shear stress at the interface surface does not exceed the value of τ_{max} regardless of the intensity of shear force V as shown in Figure 2.7.

The aforementioned Coulombic friction model is able to be applied to the concrete-to-concrete interface without or with surface treatments. The value of friction force representing the shear transferability of at the interfacial surface is dependent on the quality of surfaces that can be enhanced using surface treatment methods. Generally, the behavior of structural member including two concrete layers (Figure 2.8) is obviously different from a completely monolithic one and the deviation between them depends on the shearing strength, shear transferability in other words, at the concrete-to-concrete interface. The behavior of a section consisting of concrete substrates possibly alternatively falls into three situations as depicted in Figure 2.8:

- Unconnected joint, the composite section is divided into independent two components working separately as Figure 2.8.a,
- Partly connected joint, the composite section acts as two components but shear stress partially is somewhat transferred at the interface as depicted as Figure 2.8.c, and
- Fully connected joint, the composite section behaves thoroughly similarly to a monolithic section, it means all of shear stress is transferred completely as Figure 2.8.b.

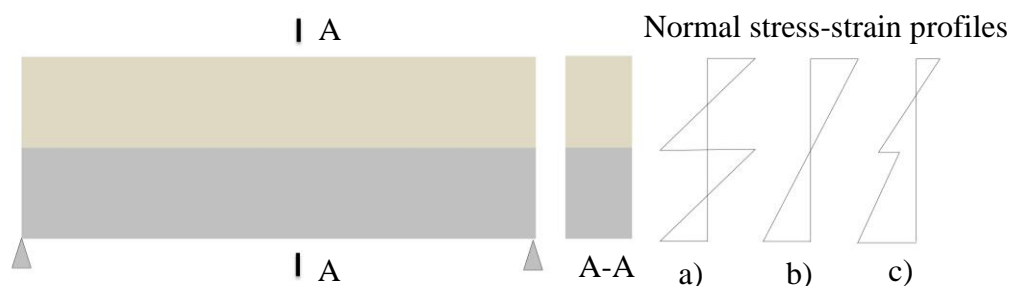


Figure 2.8. Strain diagram of a composite section. (a) Unconnected (b) Fully connected joint (c) Partly connected joint. Thermou (2015)

The shearing strength between concrete substrates decisively contributes to the bending stiffness of structural elements. Observe the behavior of composite beams focusing on the value of shear stress at the interface Gromysz (2008) also numerically indicates that after the initiation of delaminating stress the stiffness of the whole beam is degraded

(Figure 2.9). The occurrence of slippage means the loss of shear transferability at inter-concrete surfaces. Consequently, the structural beams work as composite elements instead of monolithically until the maximum value of shear stress is reached.

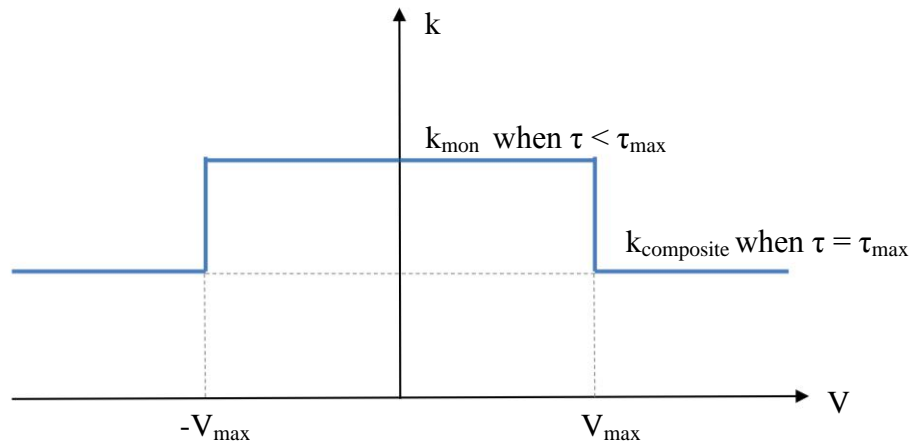


Figure 2.9. Stiffness degradation of a composite beam. Gromysz (2008)

It is highlighted saying that the shearing strength considered as the backbone of concrete-to-concrete joints has been improved using surface treatment methods in order to upgrade the shear transferability of the interface to aim at a monolithic behavior of structures. Firstly, in case of left as-cast concrete substrates, the stress transferability is represented by the value of friction coefficient whose value is in proportional to the quality of the interfacial surface classified as very smooth, smooth, rough, and very rock. In order to increase the friction coefficient, some surface preparations are applied such as wire-brushing, sand-blasting, shot-blasting, hydro-demolition, chipping, epoxy resins etc. In fact, these treatment methods possibly roughen the interface and increase the shearing strength. The friction coefficient is upgraded corresponding to applied methods and the intensity of the treatments. Secondly, another method used to upgrade the shear transferability of composite structural members is using bonding agents, commonly applied as shear connectors. Steel links crossing the concrete-to-concrete substrates contribute to the bonding strength through a mechanism, widely known as dowel action. The mechanical behavior of the concrete-to-concrete interface with or without the application of surface treatment method appears in literature and current

codes. Thirdly, the application of geometrically shaped irregularities, triangle or rectangular etc. at the inter-concrete substrates possibly increasing the monolithic behavior of composite members has been researched and stipulated in codes.

2.1.2.2. Application of shear connectors

The shear-friction theory assumes that the shearing strength of a concrete-to-concrete interface subjected simultaneously to shear and compressive stresses is ensured by friction only according to Santos and Júlio (2010). The author indicates that the shearing strength at interface surface generally depends on the compressive strength of the weakest concrete, normal stress at the interface, shear reinforcement crossing the interface, roughness of the substrate surface. The mechanism at the inter-concrete surface (Figure 2.10) illustrates that the existence of cracking at interface surface between two substrates results in tension in connectors and the compression is transferred by friction due to dowel action.

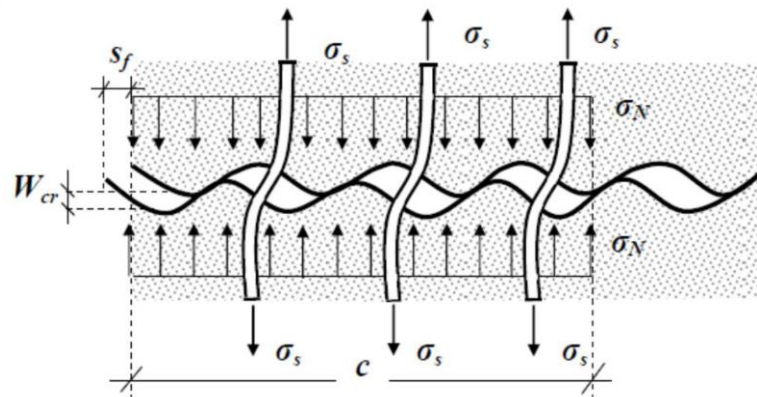


Figure 2.10. Shear-friction mechanism. Thermou (2015)

The shear friction concept also appears in ACI 318-08 (2008). The shear friction concept assumes that the crack happens at an expected location, particularly at the planar interface (Figure 2.11). Slippage initiates along the assumed crack. The roughness of the interface forces the opposing faces of the crack to separate. However, the shear friction reinforcement tends to prevent the separation. The occurrence of separation causes tension inside connectors. The tension gets balanced to the normal

clamping stress acting in its opposite direction. The clamping stress contributes to the frictional force parallel to the assumed crack to resist further slippage.

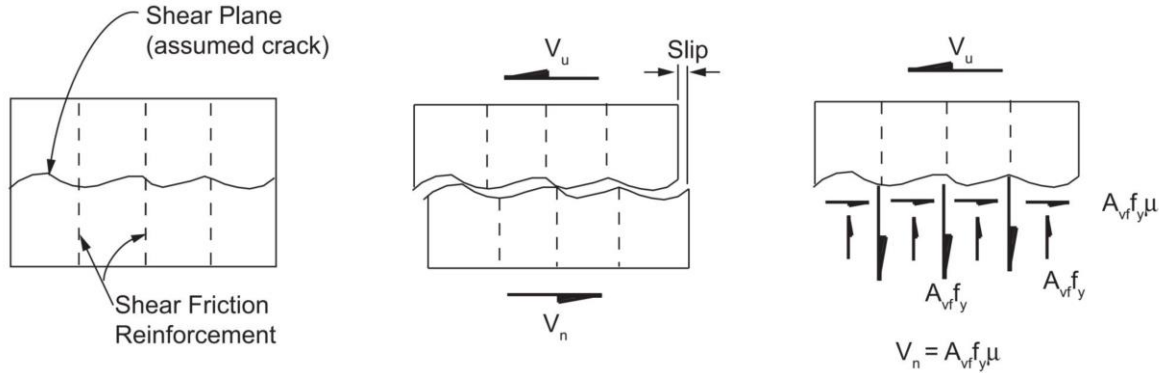


Figure 2.11. Shear-friction concept. ACI 318-08 (2008)

As concluded by Eduardo and Fernando (2008) the use of steel connectors does not significantly increase the interface de-bonding stress, although, after that, the shear stress is highly dependent on the relation between the cross-section area of steel connectors and the area of the interface. According to Santos and Júlio (2010), the load transfer mechanism at the concrete-to-concrete interface based on cohesion, friction and dowel action but the latter one is not explicitly stipulated in any current design codes. As indicated by Thermou (2007), according to previous researchers and codes, the mechanism of sliding resistance accounting for the contribution of shear connectors crossing the interface planes includes:

- Aggregate interlock between contact surfaces, including any initial adhesion of the jacket concrete on the substrate,
- Friction owing to clamping action normal to the interface, and
- Dowel action of any appropriately anchored reinforcement crossing the sliding plane.

$$v_n = v_a + v_c + v_D = v_a + \mu\sigma_N + v_D \text{ or} \quad (2.7)$$

$$\tau_{tot} = \tau_{agr} + \mu(\sigma_c + \rho\sigma_s) + \tau_D$$

$$\sigma_N = p + \rho_s f_s \quad (2.8)$$

In Equation 2.7, the first component represents the shear resistance of the aggregate interlock mechanism including any initial adhesive that decreases at low slip values

while the latter two components are explained as the maximum contribution of frictional and dowel resistance occurring at different slips. Particularly, the second one caused by the normal clamping stress acting on the interface, σ_N , consisting of not only normal external pressure but also clamping action contributed perpendicular to the interface by shear links and calculated as Equation 2.8 according to Thermou and Pantazopoulou (2009). The last contribution brought by dowel action at the interconnection due to the effectiveness of crossing surface shear reinforcement. It is worth to explain again here that the occurrence of slippage as well as the increase of interface crack width causes the tensile behavior, σ_s , of the steel connectors crossing the interface thus the concrete substrates is compressed and the shear forces, shown in tangential shear stress form, τ , are transmitted by friction mechanism. Dowel action is considered by three alternative mechanisms, namely, by direct shear and by kinking and flexure of the steel bars crossing the contact plane according to Thermou (2015).

As required by ACI 318-08 (2008), the contribution of the shear-reinforcement at the interface is calculated as Equation 2.9 or 2.10 considering the inclination angle of shear connectors, perpendicularly or obliquely to the shear plane (Figure 2.12). It can be physically seen that the shear strength of the interface surface can be upgraded if the inclination of shear links α less than 90° . The optimal value of α is the product of the optimum of the terms " $\mu \sin \alpha + \cos \alpha$ " in Equation 2.10. As result, the value can be taken from the product of " $\tan \alpha = \mu$ ". It can be concluded that the optimal angle of inclination of shear connectors is dependent on the value of friction coefficient of the interface surfaces. In case of moments acting on a shear plane, the flexural tension stresses and flexural compression stresses are in equilibrium. There is no change in the resultant compression $A_v f_y$ acting across the shear plane and the shear-transfer strength is not changed.

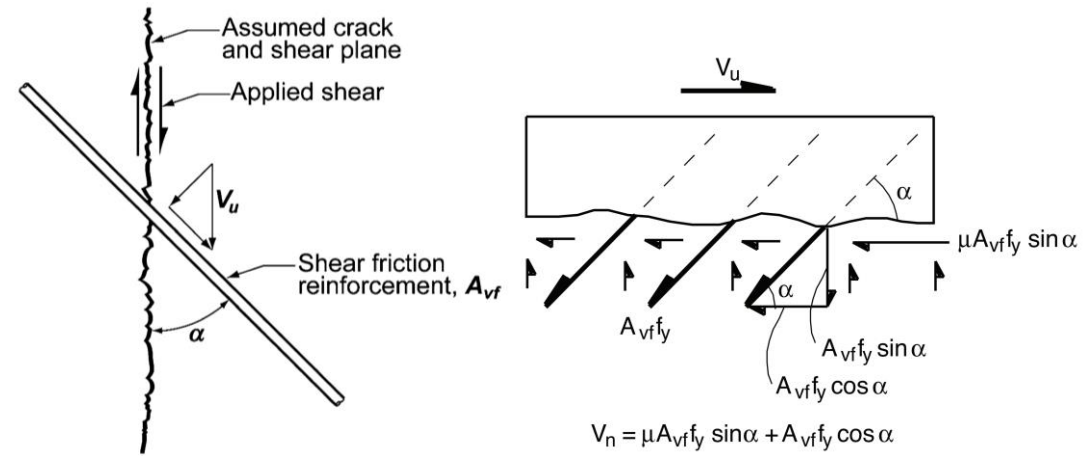


Figure 2.12. Inclined shear- friction reinforcement. ACI 318-08 (2008)

$$v_n = A_{vf} f_y \mu \quad (2.9)$$

$$v_n = A_{vf} f_y (\mu \sin \alpha + \cos \alpha) \quad (2.10)$$

2.1.2.3. Application of geometrical irregularities at the interface

Patton (1966) evaluates the interconnection between plaster layers by applying geometrical irregularities. In the method, plaster surfaces are shaped geometrically such as “saw teeth”, rectangular shaped and triangle shaped asperities etc. (Figure 2.13).

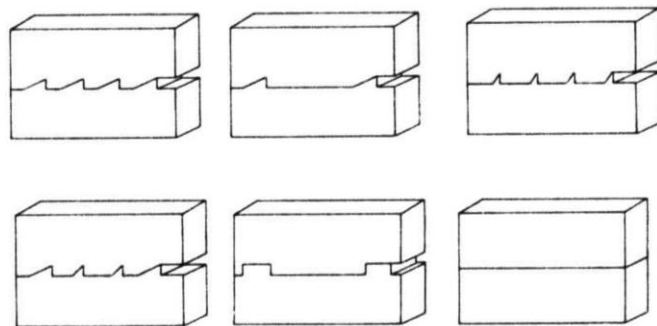


Figure 2.13. Different types of irregularities along interface surfaces. Patton (1966)

In fact, the method obeys Coulombs friction model but the whole interface surface now comprises a lot of small interface surfaces that can be perpendicular, parallel or oblique to the general surface. It means that the basic shear transferring mechanism does not change but is applied to each smaller surface. As results of research of Patton (1966) on

plaster specimens, it can be concluded that in comparison with flat surfaces the appearance of geometrical irregularities at the interface plays an important role in upgrading the shearing strength.

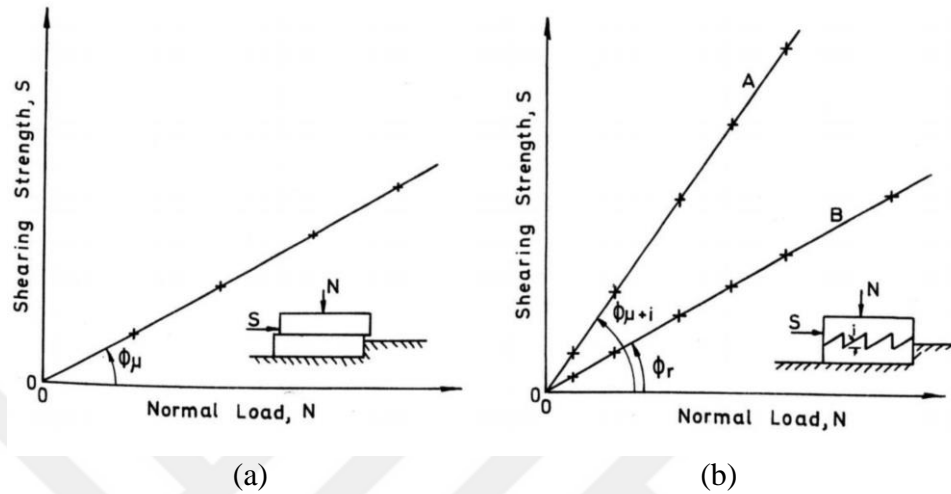


Figure 2.14. Shearing resistance. (a) Flat (b) Teeth shaped surface. Patton (1966)

Figure 2.14 illustrates the enhancement of shearing strength applying triangle “teeth” shaped irregularities on the interface surfaces compared to a reference specimen left with flat interface surfaces.

A value shearing strength determined under a constant normal stress and then graphically enveloped when a range of normal stress is applied. Firstly, the initial slope ϕ_μ of each line graph standing for the friction coefficient in case of flat interface surfaces ($\tan\phi_\mu$) is upgraded to a higher value $\phi_{\mu+i}$ when “saw teeth” shaped irregularities with an inclination of i . Secondly, in case of “saw teeth” shaped surfaces, with a given normal stress, the failure sliding failure stress is determined based on the slope $\phi_{\mu+i}$ until the collapse of “saw teeth” shaped asperities. Afterward, the shearing capacity performs a lower value. The relationship between the shearing strength and normal stress is linearly depicted according to a reduced slope, ϕ_r . The reduced slope ϕ_r is known as the angle of residual shearing resistance of materials that initially were partly and completely intact.

It can be stated that the deviation between two linear lines is the contribution of asperities to the shear capacity of the whole shaped surface. Additionally, the value of ϕ_r and ϕ_μ are approximately identical to each other with a slight deviation of less than $1,5^\circ$. According to Patton (1966) it can be observed that the line A represents not only the value of the external frictional resistance along the inclined planes but also the internal strength of the teeth at the point of failure due to the fact that these two strengths are equal as the failure occurs.

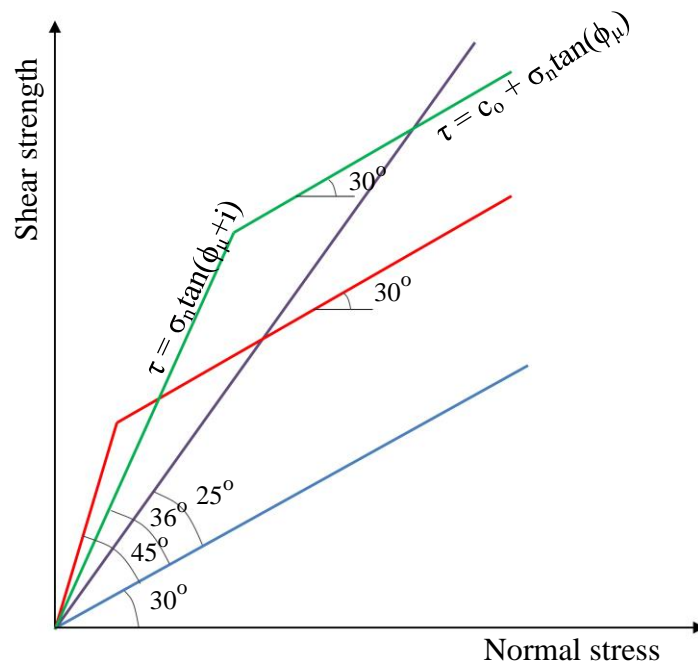


Figure 2.15. Failure envelopes for specimens with different inclinations of teeth. Patton (1966)

When the influence of the intensity of normal stress is considered, Figure 2.15 shows that the failure strength line of a specific value of angle i is divided into a lower (primary portion) and an upper (second portion). Initially, the first regime inclines with an angle of $\phi_\mu + i$ and then is followed by the second part whose inclination is reduced to ϕ_r . It means that the second portion is parallel to the line inclining with the residual slope. Secondly, it can be observed that the application of irregularities with a higher value of inclination causes a sooner transmission. As results, the contribution of “teeth” with higher inclination is higher in case of lower pressure. Conversely, in range of high

normal stress, asperities inclining with smaller angle perform higher value of shear strength due to the earlier occurrence of transmission. Finally, it is interestingly imagining that a cohesion intercept will occur as the value $\phi_{\mu+i}$ is equal to or greater than 90° . Follow that, there is no occurrence of sliding until asperities are collapsed and the shear strength versus normal stress line inclines parallel to the residual line.

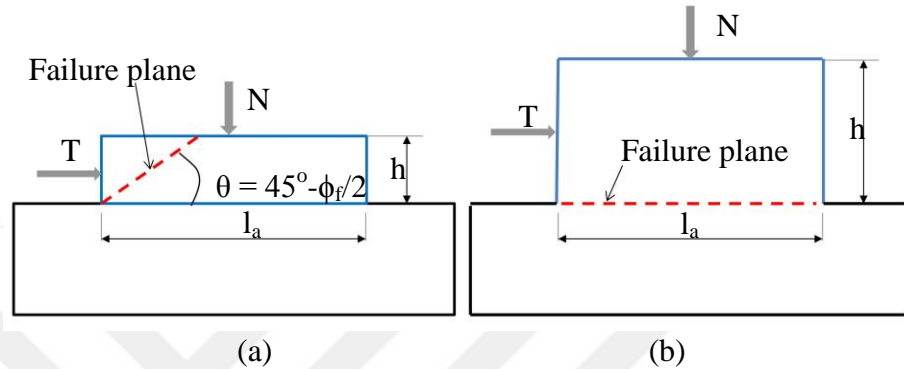


Figure 2.16. Shear mechanisms of rectangular shaped irregularity. (a) dilative failure (b) non-dilative failure. Kwon et al. (2009)

Focus on rectangular shaped asperities on inter-rock surfaces, Kwon et al. (2009) indicate two shear mechanisms a dilative failure mode with an inclination of $(45-\phi_f/2)^\circ$ where ϕ_f is the peak friction angle and a non-dilative failure mode with shearing of asperity (Figure 2.16). Due to experimental evaluation Kwon et al. (2009) conclude that the shear mechanism of small-scale asperities is relevant to not only sliding but also breakage of the asperities. That conclusion seemly matches the previous statement of Patton (1966). The authors also claim that contrary to triangular asperities, rectangular asperities always break with the dilative or non-dilative failure mode. Therefore, rectangular asperities may more closely reflect the characteristics of a rough joint surface and get insight into joint shear behaviors even in a small deformation regime.

According to Kwon et al. (2009), the dilative failure occurs when the aspect ratio α defined as the ratio of asperity height h to asperity length l_a is smaller than the critical aspect ratio obtained by Equation 2.11. It is noted that the value of aspect ratio ranges from 0,15 to 0,32. The peak shear strength of the interface surface shaped with

irregularities is determined as Equation 2.12 dependently on the value of the aspect ratio.

$$\alpha_{critical} = \frac{c + \sigma_n \tan \phi_f}{2c \tan \left(45^\circ + \frac{\phi_f}{2} \right) + \sigma_n \tan^2 \left(45^\circ + \frac{\phi_f}{2} \right)} \quad (2.11)$$

$$\tau_f = \begin{cases} 2\alpha.c \tan \left(45^\circ + \frac{j_f}{2} \right) + \alpha.\sigma_n \tan^2 \left(45^\circ + \frac{j_f}{2} \right), & \text{if } \alpha < \alpha_{critical} \\ c + \sigma_n \tan j_f, & \text{, otherwise} \end{cases} \quad (2.12)$$

When stipulating about shear strength at the interface between concrete cast at different times, the contribution of cohesion in order to account for the interlocking mechanism between aggregates as Equation 2.13 according to EN 1992-1-1 (2004). Besides that, a surface treatment method namely indented construction joints introduced by applying geometrical irregularities. With a surface shaped using indented joint (Figure 2.17), the friction and cohesion coefficient of the interface is increase from 0,6 (smooth) to 0,9 and from 0,20 to 0,50, respectively. Similar to ACI 318-08 (2008), the inclination of steel reinforcement, α is limited from 45° to 90° .

$$V_{Rdi} = c f_{ctd} + \mu \sigma_n + \rho f_{yd} (\mu \sin \alpha + \cos \alpha) \leq 0.5 v f_{cd} \quad (2.13)$$

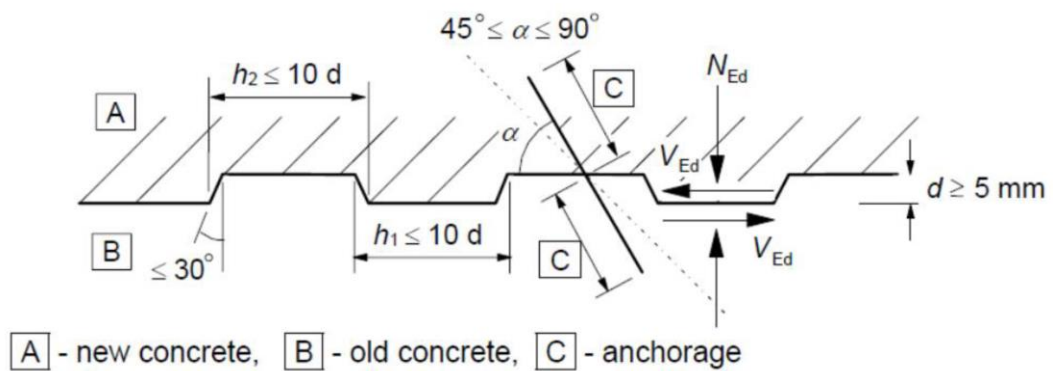


Figure 2.17. Indented construction joint. EN 1992-1-1 (2004)

For simplification purpose, the shear strength of a surface that is satisfied specific conditions can be calculated as aforementioned equations applying simple parameters.

According to EN 1992-1-1 (2004) a rough surface with at least 3 mm roughness at about 40 mm spacing, achieved by raking, exposing of aggregate or other methods giving an equivalent behavior: $c = 0,40$ and $\mu = 0,70$ while ACI 318-08 (2008) the coefficient μ is assumed to equal to 1,0 in case of normal weight concrete, interface shall be roughened to a full amplitude of approximately 1/4 in (appropriate 6,35mm).

2.1.3. Modal analysis

2.1.3.1. General

Modal analysis is applied to figure out the dynamic characteristics of structures widely known as natural frequencies, damping, and mode shapes according to Peter (2001). Modal analysis is alternatively carried out using both mathematical methods and vibration test. The latter is considered as an effective method to identify dynamic characteristics and to recognize the unwanted vibrations that are unavoidable and affect structures under dynamic conditions. Vibration test can help engineers to control unwanted vibrations that are shown clearly under the motion of structures throughout vibrating and to find appropriate solutions to reduce the response of structures effectively. Shaker test is also known as one of the most common vibration methods in order to measure the frequency response of structures based on the driving acceleration levels collected from accelerometers that are attached to the considered structures.

Modal analysis can be discussed basically considered a graphical approach (Figure 21). The response of a considered system or output data is the result of applying arbitrary input load with certain frequency and amplitude. Generally, there are three kinds of response:

- An attenuation,
- A free oscillation or vibration, and
- A vibration with amplitude increasing to infinity.

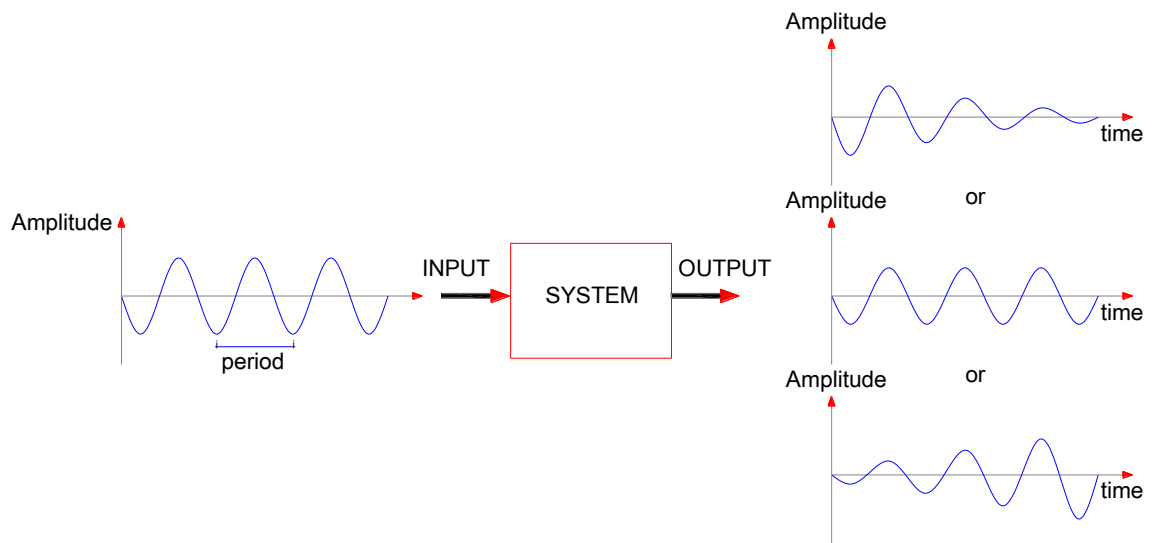


Figure 2.18. An approach to modal analysis.

Based on the output information, the hazardous responses or unwanted vibrations of the system, for instance, the third kind of response in Figure 2.18 is able to be predicted. The response of the system is dependent on dynamic characteristics of the structure, considered as constant properties, and input data consisting of the frequency and amplitude of loading.

The important role of the input frequency can be discussed clearly by approaching a nonmathematical presentation about modal analysis explained by Peter (2001). A sinusoidal force is applied to a single plate without any boundary condition (Figure 2.19). It is noted that the external force vibrates at a corner of the plate while at another corner, whose output response, particularly displacement, velocity or acceleration, is recorded using an accelerometer throughout the excitation. The backbone of this simple vibration test is that the frequency of the sinusoidal force varies increasingly while the amplitude keeps constant in order to evaluate the influence of the input frequency on the response of the plate.

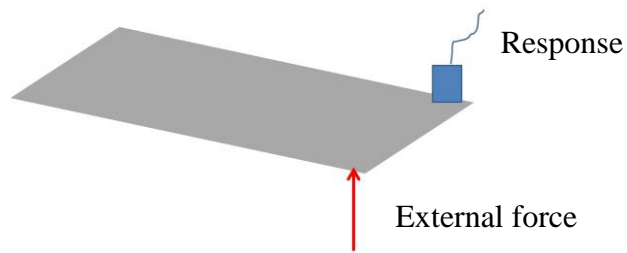


Figure 2.19. Overview of oscillation. Peter (2001)

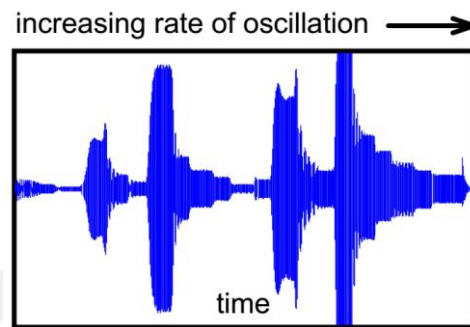


Figure 2.20. Overview of oscillation. Peter (2001)

The response amplitude at the corner is depicted in Figure 2.20. It is interesting noting that the amplitude of external vibrating force is kept constant whereas the amplitude of vibration at the considered corner changes remarkably throughout the time. That proves that the rate of oscillation or the frequency of external load decides the response of system. When increasing the rate of external vibration the amplitude of corner can increase or decrease. From Figure 2.20, the most noticed interest is the four amplitudes performing highly than others. It is interestingly noted that the rate of response tends to be equal to the rate of external excitation at the time ranges that the amplitude of response reaches distinguish levels. The event in which the frequency of the external oscillation and the response is equal to each other is called resonance. The frequencies of response, determined by Fast Fourier Transform (FFT) method based on the time data, are known as the natural frequencies or resonant frequencies of the specimen.

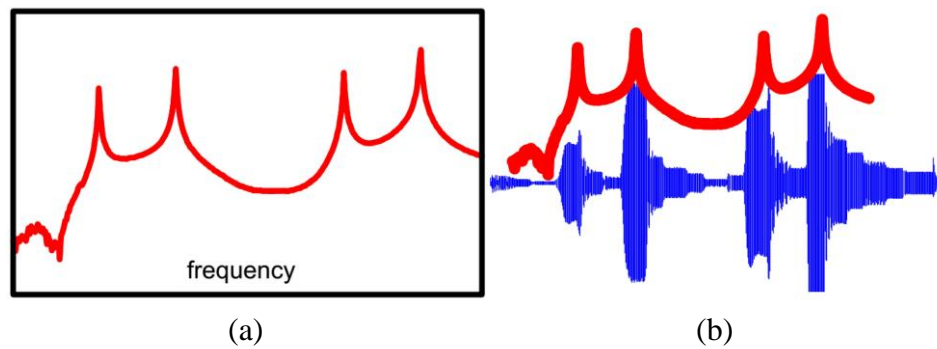


Figure 2.21. Overlay the frequency trace with time trace. Peter (2001)

Frequency response functions (FRFs) (Figure 2.21.a) illustrate the values of response frequency displayed on the horizontal axis while the vertical axis shows the corresponding amplitude of the response. The values of the frequency corresponding to the response amplitudes can be extracted from the overlay of frequency trace on time trace (Figure 2.21.b). Now, imagine that the response of a lot of points on the plate is collected during the same process of external vibration. The shape of the system possibly captured at every moment (Figure 2.22).

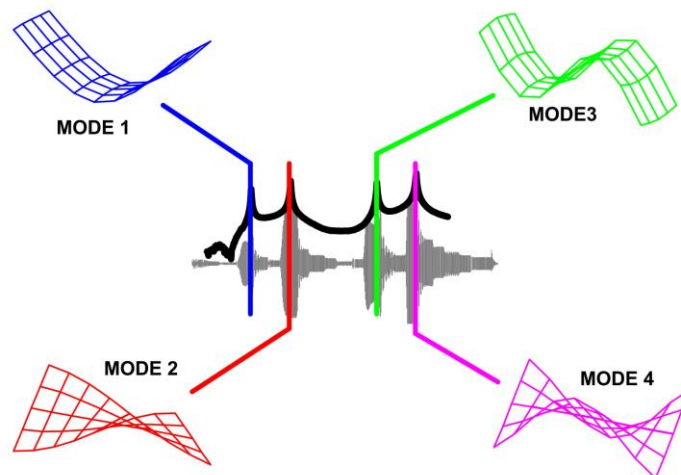


Figure 2.22. FRFs and relative shapes. Peter (2001)

Figure 2.22 displays four mode shapes of the plate at four corresponding moments resonance happens. At resonance, all of the nodes on plate oscillate with a same natural frequency and every node reaches its maximum amplitude at the same moment that builds up mode shapes of the system, mode 1, 2 3 and 4 corresponding to the first,

second, third and fourth resonant frequency. It is observed that at each moment of resonance the response frequency and the frequency of the external excitation is identical to each other, it is called as the resonant frequency. As resonant frequencies, the shape consisting of the maximum amplitude of all nodes at resonance is considered as a dynamic characteristic of the system, widely called as mode shape.

In conclusion, the process of figuring out the dynamic characteristics of a structure is called modal analysis. Modal analysis helps to recognize natural frequencies of a structure as well as its mode shapes. The dynamic characteristics can be used effectively for design purposes according to Peter (2001). In the next parts, the theoretical approach of modal analysis is explained.

2.1.3.2. Theoretical approach

Based on the basic knowledge about vibration of single degree of freedom systems the motion of multi degree of freedom structures is explained here. In comparison with simple structures, multi degree of freedom system is more complicated than in terms of stiffness, damping and mass components (Figure 2.23). These components are now considered in matrix m , c and k respectively and build the motion of structures up by the same way done before as seen in Equation 2.14 in case of elastic behavior and Equation 2.15 for nonlinear behavior.

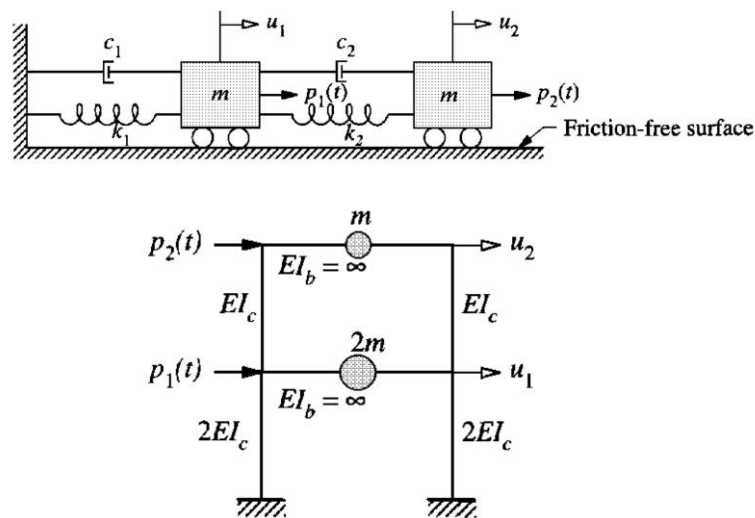


Figure 2.23. Example of multi degree of freedom systems. Chopra (2012)

$$\mathbf{m}\ddot{\mathbf{u}} + \mathbf{c}\dot{\mathbf{u}} + \mathbf{k}\mathbf{u} = \mathbf{p}(t) \quad (2.14)$$

$$\mathbf{m}\ddot{\mathbf{u}} + \mathbf{c}\dot{\mathbf{u}} + \mathbf{f}_s(\mathbf{u}, \dot{\mathbf{u}}) = \mathbf{p}(t) \quad (2.15)$$

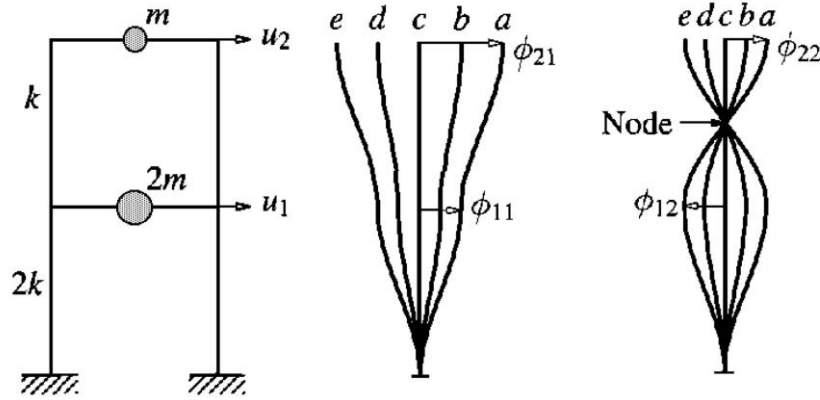


Figure 2.24. Mode shapes of a MDOF structure. Chopra (2012)

Imagine a simple system called free vibration of an undamped two degree of freedom structure. As shown in Figure 27, there are two distinct mode shapes of structures related to two moments of resonance happens. It is noted that in Figure 2.24, $\Phi_n = (\Phi_{1n} \ \Phi_{2n})^T$ (with $n = 1, 2$) is called natural modes of the structure. The motion of masses is defined as Equation 2.16. In other words, there are two natural frequencies and at each resonant event, two masses of structure oscillate around the original positions with the same period T_n ($n=1, 2$) or frequency ω_n determined based on Equation 2.16. Thus natural frequencies of MDOF structures can be found easily.

$$\det[\mathbf{k} - \omega_n^2 \mathbf{m}] = 0 \quad (2.16)$$

2.1.3.3. Experimental method – vibration tests

Frequency response functions (FRFs) is very simply the ratio of the output response of a structure due to an applied force according to Peter (2001). The response of structure or output data and input data, external vibration in other words, is collected simultaneously. Displacement, velocity or acceleration in time domain is digitalized into

frequency domain using FFT method available in any signal analyzer. In frequency response functions, magnitude, phase lag, real and imaginary parts are considered as the result of modal analysis.

Let's take a 3 DOF beam as a simple example of FRFs (Figure 2.25). In the experimental test, external vibration is located at point 3 while three accelerometers are mounted at node 1, 2 and 3. The collected data amplitude varying to time (displacement, velocity or acceleration) at each point is drawn as the right pictures. In frequency response functions, these original data then are changed in to magnitude, phase lag, real and imaginary parts by using Fast Fourier Transfer Method in order to figure out natural frequencies and mode shapes of the system, as shown in Figure 2.26.a and Figure 2.26.d respectively.

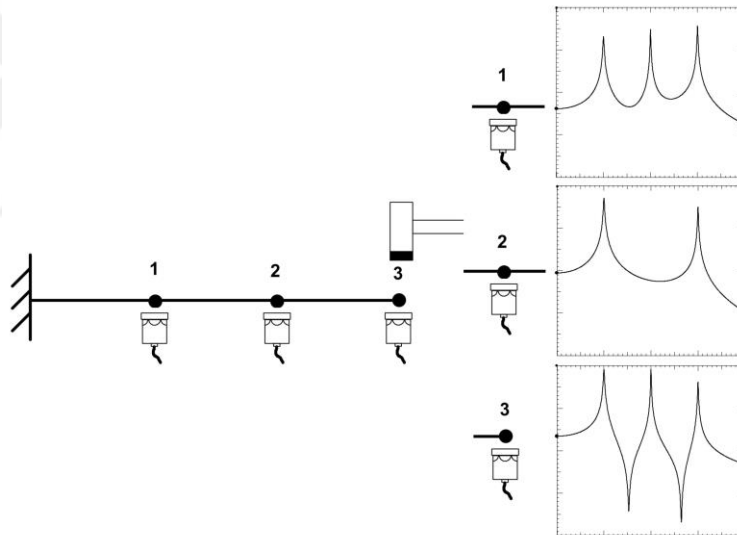


Figure 2.25. Test setup. Peter (2001)

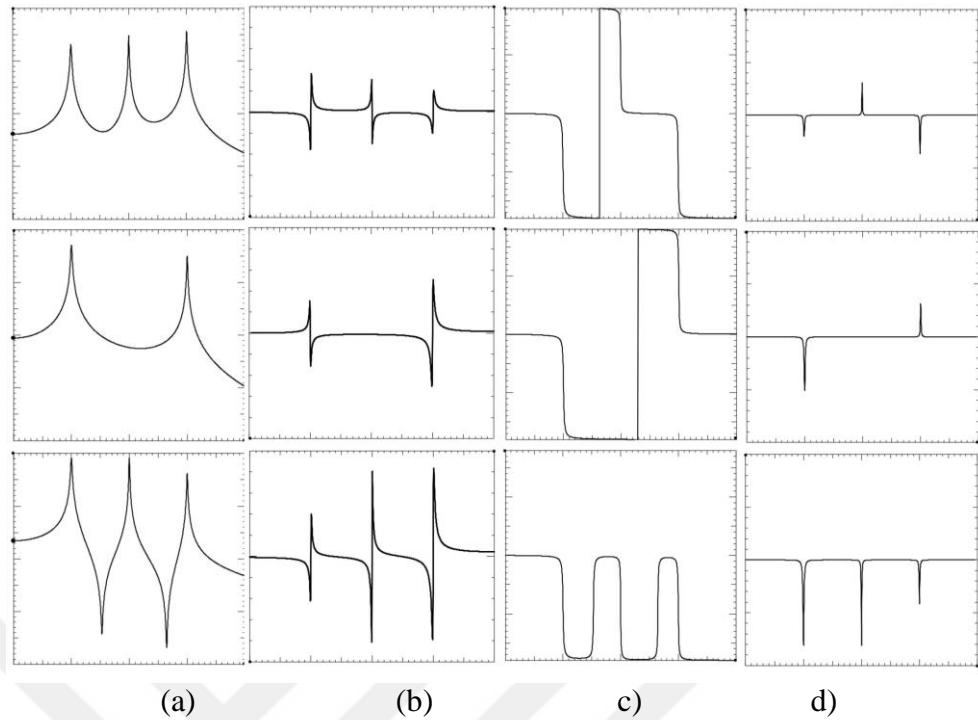


Figure 2.26. Frequency response function. (a) Magnitude (b) Phase lag (c) Real (d) Imaginary part. Peter (2001)

Waterfall plot can be obtained by increasing the number of accelerators along the beam and adding imaginary parts like Figure 2.26.d into a same graph. Mode shapes of the beam can be seen clearly in such a plot as in Figure 2.27. This experimental test for modal analysis is widely called as shaker test. There is another one method called impact test measures data at one point by moving external vibration source. In shaker test, data is collected from every considered point simultaneously when the structure is vibrated by external force mounted at only one fixed position. However, the impact test results in the same result as shaker test according to theoretical standpoint explained before.

In conclusion, dynamic characteristics of structures are able to be acquired using FFT method analyzer or a data acquisition system with software performing FFT method.

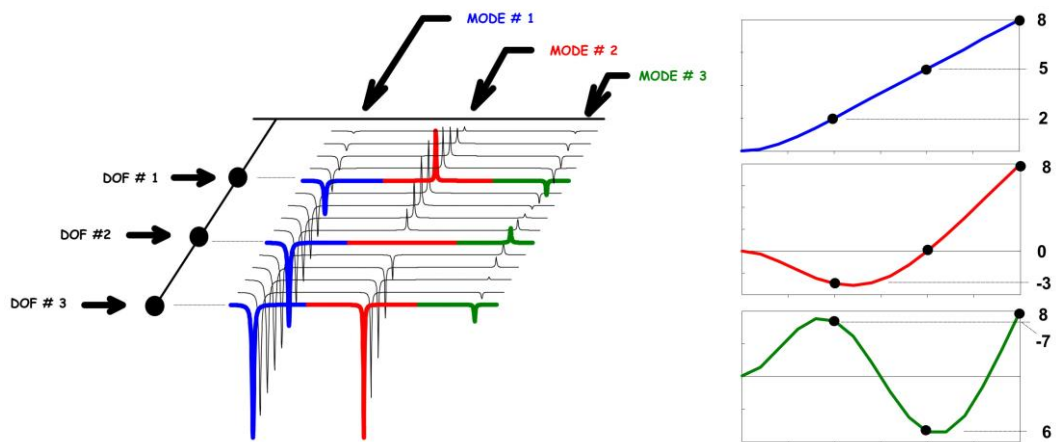


Figure 2.27. Waterfall plot of beam frequency response functions. Peter (2001)

2.1.4. Concrete damage plasticity model

2.1.4.1. Detailed input material model

In Abaqus, tension stiffening is used to define strain-softening behavior of cracked concrete and compression hardening behavior outside of elastic state (Figure 2.28). The parameters in Figure 2.28 can be calculated as from Equation 2.17 to Equation 2.20.

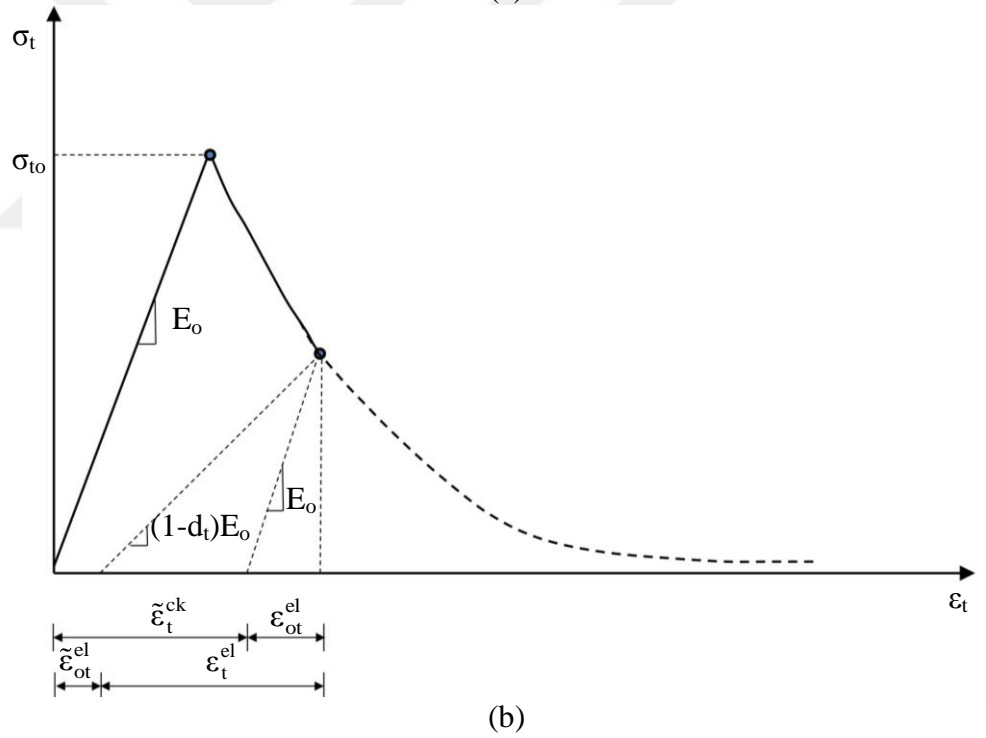
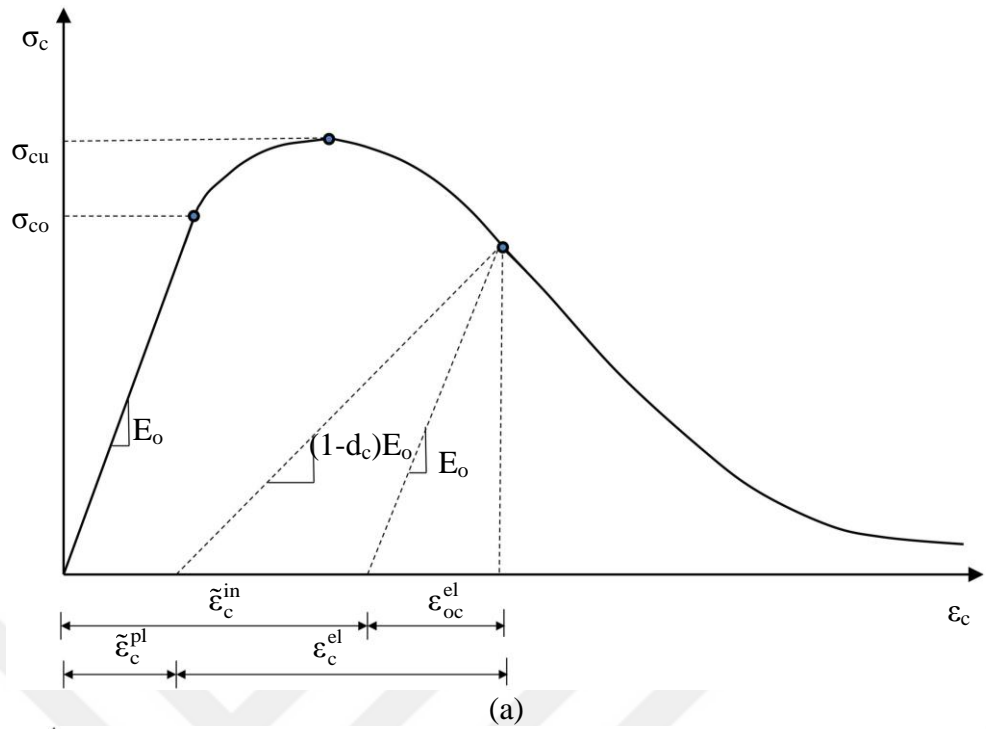


Figure 2.28. Elastic degradation in tension (a) and compression (b) Dassault Systèmes (2013)

$$\varepsilon_{oc}^{el} = \frac{\sigma_c}{E_o} \tag{2.17}$$

$$\tilde{\varepsilon}_c^{pl} = \tilde{\varepsilon}_c^{in} - \frac{d_c}{(1-d_c)} \frac{\sigma_c}{E_o} \quad (2.18)$$

$$\varepsilon_{ot}^{el} = \frac{\sigma_t}{E_o} \quad (2.19)$$

$$\tilde{\varepsilon}_t^{pl} = \tilde{\varepsilon}_t^{ck} - \frac{d_t}{(1-d_t)} \frac{\sigma_t}{E_o} \quad (2.20)$$

2.1.4.2. Selected concrete model

In the present thesis, the uniaxial behavior of concrete is built based on Hsu and Hsu (1994) whereas the tensile regime is defined following Aslani and Jowkarmeimandi (2012).

Initially, a complete stress-strain curve under uniaxial compression introduced by Hsu and Hsu (1994) defining common parameters with physical significance is divided into two branches. The first one implies an elastic behavior until normal stress reaches a value of $0,45\sigma_{cu}$, In the second regime, the stress-strain curve initiates at the final point of the first branch and the destination is captured at $(0,3\sigma_{cu};\varepsilon_d)$ (Figure 2.29.a). It is noted that, the relation between stress and strain in the second part is suitable only for concrete whose ultimate compressive stress σ_{cu} is less than 62MPa. The second relation between stress and strain is shown in equation 2.21 and the necessary component is calculated as Equation 2.22 which the unit of the compressive strength of concrete σ_{cu} is kip/in².

$$\sigma_c = \frac{\beta(\varepsilon_c / \varepsilon_o)}{\beta - 1 + (\varepsilon_c / \varepsilon_o)^\beta} \sigma_{cu} \quad (2.21)$$

$$\beta = \left(\frac{\sigma_{cu}}{9,46} \right)^3 + 2,59 \quad (2.22)$$

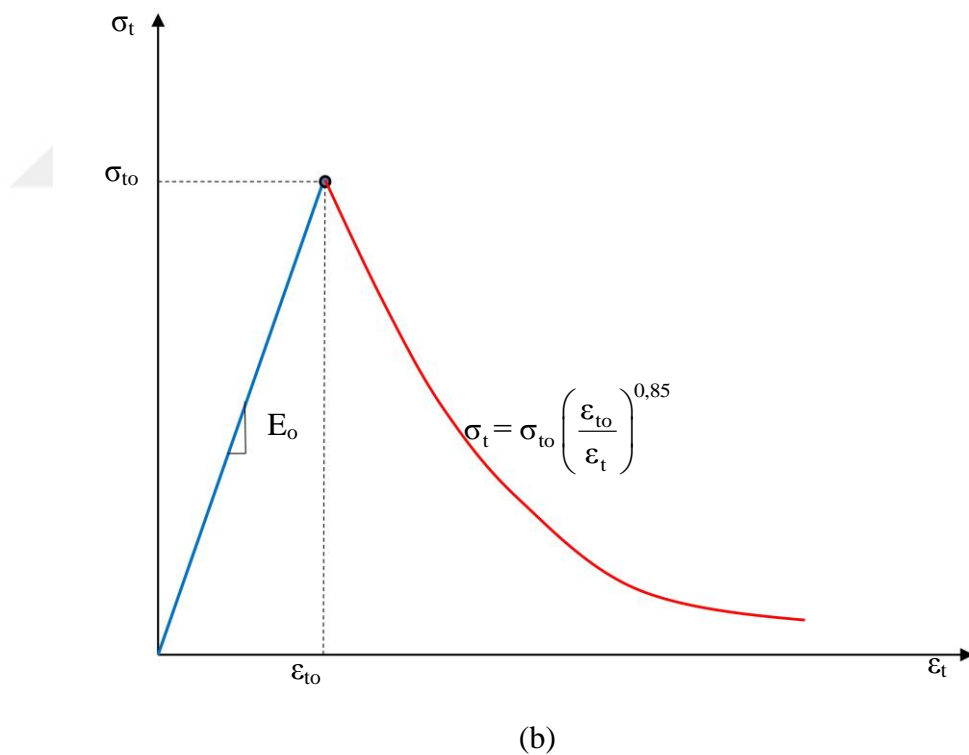
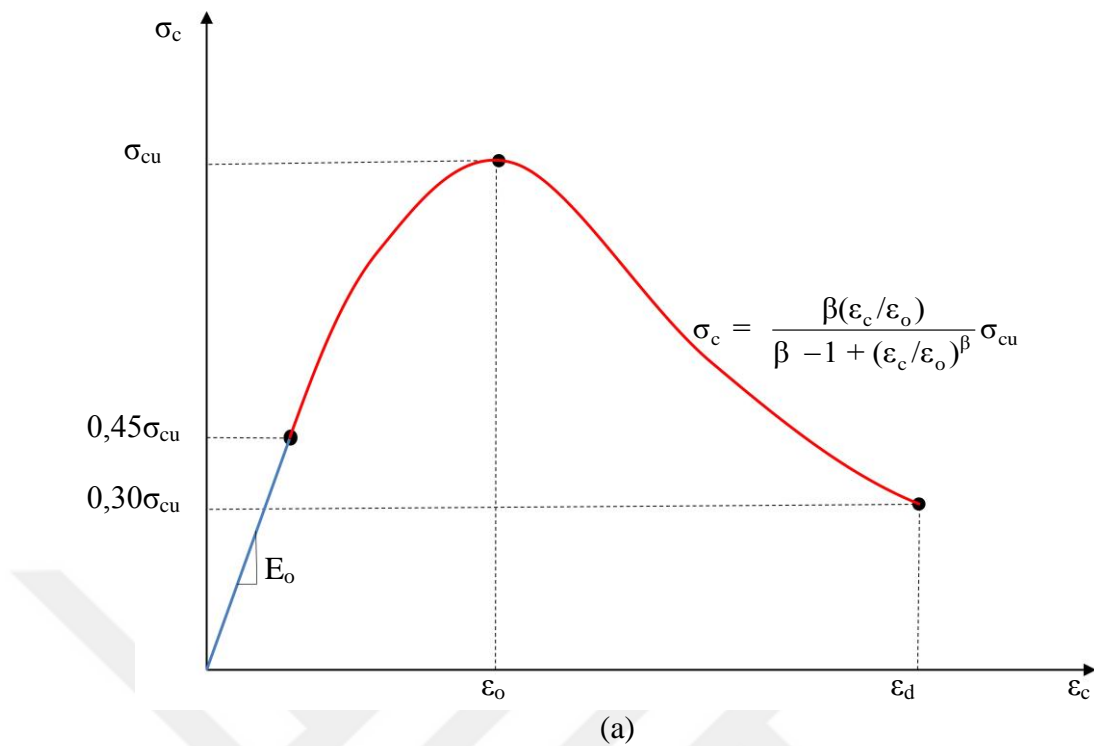


Figure 2.29. Complete stress-strain behavior of concrete. (a) In compression. Hsu and Hsu (1994) (b) In tension. Aslani and Jowkarmeimandi (2012)

In order to quantify the effect of compressive strength on the strain at peak ϵ_o and initial tangential modulus E_{it} , a regression analysis was performed to establish a relationship

between the compressive strain and these parameters whose value can be determined as Equation 2.23 and 2.24 the unit of kip/in² is considered.

$$\varepsilon_o = 8,9 \times 10^{-5} \sigma_{cu} + 2,114 \times 10^{-3} \quad (2.23)$$

$$E_{it} = 1,2431 \times 10^2 \sigma_{cu} + 3,28312 \times 10^3 \quad (2.24)$$

On the other hand, the stress-strain relation in tension is built based on Aslani and Jowkarmeimandi (2012) (Figure 2.29.b). A complete relation consists of two regimes, a linear relation is captured until the failure stress of concrete is achieved and the descending branch is determined following equation 2.25.

$$\sigma_t = \sigma_{to} \left(\frac{\varepsilon_{to}}{\varepsilon_t} \right)^{0,85} \quad (2.25)$$

2.1.5. Nonlinear performance of existing structure

2.1.5.1. General

The seismic response of a structure built in areas prone to intense earthquake events is possibly estimated by a rigorous procedure called nonlinear time history analysis and nonlinear static pushover analysis known as an approximate method. In the latter procedure, invariant lateral force calculated based on the predominant frequency is applied monotonically to the structure until a target displacement is reached. The concept of NSPA is the single degree of freedom idealization. It can be explained that, the structure is assumedly just has one lumped mass localized at the top and the numerous joints and damping are ignored. NSPA results in satisfied seismic demands and is being under-researched in order to get closer to the time-variant procedure because the present method just focuses on the fundamental mode kept unchanged even after yielding. Beside the simplicity and attractiveness of low computational cost, pushover analysis with incremental step of loading, the behavior of structures from the elastic range to ultimate and then the final failure mode can be scrutinized easily.

The simplified nonlinear method consists of the capacity spectrum analysis (CSA), the displacement coefficient method, and the secant method. The first method estimating the maximum displacement of structures based on the performance point, intersection of the capacity curve obtained by pushover analysis and the reduced response spectrum is considered in the present thesis.

According ATC 40 (1996), three primary elements required for CSA are capacity, demand (displacement) and performance. Firstly, the capacity of a whole structure is dependent on the strength and performance each components determined beyond elastic state by pushover procedure. The lateral force is applied monotonically until the structure become unstable or a predetermined is reached. Next, demand (displacement) is the maximum expected response of a considered structure excited by a certain earthquake event. Finally, performance check verifies that the structure is not damaged beyond an acceptable limit for force and displacement implied by displacement demand. The next subsections are to explain step by step from the construction of a demand spectrum, a pushover procedure and the performance check for a certain structure.

2.1.5.2. Performance point - ATC 40 (1996)

The part explains the procedure stipulated by ATC 40 (1996) to apply a nonlinear static analysis procedure namely the capacity spectrum method (CPM) that determines the maximum displacement of structures subjected to a specific seismic condition based on the intersection point, widely known as performance point, of the capacity curve obtained by pushover analysis and a reduced response spectrum. In other words, the performance point is used to evaluate whether the capacity of structures displayed as pushover curve is able to handle the demand. The capacity spectrum method requires three necessary elements: capacity, demand (displacement), and performance.

According to ATC 40 (1996) The location of the performance point must satisfy two relationship: 1) the point must lie on the capacity spectrum curve in order to represent the structure at a given displacement, and 2) the point must lie on a spectral demand curve reduced from the elastic 5% damped design spectrum that represents the nonlinear demand at the same structural displacement. Reducing the first seismic demand from

5% damped elastic demand spectrum is to account for the effect of energy dissipation. It is worth noting here that 5% damped demand spectrum is considered as the initial one because 5% viscous damping inherent in structures assumed to be constant according to ACT 40 (1996). The reduction factors are given in terms of effective damping that calculated approximately based on the shape of the capacity curve, the estimated displacement demand, and the resulting hysteresis loop.

The Acceleration Displacement Response Spectrum (ADRS) merging the top lateral displacement-base shear curve (V_b - Δ), obtained by monotonic lateral force and the response spectrum curve is a concept of pushover analysis. It means that the demand response spectra and the structural capacity are plotted in a same graph according to the Capacity Spectra technique.

The V_b - Δ coordinate is transferred into displacement spectrum versus pseudo-acceleration spectrum (S_d - S_a) Cartesian using transforming Equations 2.26 and 2.27 according to ATC-40 (1996) (Figure 2.30). Base shear force versus displacement curve is resulted by a monotonically and incrementally lateral pushing whose force determined based on the fundamental modes predominant the response of structures during ground motions, normally the first mode if the corresponding frequency is about up to one second according to ATC 40 (1996).

$$S_{a_i} = \frac{V_i / W}{\alpha_i} \quad (2.26)$$

$$S_{d_i} = \frac{\Delta_{roof}}{(PF_i \cdot \phi_{1,roof})} \quad (2.27)$$

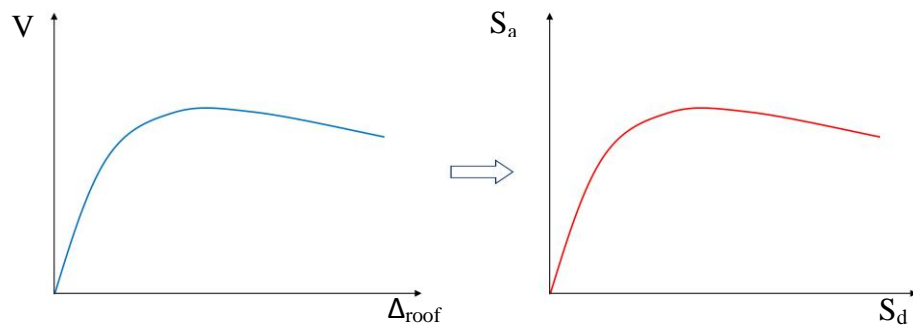


Figure 2.30. Transformation from $V_b-\Delta$ to S_a-S_d .

According to ATC 40 (1996), primary ground shaking criteria includes site geology and soil characteristics, site seismicity characteristics and site response spectra. Firstly, each site is assigned a soil profile type based on properly substantiated geotechnical data (Table 2.1).

Table 2.1. Soil Profile Types. ATC 40 (1996)

Soil Profile Type	Soil Profile Name/ Generic Description	Average Soil Properties for Top 100 Feet of Soil Profile		
		Shear wave Velocity, V_s (feet/second)	Standard Penetration Tets, N for N_{CN} for cohesionless soil layers (blows/foot)	Undrained Shearing strength, S_U (psf)
S_A	Hard Rock	$V_s > 5,000$	Not Applicable	
S_B	Rock	$2,500 < V_s \leq 5,000$	Not Applicable	
S_C	Very Dense Soil and Soft Rock	$1,200 \leq V_s \leq 2,500$	$N > 50$	$S_U > 2,000$
S_D	Stiff Soil Profile	$600 \leq V \leq 1200$	$15 \leq N \leq 50$	$1,000 \leq S_U \leq 2,000$
S_E	Soft Soil Profile	$V_s < 600$	$N < 15$	$S_U < 1,000$
S_F	Soil Requiring Site-Specific Evaluation			

Secondly, seismicity characteristics for a site are based on the seismic zone, the proximity of the site to active seismic sources, and site soil profile characteristics. Each structure is assigned a seismic zone factor Z (Table 2.2). The distance between a

considered site and the place where earthquake initiates is accounted for through near-source factor (Table 2.3) considering seismic source type (Table 2.4). Following that, seismic coefficients are determined (Table 2.5 and Table 2.6).

Table 2.2. Seismic Zone Factor (Z). ATC 40 (1996)

Zone	1	2A	2B	3	4
Z	0,075	0,15	0,20	0,30	0,40

Table 2.3. Near Source Factor (N_A) and (N_V), ATC 40 (1996)

Seismic Source Type	Closest Distance to Known Seismic Source							
	<2km		5km		10km		>15km	
	N_A	N_V	N_A	N_V	N_A	N_V	N_A	N_V
A	1,5	2,0	1,2	1,6	1,0	1,2	1,0	1,0
B	1,3	1,6	1,0	1,2	1,0	1,0	1,0	1,0
C	1,0	1,0	1,0	1,0	1,0	1,0	1,0	1,0

Table 2.4. Seismic Source Type. ATC 40 (1996)

Seismic Source Type	Seismic Source Description	Seismic Source Definition	
		Maximum Moment Magnitude, M	Slip Rate, SR (mm/year)
A	Faults that are capable of producing large magnitude events and which have a high rate of seismic activity	$M \geq 7$	$SR \geq 5$
B	All faults other than types A and C	Not Applicable	Not Applicable
C	Faults that are not capable of producing large magnitude earthquakes and that have a relatively low rate of seismic activity	$M < 6,5$	$SR < 2$

Table 2.5. Seismic Coefficient (C_A), ATC 40 (1996)

Soil Profile Type	Shaking Intensity, ZEN					
	=0,075	=0,15	=0,20	=0,30	=0,40	>0,40
S_B	0,08	0,15	0,20	0,30	0,40	1,0(ZEN)
S_C	0,09	0,18	0,24	0,33	0,40	1,0(ZEN)
S_D	0,12	0,22	0,28	0,36	0,44	1,1(ZEN)
S_E	0,19	0,30	0,34	0,36	0,36	0,9(ZEN)
S_F	Site-specific geotechnical investigation required to determine C_A					

Table 2.6. Seismic Coefficient (C_V). ATC 40 (1996)

Soil Profile Type	Shaking Intensity, ZEN					
	=0,075	=0,15	=0,20	=0,30	=0,40	>0,40
S_B	0,08	0,15	0,20	0,30	0,40	1,0(ZEN)
S_C	0,13	0,25	0,32	0,45	0,56	1,4(ZEN)
S_D	0,18	0,32	0,40	0,54	0,64	1,6(ZEN)
S_E	0,26	0,50	0,64	0,84	0,96	2,4(ZEN)
S_F	Site-specific geotechnical investigation required to determine C_V					

It is noted that in Table 2.5 and Table 2.6, the value of E used to determine the product, $Z \cdot E \cdot N$, should be taken to be equal to 0,5 for the Serviceability Earthquake, 1,0 for the Design Earthquake and 1,25 (Zone 4 sites) or 1,5 (Zone 3 sites) for the Maximum Earthquake.

Based on aforementioned parameters, the elastic response spectra for a site now are able to be constructed (Figure 2.31). The transformation from S_a-T to S_a-S_d is done rapidly using Equation 2.28.

$$S_{di} = \frac{T_i^2}{(4\pi^2)} S_{ai} g \quad (2.28)$$

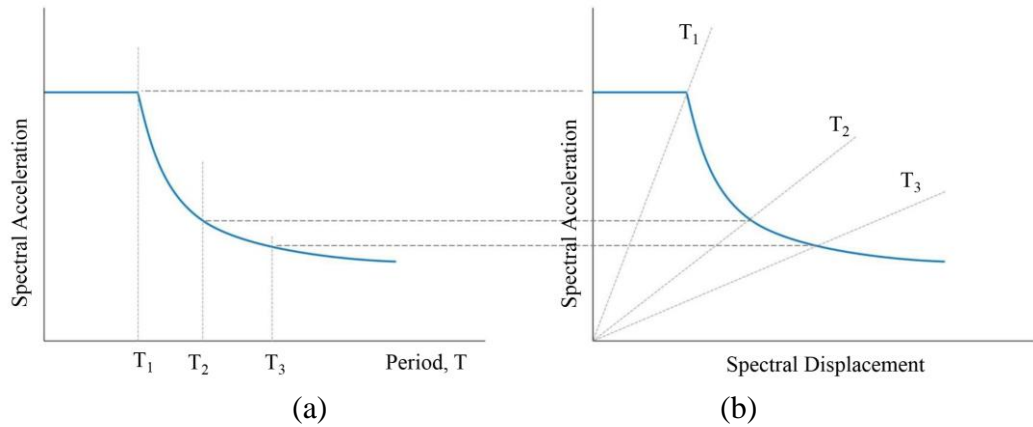


Figure 2.31. Demand spectrum. (a) S_a - T (b) S_a - S_d . ATC 40 (1996)

ATC40 (1996) builds the 5% response spectrum and then the reduced 5% response spectrum is depicted (Figure 2.32).

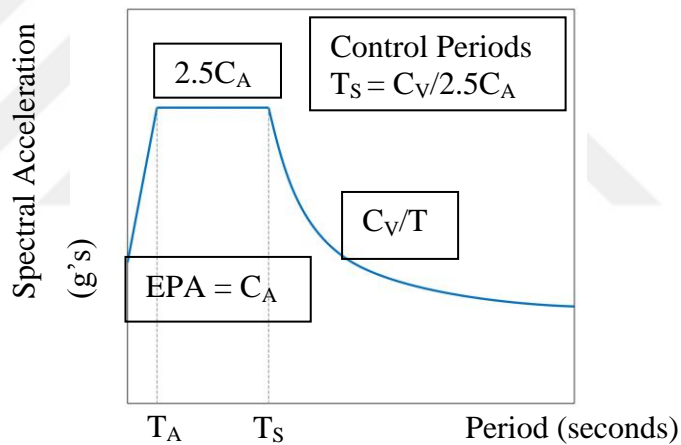


Figure 2.32. Construction of a 5 %-damped elastic response spectrum. ATC 40 (1996)

Additionally, spectral reduction factors are used to decrease the elastic (5% damped) response spectrum to a reduced response spectrum with damping greater than 5% of critical damping (Figure 2.33).

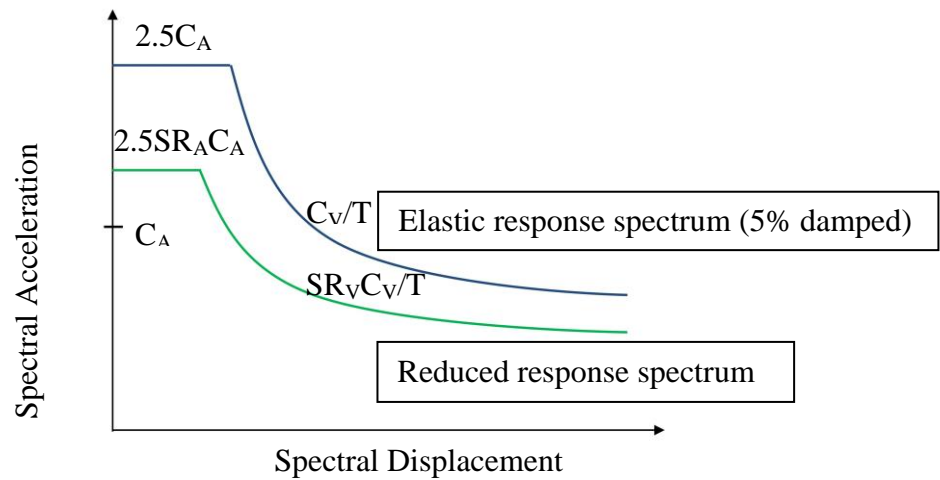


Figure 2.33. Original 5% damped and reduced response spectrum. ATC 40 (1996)

The parameters SR_A and SR_V are calculated as Equation 2.29 and 2.30 according to ATC 40 (1996) and should be greater than the values shown in Table 2.7.

$$SR_A = \frac{3,21 - 0,68 \ln(\beta_{eff})}{2,12} \quad (2.29)$$

$$SR_V = \frac{2,31 - 0,41 \ln(\beta_{eff})}{1,65} \quad (2.30)$$

Table 2.7. Minimum allowable SR_A and SR_V values, ATC 40 (1996)

Structural Behavior Type	SR_A	SR_V
Type A	0,33	0,50
Type B	0,44	0,56
Type C	0,56	0,67

The parameter β_{ff} called effective viscous damping is determined by Equation 2.31 while κ is known as a damping modification factor (Table 2.8) is determined based on duration of shaking and the quality of structures (Table 2.9).

$$\beta_{eff} = \frac{63,7\kappa(a_y d_{pi} - d_y a_{pi})}{a_{pi} d_{pi}} + 5 \quad (2.31)$$

$$\beta_o = \frac{63,7(a_y d_{pi} - d_y a_{pi})}{a_{pi} d_{pi}} \quad (2.32)$$

Table 2.8. Values for damping modification factor κ , ATC 40 (1996)

Structural Behavior Type	β_o (percent)	κ
Type A	$\leq 16,25$	1,0
	$>16,25$	$1,13 \frac{0,51(a_y d_{pi} - d_y a_{pi})}{a_{pi} d_{pi}}$
Type B	≤ 25	0,67
	>25	$0,845 \frac{0,446(a_y d_{pi} - d_y a_{pi})}{a_{pi} d_{pi}}$
Type C	Any value	0.33

Table 2.9. Values for damping modification factor κ , ATC 40 (1996)

Shaking Duration	Essentially New Building	Average Existing Building	Poor Existing Building
Short	Type A	Type B	Type C
Long	Type B	Type C	Type C

The performance point is defined as the intersection point of the capacity spectrum and the spectral demand curve that is reduced from the elastic demand spectra. Spectral reduction factor is determined based on effective damping factor of the structure. A bilinear representation of the capacity spectrum (Figure 2.34) is needed to estimate the effective damping and appropriate reduction of spectral demand. Construction of the bilinear representation requires definition of a_{pi} and d_{pi} , the trial performance point which is estimated by the engineer to develop a reduced demand response spectrum. If

the reduced response spectrum is found to intersect the capacity spectrum at the estimated a_{pi} and d_{pi} , then that point is the performance point (Figure 2.34). The trial performance point must satisfy the condition $0,95d_{pi} \leq d_p \leq 1,05d_{pi}$ with d_p is the displacement interaction point (Figure 2.35).

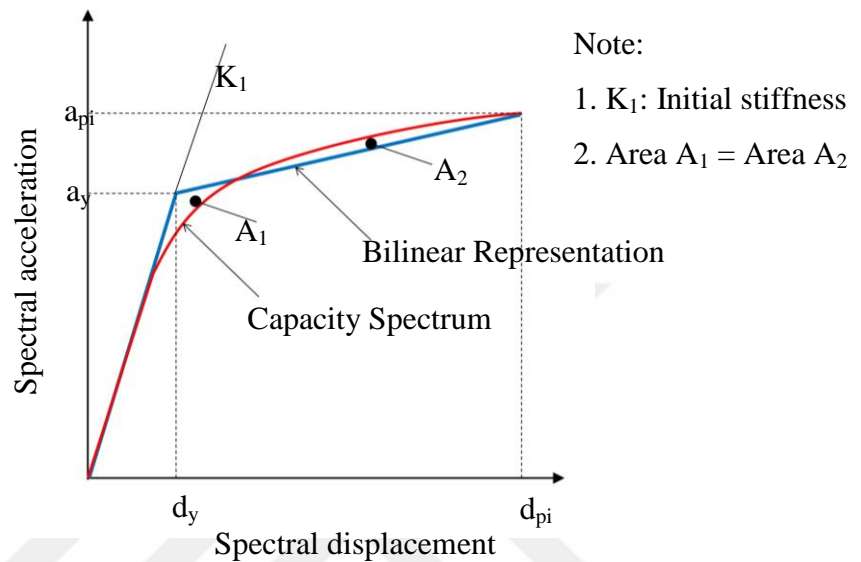


Figure 2.34. Bilinear representation of capacity spectrum for capacity spectrum method. ATC 40 (1996)

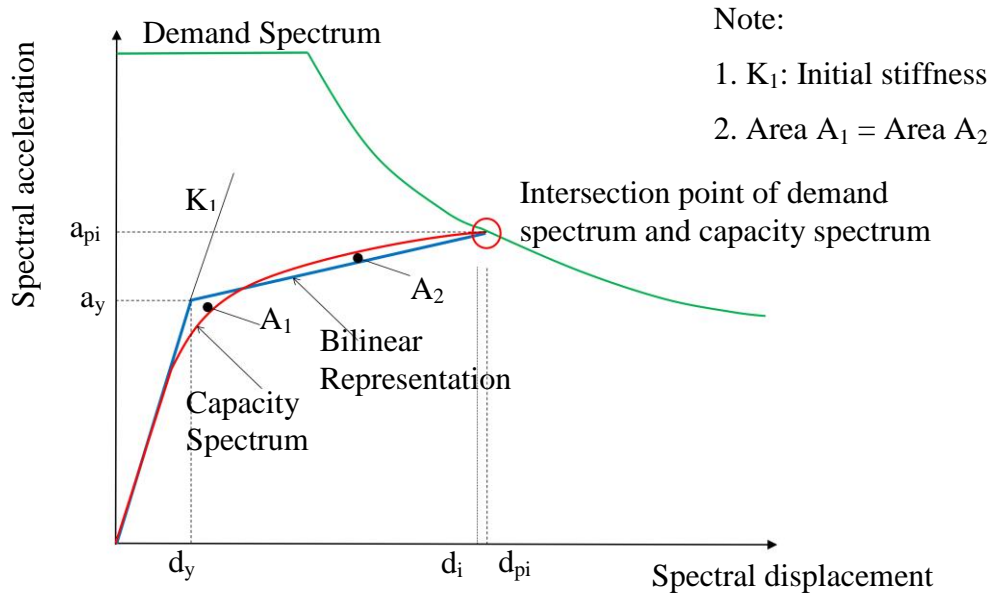


Figure 2.35. Performance point determination. ATC 40 (1996)

According to ACT 40 (1996) lateral deformations at the performance point displacement are to be checked against the deformation limits stipulated (Table 2.10).

Table 2.10. Deformation Limits, ATC 40 (1996)

Inter-story Drift Limit	Performance Level			
	Immediate Occupancy	Damage Control	Life Safety	Structural Stability
Maximum Total Drift	0,01	0,01-0,02	0,02	$0,03V_i/P_1$
Maximum Inelastic Drift	0,005	0,005-0,015	no limit	no limit

In Table 2.10, Maximum Total Drift is defined as the inter-story drift at the performance point displacement. Maximum Inelastic Drift is defined as the portion of the maximum total drift beyond the effective yield. Immediate Occupancy (IO): there is no occurrence of structural and non-structural damage and the structure is able to overcome the ground motion. Damage Control (DC): the structure can be damaged by not be collapsed. Inside living does not face problems. Life Safety (LS): The structure is still able to withstand the ground motion and minimum damages are captured. Living is safe. Structural Stability or Collapse Prevention (CP): The structure is extreme damaged but not completely collapsed.

2.1.6. Finite element method – ABAQUS CAE

2.1.6.1. Finite element method

According to Robert (1994), the FE method is considered as approximate numerical solution for a specific problem maybe in stress analysis, in thermal analysis and fluid flow etc. The method is dividing a structure into a number of small and simple elements, solving elements separately and then connecting them at nodes holding the elements together. Versatility is considered as the power of finite element method due to the ability to analyze a structure with arbitrary shape working under arbitrary loads and arbitrary boundary condition. An example of model defined by finite element method is shown (Figure 2.36).

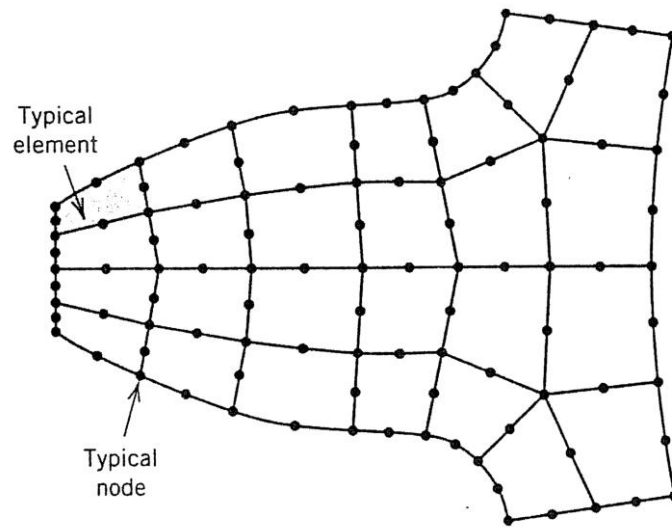


Figure 2.36. Nodes and elements of a gear tooth. Robert (1994)

Finite element method uses matrix symbolism is $K.D = R$, where D is an unknown vector, R is vector of known load and K is a matrix of known constants and in stress analysis K is called as a stiffness matrix. Commercial software using FEM consists of matrix manipulations, numerical integration, equation solving and other procedures applied automatically according to Robert (1994). The user of commercial software cooperate with pre-processing such as defining the geometry of structures, materials, loads, boundary conditions, mesh sizes etc. and post-processing including storing output data, illustrating the data etc.

Before running a software applied FEM, the user should keep in mind that FEM is a implementing of mathematical theory of physical behavior and the following questions should be answered in order to avoid mistakes and unrealistic situation.

- What kinds of and how many of elements should be used?
- How small element should be meshed, where is mesh should be fine and where is maybe coarse.
- Which is suitable model used to define materials?
- The analysis is static or dynamic? etc.

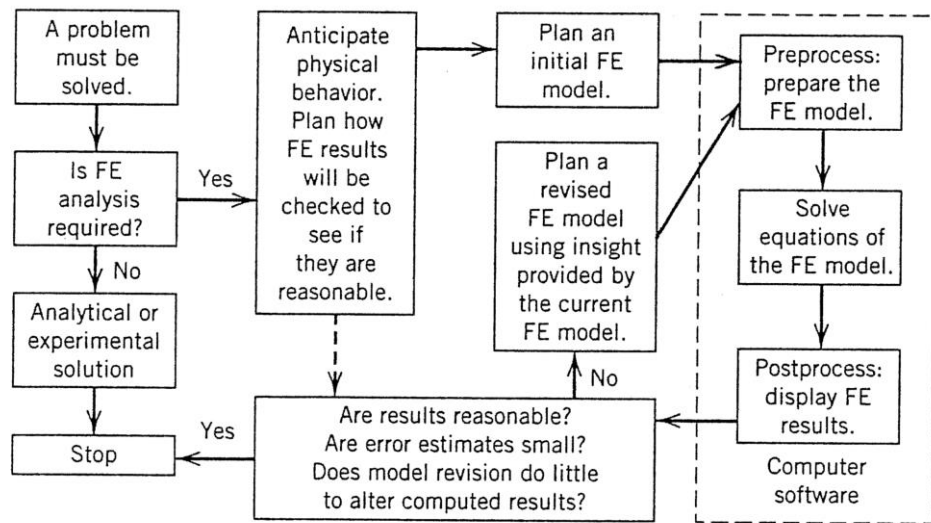


Figure 2.37. Outline of FE analysis project. Robert (1994)

2.1.6.2. Commercial package Abaqus CAE

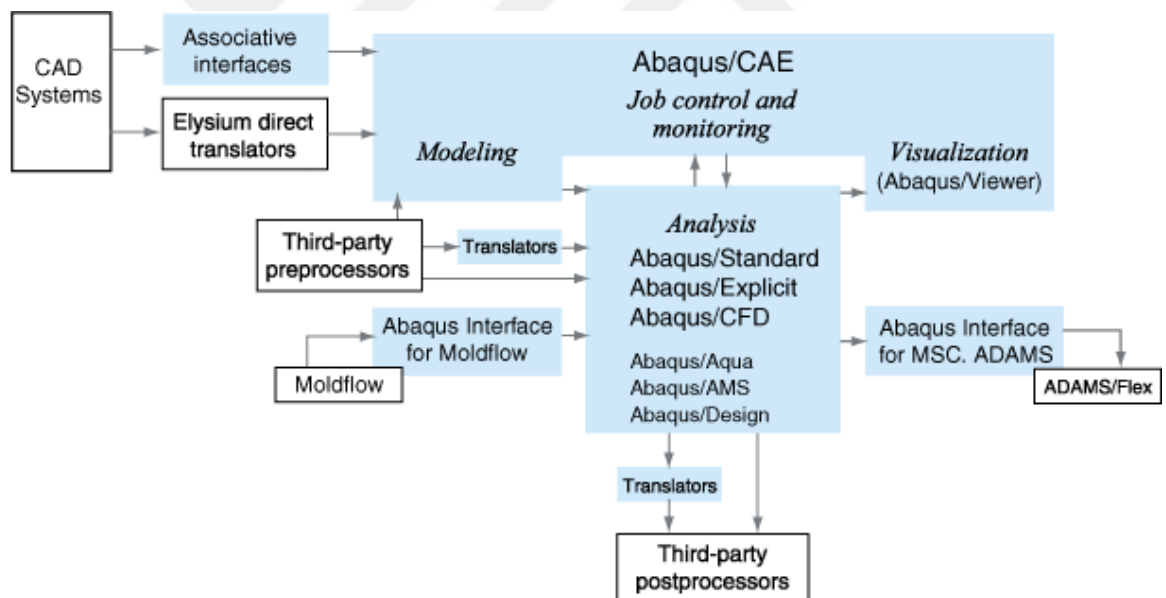


Figure 2.38. Suite of finite element analysis modules. Dassault Systèmes (2013)

Abaqus/CAE incorporates the analysis modules into a Complete Abaqus Environment for modeling, managing, and monitoring Abaqus analyses and visualizing results. Abaqus/CAE is evaluated as a powerful tool for structural analysis with tremendous advantages according to Dassault Systèmes (2013).

- Integrates modeling, analysis, job management, and results evaluation seamlessly.
- Provides the most complete interface with the Abaqus solver programs available.
- Uses neutral database files that are machine independent.
- Can be customized to create application-specific systems.

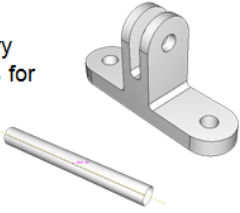
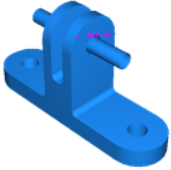
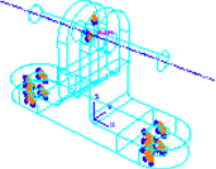
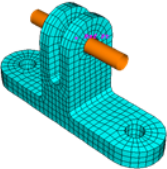
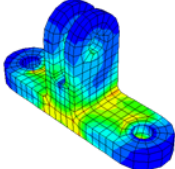
Part	Property	Assembly
<ul style="list-style-type: none"> • Create the part geometry (and regions for sections, if necessary) 	<ul style="list-style-type: none"> • Define materials • Define additional part regions • Define and assign sections to parts or regions 	<ul style="list-style-type: none"> • Position parts for initial configuration. 
Step	Interaction	Load
<ul style="list-style-type: none"> • Define analysis steps and output requests 	<ul style="list-style-type: none"> • Define contact and other interactions on regions or named sets, and assign them to steps in the analysis history 	<ul style="list-style-type: none"> • Apply loads, BCs, and ICs to regions or named sets; and assign them to steps in the analysis history 
Mesh	Job	Visualization
<ul style="list-style-type: none"> • Split assembly into meshable regions and mesh 	<ul style="list-style-type: none"> • Submit, manage, and monitor analysis jobs 	<ul style="list-style-type: none"> • Examine results 

Figure 2.39. A modeling process in Abaqus. Dassault Systèmes (2013).

2.2. Literature Review

Abbas et al. (2014) applies reversed cyclic loading history to external column-beam joint (T shape) in Abaqus program using a 20mm thickness steel plate in order to avoid stress concentration and premature failure in simulation. In simulative models, the concrete medium was modelled with a dense mesh of 8-node brick finite elements with 50 mm size meshing. According to the results, in case of cross shape joint, failure in simulative models occurred earlier than in experimental with lower deformation up to

20%. It could be explained that in experimental tests, there are some alternative resistance mechanisms working under vibration that are ignored in analytical definition.

Alhadid and Youssef (2016) evaluate RC jacketed RC beams considering the effect of interfacial slip effect from elastic stage to nonlinear behavior range. An iterative calculation algorithm was used for moment-curvature relationship and load deflection of a bending beam with considering slip distribution, shear stress distribution and the influence of surface roughness condition. The interfacial-slip model was built based on the summation of concrete contribution i.e. adhesion, aggregate interlock and friction. The friction force between two substrates is affected by the roughness of surfaces, normal pressure. In the proposed calculation algorithm, the author suggested the initially assumed value of friction coefficient is 0,4 for smooth and 1,4 for intentionally roughened surface. According to the results, the author concludes that the increasing of jacket thickness leads to the increasing of capacity and flexural ductility especially for three side jacketed beams. Increasing the span causes the reduction of ultimate capacity and stiffness while increases ductility. Consequently, the friction force increases due to the larger interacting surface and the lower relative displacement between two surfaces is witnessed consequently. Higher compressive strength results in lower slip reduction rate in range of elastic as a consequence of the fact that at the surface more surface friction are witnessed.

Altun (2004) indicates that concrete jacketing method improves the resistance against seismic conditions and is considered enhancing the durability of structural members. The study introduced an equation used to calculate ultimate moment considering the contribution of longitudinal reinforcement in host and cover part of jacketed beams. The jacketed RC beams behave similarly to the ordinary RC beams from the beginning till the ultimate failure. 10 cm thickness concrete jacket is commonly used for damaged structures, the author indicated.

Aslani and Jowkarmeimandi (2012) describe the behavior of concrete applied to monotonic as well as cyclic loading in compression and tension such an envelope curve (for monotonic and cyclic loading), an unloading curve, a reloading curve and a

transition curve. Formulations established to predict the stress-strain relation in compression and tension in FE environment results in a good fit to experimental results. Besides that, the author claimed that the tensile strength of concrete members without premature damage in compression can be assumed equal to 10% of its compressive strength.

Badoux and Hulsbos (1965) show that there are some important points that were inherent and developed in terms of interface surface strength. First, shearing strength decreases when the ratio of shear-span and effective depth of section (a/d) increases (Mattock and Kaar). Based on empirical tests series, it can be concluded that the interface joint strength does not depend on a/d ratio as much as obtained by previous equations for static tests. Then, the authors claimed that the a/d ratio does not influence on the effectiveness of the joint reinforcement while plays a decisive role in the natural bond strength that should be considered when evaluating the concrete on concrete interface surface joint. Second, an increase in concrete strength increases slightly the ultimate shear stress in the joint according to Saemann and Washa test series. Next, 0,005 in. slip, obtained by Wisconsin test series and known as critical slip causing the loss of composite action, is considered conservative and is increased to 0,01 in. (0,254mm) by the proposed study. The study applied cyclic loading with rate of 250 cycles per minute in order to evaluate the fatigue of bending beams, especially interface surface strength. Under cyclic loading, a residual slip was witnessed when slip never came back to zero when load was removed. Besides that, the authors indicated that the strength of interface surface under bending condition is lower than the result obtained by push-out test. Furthermore, in this study, friction force is considered contributing to interface surface immediately after the moment of loss of the natural bond strength. Consequently, the interface surface strength cannot be superimposed the contribution of the natural bond, of the reinforcement, and of the friction.

Belejo et al. (2012) evaluates the deviation of SAP2000 and SeismoStruct's results when applying pushover analysis to a spatial structure. Although there are some types of plastic hinge model defined in SAP2000 FEMA-356 (FEMA, 2000) or on CALTRANS (CALTRANS, 2009), none of results, especially base shear versus displacement curve,

was close to the reference's result. It could be understood that, lumped mass is defined in SAP whereas distributed mass is considered in SeismoStruct. Uncoupled M2/M3 hinge model in SAP2000 underestimates target displacement result possibly because of the absence of PM effect. Moreover, different hinge models lead to different deviation in terms of inter story drift rate between them inside SAP2000 and SeismoStruct program. To put in the nutshell, the author claimed that the hinge definition based on FEMA356 in SAP2000 definitely not suitable for 3D RC structure, especially asymmetric plan building under high PGA level. Conversely, hinge models defined through fiber elements results in more accurate and satisfactory results and leads to the most acceptable seismic behavior of structure objected to low PGA intensities.

Cheong and Macalevey (2000) set up a dynamic test consisting of a static cyclic pushover test by applying 100,000 or 1,000,000 cycles of dynamic load from $0,2P_{ult}$ to $0,6P_{ult}$, where P_{ult} is the theoretically assumed static failure load of an equivalent monolithic beam, was set up. In general, the jacketed beam behaves in the same way as monolithic members in terms of the progression of appearance of the first crack, deflection behavior, strains recorded in the reinforcement, and ductility. Moderate dynamic loading applied to a jacketed beam does not cause a significant reduction in the load capacity of jacketed beams. Besides that, partially roughening does not result in remarkable load capacity in comparison with fully roughened beams.

Genikomsou et al. (2015) indicate that modelling accurate materials, especially concrete, plays a decisive role in resulting in a realistic results. The dilation angle of concrete model is considered as a critical aspect affecting the results. The authors observe punching shear response of slabs by FEA where CDPM is applied with necessary parameters such dilation angle ($\psi=40^\circ$), flow potential eccentricity ($\epsilon=0,1$), ratio of strength of concrete under biaxial compression to the strength under uniaxial compression ($f_{b0}/f_{c0}=1,16$), ratio of strength of concrete under biaxial compression to strength under tri-axial compression ($K=0,667$) and viscosity parameter ($\mu=0,00001$). The value of the viscosity parameter depending on the time increment step should be set around 15% of the time increment step in order to get accurate results. Furthermore, a

limit value of 0,9 is set up for damage parameter in case of compression and tension. A good agreement is captured when comparing simulative results to test results. According to the results, the authors conclude that a mesh size of 20mm leads to the most realistic results while 15mm size is considered to be so small and 24mm size seems to be too coarse.

Gohnert (2000) introduces a proposed theory to calculate horizontal shear stress at the interface surface between precast and in-situ concrete of a flexural beam. First, the maximum shear stress was built theoretically for cracked section and un-cracked section at the interface surface. Secondly, push-off test was applied by pushing the in-situ part until shear failure occurrence at the interface surface and an empirical equation was also set up. Based on experimental results, the two proposed equations predict shear failure value more accurate than shear resistance at interface surface of concrete carried out by ACI 318, BS 8100 and SABS 0100.

Gromysz (2008) describes a joint surface model, interface surface, in which after horizontal critical shear stress is reached, friction force appears as a consequence and keeps the stress constant even external force increases. Based on numerical test, the author claimed that the delamination in concrete on concrete joint surface affects vibration frequency and as well as damping of vibration. The vibration of composite member is affected by viscous damping factor (c) and damping force (R), however, viscous damping (c) plays a decisive role. In event of small boundary of frictional stress, composite member fades slower than monolithic one due to the fact that vibration period of composite member is higher than monolithic one. Furthermore, it is noted that with high boundary of horizontal stress at interconnection, the energy in composite member is dissipated more quickly than in monolithic member.

Hassanean et al. (2013) apply Γ shaped 4mm diameter shear connectors with dimensions of 50mm and 20 mm sides on the concrete-to-concrete interface surface of strengthened beams using steel fiber strengthened Π shaped RC jackets. Furthermore, high tensile steel rivets of 520 N/mm² yield strength have end screw with a length of 25 mm. The ratio of shear connectors on surface is about 0,066%. Each Γ shaped connector

is embedded in the core part with a length of 28mm while the other 20mm long part is left outside. The effect of the thickness of RC jackets is considered changing the thickness of the bottom part from 30mm to 50mm while two side parts are kept constant, 30mm. The specimens are tested using three-point bending scheme where repeating concentrated load (P) is considered. The maximum load is enhanced 25%, 45%, and 75% for RC jacketed beam with the thickness of bottom layer of 30mm, 40mm, and 50mm respectively.

He et al. (2017) show that mechanical strength of new-to-old bonded concrete consisting of the tensile splitting strength, the flexural strength and the bond strength is linearly dependent on the interface roughness. It is evident that mechanical strength increases when surface is artificial roughness is created due to the increase of interfacial fractal dimension. Sand-blasting is considered as the best surface preparation procedure.

Hindo (1990) introduces an in-place direct tensile test, called LOK-TEST pullout, successfully controlling overlay and patch work in situ by using two methods of surface preparation to achieve high bond strength: pneumatic hammer and hydro-demolition, also called hydro-blasting or hydro-jetting. According to the experimental data, surface prepared by using hydro demolition works twice times well compared with one prepared by pneumatic hammer method due to the fact that no damage was witnessed when the first one was applied whereas latter technique weakened the zones below the interface. Bond strength depends on the depth of bruised layers, the type of bond material, the quality of surface preparation and the type of concrete. ACI committee 503 stipulates that minimum pullout strength of 100 psi (0,69 MP(a)) must be developed at prepared surface to achieve adequate bending.

Hsu and Hsu (1994) set up a series of compression tests using 3x6 in (76,2x152,4mm) cylindrical specimens to determine the complete stress strain behavior for high-strength concrete with or without tie confinements. Modulus of elasticity was considered as the secant slope of the uniaxial stress-strain curve at a stress level of 45% of the compressive strength. Based on experimental results, the authors concluded that the

constant values of 0,002 and 0,003 for the strain corresponding to the peak stress and the ultimate strain, as specified by ACI committee 318, are conservative.

Huang and Gould (2007) assumes that Modal Pushover Analysis (MP(A) is able to capture the behavior of tall and asymmetric-plan building under two directions of ground motion. The article indicates that the prevailing effects of the fundamental frequency and the ignorance of vertical component of ground motion caused the discrepancy of MPA and nonlinear time history analysis (NTHA) in terms of top displacement and damaged patterns, particularly the intensity and location.

Ismail (2014) evaluates the seismic response of existing buildings by comparing the original with the retrofitted one by using full steel jacket, partial steel jacket and RC jacket. Based on the results, all retrofitted jacketing techniques enhance the strength and the ductility of structures especially steel jacketing and RC jacketing. Besides that, the fundamental period of retrofitted building decreased significant and the modification factor improve remarkably due to the increase of lateral stiffness. Besides that, carbon fiber reinforced polymer (CFRP) composite is more preferable if the remaining of elements dimensions is required.

Julio et al. (2004) proves the strongly existent correlation between bond strength in tension and bond strength in shear at the interface surface of added and substrate concrete with a correlation coefficient of $R^2=0,948$. The result can be used conveniently in the future when considering the bond strength in tension and in shear of concrete layers. In case of bond strength at interconnection, a saturated substrate with a dry surface was considered to be the best way to achieve strong bond or adhesion in shear and in tension. Besides that, higher compressive strength of concrete plays an important role in increase the bond strength. Particularly, the compressive strength of added concrete is quite higher than that of concrete substrate, monolithic failure maybe happens. It is worth noted that the more different age between added concrete and concrete substrate, less strength in bond. For the surface preparation, among roughening techniques, sand-blasting causes highest bond strength in tension and in shear.

Júlio and Branco (2008) evaluate experimentally and analytically the ultimate bending moment under cyclic load of a RC jacketed columns. Monolithic behavior of jacketed elements is the objective of previous studies. The previous authors concluded that, with thickness of jacket less than 17,5% width jacketed column, if the ration of bending moment to shear force is greater than 1,0m (3,281 feet), the jacketed column will behave as a monolithic composite element. It is worth noting that, the out of phase localizing of the stirrups of jackets and core column is necessary to obtain monolithic behavior of member. In experimental test, columns were applied to predefined displacement histogram. It should be noted that the axial load was constantly applied throughout lateral forcing. The history of imposed displacement is applied based on recommendation of European Convention for Constructional Steelwork that presents clearly about the progressively increasing amplitude of displacement in each cycle, particularly 8 steps. Furthermore, lateral displacement was imposed slowly with velocity of 0,1mm/s. From the experimental investigation, the author concluded that the interface preparation does not affect the result too much and models can be considered working monolithically. In case of analytical test, a delamination model was considered at the interface surface under the pushover test. The lateral load was applied to using an epoxy bonded steel disc at the top of core. Based on the load - displacement curve, it can be concluded that numerical pushover test result is higher capacity than experimental test at the same column. Besides that, to obtain total adherence between core and jacket parts, increasing the roughness of the interface surface with sandblasting, epoxy resins and bonding agent like steel connector were considered. Besides that, self-consolidating high-strength grout has been applied to reduce the thickness of jackets.

Kang et al. (2015) examine analytically concrete-to-concrete shear resistance of specimens consisting of two layers of concrete that the interface is indented with the height of 6mm and 10mm as stipulated by Eurocode. It is found that in case of smooth surface as well as application of indented surfaces the shear resistance obtained by simulative modeling is higher than the results calculated by code, about more than 1,3 times. Moreover, the class strength of concrete layers can affect the shear strength at the interface. For specimens with 30MPa strength concrete layers, the shear resistance is

slightly higher for 10mm indented surfaces. However, when the compressive strength is used differently for the bottom and top substrate, 80MPa and 30MPa respectively, the shear strength of both situations seem to be identical to each other. Furthermore, girder specimens are built in order to evaluate the shear strength at the inter-concrete interface surface between concrete casing and slab with variable of surface rough conditions. It is noted that shear connectors are applied to all of specimens. The experiment shows that the specimen not roughened performs higher peak load, about 6%, than the design value while the one considered as rough as well as the one with 6mm high 40 mm width 40mm distance intentional indents underestimate compared with design load, 8% and 6% respectively.

Khalil et al. (2016) evaluates the beams strengthened by Ultra High Performance Strain Hardening Cementitious Composites (UHP-SHCC) with the ratio of 0,3 to 0,6% of reinforced steel and steel reinforcement under both monotonic and cyclic loading. In Abaqus, for concrete, load strain curves in terms of uniaxial load and compression consisting of linear range and softening are described as plastic behaviors of concrete using two plastic variables d_t and d_c that are functions of plastic strain, temperature and field variables. Those variables value vary from 0 to 1 corresponding to from elastic or undamaged to total loss strength events. In the case of reinforcement, embedded region modelling is chosen. It should be noted that the effect of bond slip is not considered in the embedded region modelling but somewhat will be defined as tension stiffening behavior of concrete. The author reminded again that the dissipated energy is the area enclosed by the hysteresis loop and represents the structural element capacity to mitigate the repeated loading effect which causes excessive cracking and permanent deformation. It is worth noting that the energy dissipated in the first cycle is greater than the subsequent due to the fact that the crack development, widening and propagating occurred in the first cycle. Thereafter, fibers work as energy dissipater and the crack just opens and closes under alternate cyclic load.

Kothari et al. (2017) evaluates the seismic response of structures observing results obtained by nonlinear dynamic analysis using shake table and nonlinear static pushover test compared with time history function. In experimental tests, the capacity curve

resulted by shake table test is lower than pushover test due to the fact that cyclic loading causes loss of strength and stiffness of members. Besides that, hysteresis energy dissipation causes the lower backbone curve of spectral acceleration cyclic analysis than monotonic loading analysis.

Kwon et al. (2009) analyzes the shear behavior of rectangular-shaped asperities at asperity-level considering geometry variation and compare the results to experimental test on artificial rock joints. The dimensions of asperities decide its failure mechanism such dilative or non-dilative mode.

Lampropoulos and Dritsos (2011) show that shear stress and friction coefficient depend on the normal stress at interface surface. It is noted that, normal stress is different from node to node on the surface and hypothesis indicates that friction coefficient is constant. RC columns strengthened by RC jackets are investigated using FE analyzes under monotonic and cyclic loading. Shrinkage at the interconnection resulting in lower value of maximum load and the stiffness of jacketed column was considered through using two different thickness jackets, 35mm and 75mm. As predicted, the model considering concrete jacket shrinkage according to ACI 209R-92 reduces the strength capacity of jacketed columns and is well fit with the experimental capacity curve drawn thorough cyclic test. Shrinkage effect is more profound for the thicker jacket. According to the results, moreover, the author concluded that perfect bond models leads to significant errors. For practical purpose, the capacity can be calculated using monotonic test and then possibly is transferred for cyclic test by multiplying reduced factor, 0,9 for non-shrink grout and 0,8 for normal concrete used for jackets.

Lee and Polycarpou (2007) conduct an experimental study to measure the static friction coefficient under constant normal load. The empirical result was compared with the theoretical friction coefficient obtained by KE model (Kogut and Etsion) which was valid for dry interfaces and did not capture any dynamic velocity effects. Based on the results, the authors concluded that the constant Coulomb friction assumption may be valid. Besides that, by considering linearly sliding velocity in case of smooth dry interface, the study indicates that slower velocity causes decrease from static to kinetic

coefficient of friction, known as static-to-kinetic friction transition, more clearly than higher velocity as a consequence of the fact that under slow displacement rate, the static friction force has time to be built up as asperity junction growth resulting in a larger friction decrement from static to kinetic values. It is worth noting that higher displacement rate is applied, slower the static coefficient of friction is obtained. Dynamic effects may play a more significant role in case of faster velocity.

Lee and Fenves (1998) introduce a new plastic-damage model for cyclic loading developed using the concept of fracture-energy based damage similar to the Barcelona model. The authors showed that the effect of compressive damage on the yield surface and the elastic stiffness are not affected considerably by the tensile damage (stiffness recovery) while the stiffness degradation accumulated by the compressive damage is not recovered during tensile unloading because the compressive failure mainly is caused by dilatancy (dilatation), which affects both compressive and tensile strength. It is noted that the stiffness recovery takes place only when the tensile cracks are closed. The hysteresis curve in the tensile region is negligible compared with the compressive regime.

Mahmoud et al. (2013) indicate that the presence as well as the ratio of shear connectors influences directly the shear transferability at the interfacial surface between composite concrete decks, particularly between precast beams and cast in-situ slabs. Based on experimental and analytical results it is proved that concentrating the connectors at the vicinity of the supports enhances the ductility of the beam due to the fact that the shear forces increase at areas near supports. Specimens strengthened using 0,2% shear connectors perform at approximate 46% the ultimate load capacity of the monolithic one while the value is about 68% when 0,3% ratio of shear links are applied. The stiffness of beams is enhanced using higher ratio (0,3%) as well as larger diameter (6mm) of shear links more than applying 4mm diameter connectors and 0,2% surface crossing reinforcement.

Mazizah and Izni (2015) evaluate the influence of shaped irregularities at and shear connectors crossing the interface between concrete substrates casted at different times.

Experimental tests show that in case of specimens applied shear links the shear failure does not happen suddenly as the one without projecting shear connectors. The amount of shear friction reinforcement and the surface texture play a decisive role in enhancing the shear strength of the concrete-to-concrete interface. The clamping stress produced by dowel action when applying shear connectors increase the shear strength of the interface in comparison with specimen left with smooth surfaces. The author indicate that the application of shear friction reinforcement possibly upgrades the friction coefficient up to 0,87 higher than the value of 0,6 applied for both smooth and surface strengthened by shear ties as stipulated by Eurocode 2.

McCrum et al. (2016) set up a pushover test on a typical moment resisting frame in Europe with necessary parameters such as soil type, peak ground acceleration and a behavior factor. In the study, according to research on CDPM, the constitutive parameters used to define yield surface and flow potential surface of concrete in Abaqus are: dilation angle ($\psi=36^\circ$), flow potential eccentricity ($\varepsilon=0,1$), ratio of strength of concrete under biaxial compression to the strength under uniaxial compression ($f_{b0}/f_{c0}=1,16$), ratio of strength of concrete under biaxial compression to strength under tri-axial compression ($K=2/3$) and viscosity parameter ($\mu=10^{-7}$). It is worth noting that, according to EC8, the actual collapse of structure based on engineering judgement and assessment of the stress distribution in the structure at the final time step is estimated approximately the roof displacement of 350mm known as “pushover ext.” portion of the curve while the displacement of 238,33mm was obtained using Abaqus.

Minafò (2015) concludes that the simplified analytical method is considered as a useful tool in investigating strength domain of jacketed columns can be used by hand in combination with monolithic coefficient and safety factor considering shrinkage effect. Furthermore, the reduction on the effectiveness of composite column depends on how the interface surface is roughened, 10% for no surface preparation and can be neglected in case of well-roughened.

Münger et al. (1995) claim that reinforcement to cross the bond interface in order for shear transfer to occur, a necessary condition for the monolithic design of the section. A

trussed framework analogy segregated into tension and compression lines of action is used to explain the action of shear connectors whose diameters are less than 20mm at the concrete-to-concrete interfaces. A tensile force initiates along to the connectors at the moment of the opening of the bond interface. On the other hand, the shear resistance of shear links is considered more accountable if the interface surface is smooth. The effect of surface roughness has an upper limit which is given by fracture of the new or the old concrete adjacent to the interface zone. A kind of shear connector namely Hilti Jumbo-Nail is considered to prevent as well as eliminate de-bonded interconnections.

Najafgholipour et al. (2017) models internal and external column-beam joints in Abaqus according to some previous empirical experiments. In case of materials, concrete damage plasticity model is chosen to define for concrete considering nonlinear behavior of structure. Particularly, dilation angle ($\psi=35^\circ$), flow potential eccentricity ($\varepsilon=0,1$), ratio of strength of concrete under biaxial compression to the strength under uniaxial compression ($f_{b0}/f_{c0}=1.16$), ratio of strength of concrete under biaxial compression to strength under tri-axial compression ($K=0,667$) and viscosity parameter ($\mu= 0,007985$). In load and boundary menu, the compressive axial load was applied to the column top surface in the initial step propagating constantly throughout the analysis. The monotonic load was defined in the next step. For meshing, invariant 40mm size meshing assumed as the optimum choice based on previous tests is applied for both concrete and reinforcement.

Nasersaeed (2011) says that RC columns retrofitted using RC jackets possibly perform monolithically when a higher percentage of transverse reinforcement is used, particularly stirrup distance is set equal to half of the spacing of the original column transverse reinforcement.

Oñate et al. (1998) describe a potential function defined identically to the modified Mohr–Coulomb yield surface but using a more realistic angle of dilatancy ψ instead of the internal friction angle ϕ . The typical values of dilatancy ψ for concrete are assumed varying from 8° to 15° .

Poleswara et al. (2017) indicate that Nonlinear Pushover Analysis (NPA) results in approximate accuracy in case of low rise, stiffer and short period framed structures where just fundamental mode is considered and the others are neglected. Besides that, exact selection lateral load distribution plays an important role in leading to acceptable results. However, with high-rise building or flexible systems the deviation between NPA and full non-elastic behavior analysis is significant.

Ren et al. (2014) applied CDPM to simulate 3D model of partial-depth precast prestressed concrete bridge decks under increasing static loading. Particularly, dilation angle ($\psi=38^\circ$), flow potential eccentricity ($\varepsilon=0,1$), ratio of strength of concrete under biaxial compression to the strength under uniaxial compression ($f_{b0}/f_{c0}=1,76$), The ratio of the second stress invariant on the tensile meridian, $q(TM)$, to that on the compressive meridian ($K=2/3$) and viscosity parameter ($\mu= 0,0005$). Based on extensive trials, higher value of viscosity makes structures harder while lower viscosity parameter is assumed to result in good convergence and higher accuracy but computational cost increases. The steel reinforcing bars are embedded into surrounding concrete considered as the host parts. According to the interactive module, reinforcing bars are only able to translate and rotate completely equal to the movement of host parts. The deviation of 6% and 10% between simulative results and empirical experiments is captured in case of failure load and mid-span displacement.

Santos (2009) evaluates bond strength of including substrate surface preparation, differential shrinkage, interface stiffness and failure mode. Shear-friction theory considering four fundamental parameters: compressive strength of the weakest concrete, normal stress at the interface, shear reinforcement crossing the interface and roughness of the substrate surface was applied. The shear friction theory assumes that the transfer mechanism of shear forces at a concrete-to-concrete interface subjected simultaneously to shear and compression forces is ensured by friction only. There are two different transfer models commonly used: shear transfer across an initially cracked plane and shear transfer across an initially un-cracked plane. When adhesion maximum load capacity is reached, de-bonding occurs at the concrete-to-concrete interface and the shear stresses will be transferred by mechanical interlocking. If the interface is

subjected to compression, the shear stresses will be transferred by shear-friction. With the increase of the relative displacement between concrete parts, the reinforcement that crosses the interface will be tensioned and yielding can occur. Therefore, the shear reinforcement will induce compression at the interface and the shear load will be transferred by friction. Due to slippage, the shear reinforcement will also be subjected to shear, usually named as dowel action. The author introduced different interface surface failure modes, adhesive failure (interface de-bonding) and cohesive failure (monolithic behavior) by analyzing slant shear test results based on the Mohr-Coulomb criterion. The failure models of composite member are possibly changed because of differential stiffness that should be taken into account. The author noted that the Young modulus of added layer should not be lower than substrate concrete. The author stipulated that for left as cast concrete surface, coefficient of cohesion is 0,74 and 0,59 and coefficient of friction is 1,18 and 1,1 for laboratory and for external conditions respectively. It is worth noting that under fatigue and dynamic conditions, the values for coefficient of cohesion c halved according to 6.2.5 note in Eurocode 2 (2004) should be neglected when calculating design shear resistance at the interface surface. 2D laser roughness analyzer considered more accurate than TDI method and others was used to determine the texture of interface surfaces. Wire-brushing, sand-blasting, shot-blasting, hydro demolition and chipping are some common used method for surface preparation.

Santos et al. (2007) evaluate the roughness profile of the substrate surface in shear and in tension, measured with slant shear and pull-off tests. Based on slant shear test results, the author indicated that bond strength in shear of as left concrete layers (50,40 MPa and 46,22 MPa) is 1,30 MPa and bond strength in tension is 0 MPa.

Sengottian and Jagadeesan (2013) claim that it can be noted that the RC jacketing method is an efficient technique to repair and rehabilitate damaged columns. The efficiency depends on monolithic behavior of composite section possibly increased by using epoxy resin for instance. The load carrying is found higher than conventional columns based on uniaxial stress-strain curve and load-lateral displacement relationship when considering slenderness of columns.

Shehata (2009) investigates bending beams strengthened using partial jacketing with trapezoidal RC formworks and expansion bolts as shear connector. In general, in RC beams, the shear stress can be transmitted across the connection by adhesion, by shear-friction at the interface surface and by the dowel action of reinforcing bars. According to the results, the author concluded that with jacketing the composite section acts monolithically even until the yielding of reinforcement and enhances the bending capacity of strengthened beams. Besides that, it is noted that concrete does not provide any contribution to the shear resistance of the connection that agrees with the modified Mohr–Coulomb criteria of failure for concrete.

Tahsiri et al. (2015) concludes that RC jacketing enhances flexural capacity by section enlargement as well as using extra longitudinal bars and ductility of strengthened beams under seismic condition. The error is about 23% for RC jacketed beams due to the difference between analytical and experimental in terms of ultimate flexural bending moment.

Thermou et al. (2014) indicates that RC jacketing is arguably the most appropriate intervention method for providing uniformly distributed lateral load capacity throughout the structure. In the study, shear resistance mechanisms were used to describe the interface surface between old and new concrete layers including aggregate interlock, friction and dowel action. Friction coefficient was chosen as 0,4 according to the Greek code for interventions. An analytical algorithm was introduced to calculate the flexural behavior under reversed cyclic loading. Particularly, in case of analytical model of slippage, for flexural analysis, the whole section is divided into three layers deforming with the same curvature and perfect bond between reinforcement and concrete was assumed in order to avoid more complicated analytical model. Besides that, for flexural beam, the resultant force on two vertical surfaces was neglected due to the fact that compression and tension over the height of the segment is almost equal and the resultant force is close to 0. It is worth noting that differential shrinkage resulting on reduction in compressive strength of concrete because of biaxial stress at interconnection was considered as consequence of the fact that the concrete dries out, then tensile stress appears at and perpendicular to interface and causes cracking eventually. The

differential shrinkage is indirectly taken into account by utilizing the proposed model by introducing a reducing value applied for the concrete compressive strength.

Thermou et al. (2007) introduces a calculation algorithm to evaluate the parameters relevant to composite behavior jacketed RC member through a flow chart. According to the comparison between analytical and experimental results, the author claims that the behavior of jacketed members is greatly sensitive to the interface slip definition. The study claims that increasing friction coefficient leads to higher shear capacity at the contact surface allowing for the development of higher strength and curvature values. For practical purpose, the study indicates that the capacity of monolithic member can be multiplied to a multiplier called monolithic factor, ranging from 0,7 to 1,0 and defined in some codes, to determine the capacity of composite member. In order to determine the parameters relevant to monolithic factors for flexural strength, curvature and ductility, the author adjusted the shear span ratio to have two kinds of bending beam, known as dominated by moment and dominated by shear force. According to results, the author indicated that flexural dominated members are more sensitive to the change of the ratio of longitudinal bars and axial force than members dominated by shear force in case of yielding. The parameters affecting the monolithic factors are the ratio longitudinal reinforcement, axial load, confining reinforcement (stirrup). Additionally, the axial load N applied on the jacketed cross section expressed as a fraction of the theoretical crushing capacity ($A_g f'_c$), cylinder compressive strength, of the jacketed cross section which varied between 0 and 0,3.

Truong et al. (2017) uses 51 mm thickness reinforced jacket in order to enhance the initial stiffness, strength and deformation capacity of strengthened columns. Cyclic load was applied vertically while 1000kN axial load (30% of the axial load carrying capacity) was constantly applied at the top of specimens. Reversed cyclically load history was applied to columns built based on ACI 374.2R-13. In general, retrofitting method improves the hysteresis load-drift capacity curve of column, increases the dissipated energy, causes ductile failure and increases of initial elastic stiffness compared to original columns.

Vandoros and Dritsos (2008) compare 75mm thickness shotcrete and concrete jacketed and monolithic columns using exactly the same reinforcement to each other by applying cyclic loading procedure where the amplitude increased 5mm per step. It is indicated that jacketed columns are able to keep almost monolithic behavior and the stiffness is so close together under seismic conditions. In comparison with monolithic columns, the strengthened columns without surface preparation have lower flexural capacity about 35,8% at yielding and 16,3% at ultimate point. Premature failure and lower ductility of jacketing without surface treatment is the consequence of poor bond. Due to lack of interface bond and adhesion, the friction force at interface reduces so that columns jacketed without roughening witness faster degradation of dissipated energy capacity in comparison with columns strengthened using surface preparation methods. Besides that, jackets tend to separate the core because of no surface treatment. The failure mechanism and visible cracking are influenced by jacketing methods. Shotcrete specimen is considered better than concrete method due to fewer bond slip at interface surface. However, jacketing without surface preparation causes significant stiffness degradation even it improves the stiffness of column significantly in comparison with original one.

Wahalathantri et al. (2011) use a material model to simulate flexural cracking in RC elements in ABAQUS providing the capability of simulating the damage using either of the three crack models for RC elements: (1) Smeared crack concrete model, (2) Brittle crack concrete model, and (3) Concrete damaged plasticity model. The Nayal and Rasheed's tension stiffening model for RC elements and the modified tension stiffening model for the present study was presented. The tensile damage parameter, d_t is defined as the ratio of the cracking strain to the total strain. The compressive damage parameter, d_c is defined as the ratio between the inelastic strain and total strain. If damage parameters are not specified, the model behaves as a plasticity model. The beam is meshed with approximate element size with 50mm x 50mm x 12,5mm in longitudinal, transverse and thickness direction respectively. Result section indicates that both displacement and crack patterns obtained from FEM are well matched with the experiment results. Therefore, the above material model minimizes the number of tests needed to develop an accurate material model in FE simulation.

Wang et al. (2011) set up pure shear test in order to evaluate the shear strength of the concrete substrates where shear connectors are applied. The bond strength is enhanced most by using Π shaped steel shear ties compared to Γ and I shapes. In general, the relationship between the lateral applied load versus interfacial slip is describe from an ascending part up to an ultimate peak load with really small slip followed by an approximate plateau regime proving that the interface has good ductility behavior due to the presence of steel ties.

Zhu et al. (2016) experience push-out tests on steel-concrete interface surfaces strengthened using 16mm diameter 390 yield strength shear connectors whose ratio is about 0,16%, 0,32%, 0,48%, and 0,64%. It is evident that the change of ultimate shear capacity per stub is not enhanced obviously with the increase of the ratio of connectors.

Zou and Chan (2005) indicate that there are two same dimensional frames working under a same pushover analysis combining with different gravity loads. It is noted that the frame with lighter vertical load led to more plastic hinges and cost more than the other one. That is because lighter frame causes higher flexural moment at left columns called net tension on columns that leads to weak story.

3. METHODOLOGY AND APPROACH

The present thesis is aiming at the behavior of RC shell covered structures built in areas prone to large earthquake events. Particularly, dynamic characteristics and performance point of the structures are compared with those of a respective structure built traditionally as well as some surface treatment methods are applied in order to enhance the strength of the concrete-to-concrete interface. The first objective is evaluated experimental using Shaker test and numerically by modeling in finite element commercial software namely Abaqus. On the other hand, performance point of structures is obtained by simulative modeling. Moreover, the effect of normal loading on structure is also evaluated using numerical modelling.

The concrete-to-concrete friction model is built based on Coulombic friction model. Besides that, in order to increase the shearing strength at the interface, surface treatment methods are applied such as shear connectors, indented construction joints, and a combination of them.

3.1. Geometrics of Specimen

The structure formed using RC formworks namely NEW FRAME (NF) built spatially is evaluated comparing to a relative one namely CLASSICAL FRAME (CF) whose dimensions are similar to the dimensions of NF. Two single-story symmetric frames, CF and NF, own the same finished dimensions (Figure 3.1). Particularly, beams section is 250x300mm dimensions, and 300x300mm is dimensioned for columns. 30mm thickness RC formworks cover beam and column components in case of NF. All of longitudinal re-bars and stirrups have 8 mm diameter. Stirrups are placed at a distance of 75mm for formworks and 150 mm for core beams and columns in case of NF and for the elements of CF.

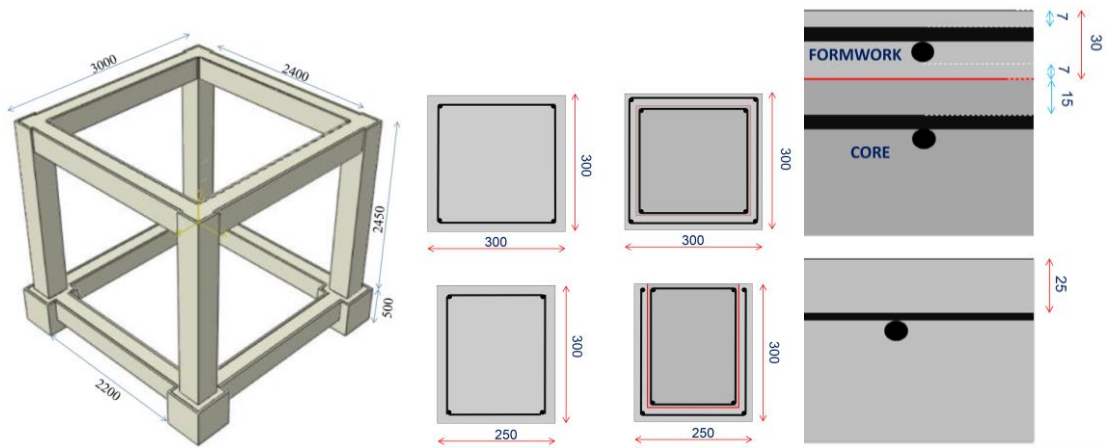


Figure 3.1. Finished dimensions of symmetric frames and cross sections in mm

3.2. Materials

3.2.1. Concrete

In the present thesis, concrete class B35 with 35MPa strength at 28 day age is applied (cylinder specimens) (Table 3.1). It is noted that, elastic range is considered when extracting the dynamic characteristics of structures while pushover analysis causes nonlinear behavior. Initially, when Poisson's ratio is concerned, Kupfer et al. (1969) states that within the region of biaxial compression a constant value for Poisson's ratio of 0,20 was calculated while the corresponding value for region of biaxial tension was 0,18. For combined compression and tension Poisson's ratio ranges from 0,18 to 0,20. Moreover, the Poisson's ratio value for concrete material is chosen 0,2 according to Najafgholipour (2017), 0,18 according to Lee et al. (1998).

Table 3.1. Mechanical properties of concrete material

Property	B35
Ultimate compressive strength (σ_{cu}), MPa	35
Tensile capacity (σ_{to}), MPa	3,5
Density, T/m ³	2,4
Elastic modulus (E_0), MPa	26987
Poisson's ratio (ν)	0,18

When pushover analysis is applied, concrete is considered to fall deeply into its inelastic regime as well as damaged under extreme large deformation of structures. In the present study, concrete damage plasticity model (CDPM) built based on Kupfer et al. (1939) and Lubliner et al. (1989). The input data of uniaxial stress-strain relation in compression is built based on Hsu and Hsu (1994) whereas the tensile regime is defined following Aslani and Jowkarmeimandi (2012) (Table 3.2). It is noted that, for simulation converge reason, the softening branch in compression of concrete is extended in comparison with the model of Hsu and Hsu (1994).

Table 3.2. Proposed Abaqus input parameters of B35 concrete

COMPRESSION			
Stress, σ_c (N/mm ²)	Strain, ϵ_c (mm/mm)	Crushing strain, $\tilde{\epsilon}_c^{in}$ (mm/mm)	Damage parameter, d_c
15,751	7,03E-04	0,00E+00	0,000
21,930	1,08E-03	2,31E-04	0,000
27,769	1,45E-03	3,01E-04	0,000
31,936	1,82E-03	3,85E-04	0,000
34,292	2,19E-03	4,86E-04	0,000
35,003	2,57E-03	1,27E-03	0,000
32,997	3,31E-03	2,09E-03	0,057
28,898	4,05E-03	2,98E-03	0,174
24,561	4,80E-03	3,89E-03	0,298
20,717	5,54E-03	4,77E-03	0,408
17,523	6,28E-03	5,63E-03	0,499
14,930	7,03E-03	6,47E-03	0,573
12,834	7,77E-03	7,29E-03	0,633
11,133	8,51E-03	8,10E-03	0,682
9,742	9,26E-03	8,90E-03	0,722
8,594	1,00E-02	9,68E-03	0,754
7,662	1,07E-02	1,04E-02	0,781
6,875	1,14E-02	1,12E-02	0,804
6,205	1,22E-02	1,19E-02	0,823
5,631	1,29E-02	1,27E-02	0,839
5,134	1,36E-02	1,34E-02	0,853
4,702	1,43E-02	1,42E-02	0,866
4,323	1,51E-02	1,49E-02	0,876
3,990	1,58E-02	1,56E-02	0,886
3,695	1,65E-02	1,64E-02	0,894

Table 3.2. Proposed Abaqus input parameters of B35 concrete (Cont.)

3,433	1,72E-02	1,71E-02	0,902
TENSION			
Stress, σ_t (N/mm ²)	Strain, ε_t (mm/mm)	Cracking strain, $\tilde{\varepsilon}_t^{ck}$ (mm/mm)	Damage parameter, d_t
3,500	1,30E-04	0,00E+00	0,000
1,569	3,33E-04	2,75E-04	0,552
1,046	5,37E-04	4,98E-04	0,701
0,796	7,41E-04	7,11E-04	0,773
0,647	9,45E-04	9,21E-04	0,815
0,548	1,15E-03	1,13E-03	0,843
0,477	1,35E-03	1,33E-03	0,864
0,424	1,56E-03	1,54E-03	0,879
0,382	1,76E-03	1,75E-03	0,891
0,348	1,96E-03	1,95E-03	0,901
0,320	2,17E-03	2,15E-03	0,909
0,296	2,37E-03	2,36E-03	0,915
0,276	2,57E-03	2,56E-03	0,921
0,259	2,78E-03	2,77E-03	0,926
0,244	2,98E-03	2,97E-03	0,930
0,230	3,19E-03	3,18E-03	0,934
0,219	3,39E-03	3,38E-03	0,938
0,208	3,59E-03	3,58E-03	0,941
0,198	3,80E-03	3,79E-03	0,943
0,190	4,00E-03	3,99E-03	0,946

The necessary parameters required by Abaqus play an important role in defining the CDPM as well as calibrating simulative models (Table 3.3). First of all, in case of dilation angle (ψ), according to Wu et al. (2006) a parameter chosen to provide proper the dilatancy parameter α^p with common range between 0,2 and 0,3 of for concrete corresponding between 31° and 42°. Furthermore, after applying various values of dilation angle to simulative models, Najafgholipour et al. (2017) indicates that a value of 35° of the dilation angle parameter is considered to result in a reasonable the lateral load-deformation curve and the failure mode after applying different values of dilation angle to FEA models. Besides that, Ren et al. (2015) applied a value of 35° in order to define the dilation angle while a value of 40° is chosen by Genikomsou and Polak (2015). Secondly, Ren et al. (2014) took a small value 0,1 as the flow potential

eccentricity the rate at which the hyperbolic flow potential approaches its asymptote. Genikomsou and Polak (2015) also used the same value. Thirdly, the ratio between the equivalently biaxial and the uniaxial compressive strength is about 1,16 according to Kupfer et al. (1969). The stress ratio is also recommended as 1,16 by Genikomsou and Polak (2015) and Wu et al. (2005). Afterward, Ren et al. 2014 and Genikomsou and Polak (2015) choose the ratio of the second stress invariant on the tensile meridian, $q(TM)$, to that on the compressive meridian K_c was taken as $2/3$ similar to the stipulation of Dassault Systèmes (2013). Moreover, after examining the load–displacement response of the slab-column connection with three values of K , $2/3$, 0,9 and 1, Genikomsou and Polak (2015) concluded that there is no significant deviation among three results and the less value of K , $2/3$ causes more realistic results. Finally, Wosatko et al. (2015), a value 0,01 of viscosity parameter is considered to be the best choice and a premature divergence is witnessed in event of no viscous regularization while a value of 0,0005 is chosen by Ren et al. (2014) because it leads to results approximately close to experiments while higher viscosity coefficient would make the structure of ‘‘harder’’.

Table 3.3. Input parameters for CDPM

Dilation angle	Eccentricity	f_{bo}/f_{co}	K	Viscosity parameter
35	0,1	1,16	$2/3$	0,007985

3.2.2. Steel reinforcement

420 yield strength steel (S420) is applied to reinforcing bars while S520 steel is applied to shear connectors (Table 3.4). An elastoplastic model is applied in Abaqus (Figure 3.2).

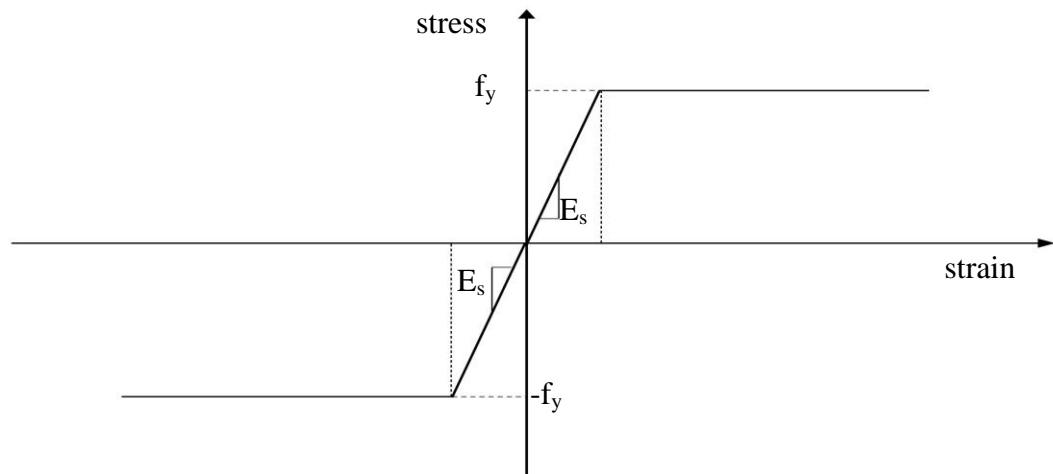


Figure 3.2. Elastoplastic model of steel

Table 3.4. Mechanical properties of steel

Property	S420 and S520
Density, T/m ³	7,85
Elastic modulus (E_s), MPa	210 000
Poisson's ratio (ν)	0,3

3.3. The Concrete-to-concrete Interface

Coulombic friction model is chosen to define the left as-cast concrete-to-concrete interface in the present thesis. It is noted that in order to figure out the performance point of structures, under applied large lateral pushing, materials fall into the inelastic regime and large slippages between core-to-cover concrete substrates are predicted.

3.3.1. The left as –cast interface

Coulomb friction model consists of tangential and normal behavior at the interface.

3.3.1.1. Tangential behavior

Firstly, in the planar behavior, a constant of friction coefficient is applied due to the fact that an isotropic friction behavior is assumed on concrete-to-concrete substrates. The

parameter playing crucial role in evaluating the quality of the interface not only recommended by researchers but also stipulated in current codes (Table 3.5). In the present study, a constant friction coefficient of 0,6 applied to smooth surface according to ACI 318-08 (2008) indicating that concrete placed against hardened concrete not intentionally roughened $0,6\lambda$ where $\lambda = 1,0$ for normal weight concrete. A value of 0,6 is also applied to a free surface left without further treatment after vibration by as EN 1992-1-1 (2004).

Table 3.5. Friction coefficient of concrete-to-concrete interface

Sources	Friction coefficient, μ
Birkeland and Birkeland (1966)	0,8-1,0
Mattock and Hawkins (1972)	0,8
CEB-FIP Model (2010)	0,5-0,7
EN 1992-1-1 (2004)	0,6
ACI 318-08 (2008)	0,6

Secondly, a critical shear stress is calculated theoretically following Von Mises stress is applied to the friction model. Assumedly saying that, at the interface surfaces of elements mostly behaving under flexural conditions as the case in the thesis, the normal stress is not large enough to initiate the situation in which the materials at the interconnection yield and the surfaces slide on each other regardless the intense of normal stress. However, the critical shear stress must be filled out in the Coulomb friction model as required by Abaqus.

Thirdly, sliding at the interface is divided into two states, elastic and inelastic. In the elastic range of slippage, the stiffness of concrete-to-concrete joint is chosen equally to the Young elastic modulus of concrete material in shear, G .

Finally, according to Dassault Systèmes (2013), the method of altering the default elastic slip is convenient if the goal is to increase computational efficiency, in which case a value larger than the default of 0,005 would be given, or if the goal is to increase

accuracy, in which case a value smaller than the default would be given. The defaulted value is chosen in the present thesis.

The crucial parameters defining Coulomb friction model is required (Table 3.6). The value of shear-transfer stress at the inter-concrete substrates is calculated based on Von Mises stress.

Table 3.6. Parameters of the modified Coulombic friction model

Friction coefficient	0,6
Shear stress limit (τ_{\max}), MPa	9,093
Elastic stiffness (κ or G), GPa	11,435
Fraction of characteristic surface dimension (F_f)	0,005

3.3.1.2. Normal behavior

“Hard contact” and zero-penetration are applied in the normal direction. Surface separation is accepted in event of no contact is captured. Besides that, when “hard contact” is applied, tension is not withstand at the interface surface.

3.3.2. Formulation of friction model in Abaqus

Coulomb friction model is chosen to define frictional property at the interface surface. First of all, “Penalty friction” formulation is chosen because the elastic slip is able to be applied. Secondly, “surface-to-surface contact” is chosen to describe the interaction because surface-to-surface discretization provides more accurate stress and pressure results than node-to-surface discretization if the surface geometry is reasonably well represented by the contact surfaces according to Dassault Systèmes (2013). Contact pairs are defined separately as master and slave surfaces where master surface belongs to the stiffer bodies. “Contact” type is chosen in “Interaction Properties” menu to define the cover-to-core concrete interface. “Contact properties” include tangential and normal behavior. A constant of friction coefficient is applied “isotropic friction” model in planar behavior while “hard contact” is applied to the normal direction.

3.4. Natural Dynamic Characteristics of Structures

3.4.1. Shaker test

The experiment was held at the faculty of Civil Engineering at Uludağ University. Materials as well as necessary equipment were gathered at a construction site.

3.4.1.1. Materials

A 28 day-compressive strength (cylinder) of 35MPa concrete was used for two specimens while 8mm diameter S420 grade (420 MPa yield strength) steel was chosen for both longitudinal bars and stirrups. Wooden plate formworks were used to form RC formworks and the monolithic frame.

3.4.1.2. Specimen preparation

All of RC specimens in the present study are addressed by the methodology-cast-in-place. First of all, 30mm thickness RC formworks whose dimensions had been calculated carefully to make the same finished shape as the classical frame (Figures 3.3). It is noted that, the surface of wooden formworks is smooth in order to aim the smooth interface between concrete substrates. 4 longitudinal bars and 75mm space between stirrups were applied to both column and beam formworks. Besides that, rectangular shaped bars were used for a 500mm cuboid feet. After formwork preparation, concrete was poured inside wooden formworks in-situ to form RC formworks. After pouring, concrete curing method was applied to keeping new-age concrete against external factors affecting the quality of concrete until concrete reaches its strength at the 28th day age.

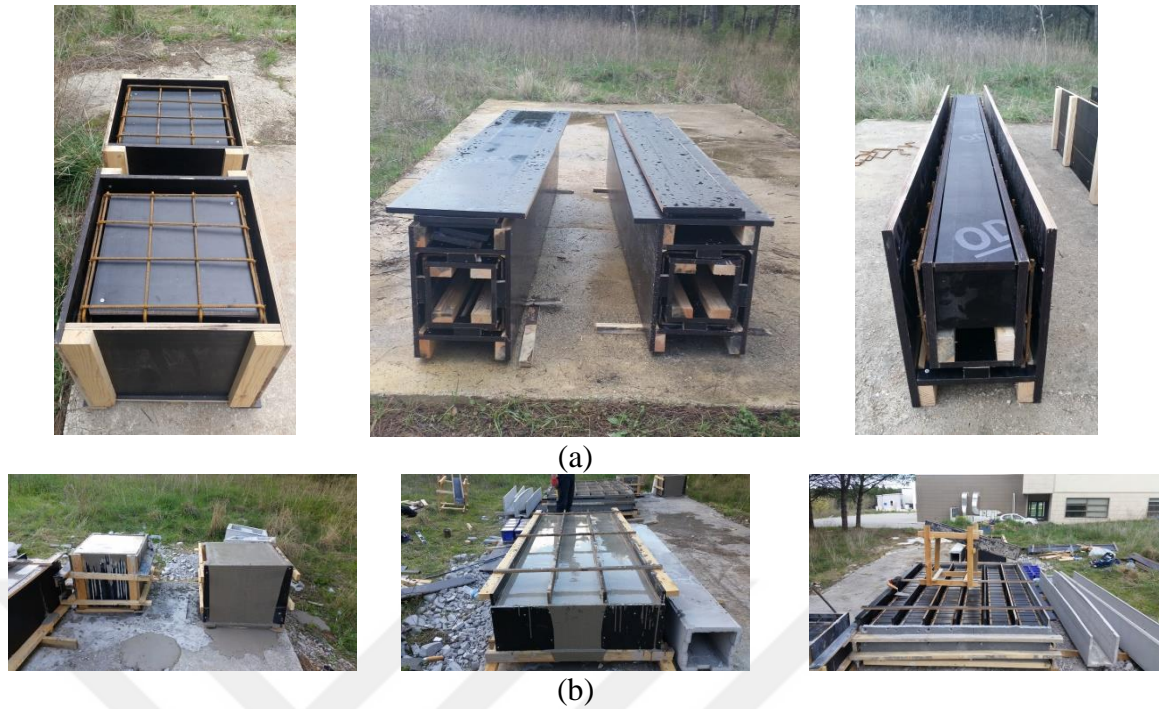


Figure 3.3. RC formworks for bases, columns, and beams. (a) Preparation (b) Products.

Wooden formworks were installed for CF specimen while RC formworks were to form NF (Figure 3.4). The construction process of the structure using RC formworks was similar to the traditional method in general. After formwork installation, concrete was poured to form lower parts such as 4 feet and tie beams. It is noted that the reinforcement of columns was adapted before pouring concrete inside the lower parts.

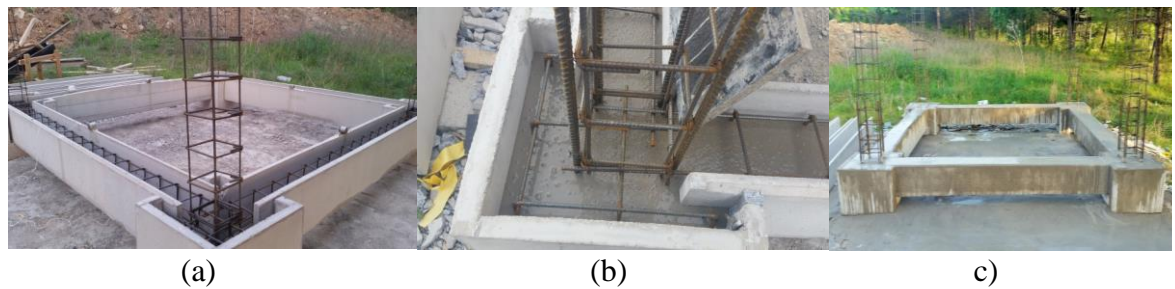


Figure 3.4. Pouring concrete into the RC formworks. (a) Formwork installation (b) Pouring concrete c) Product.

After pouring lower components, RC formworks for columns were installed then and finally, upper parts of structures were fit up (Figure 3.5).



Figure 3.5. Formwork installation of columns and beams.

Pouring concrete for CF and NF was done at a same time. Observe the finished specimens the most remarkable difference after pouring concrete is that the workspace of both frames is so different from the other's one (Figure 3.6). Everything looks like finished for the structure that used the integrated formwork system and the environment around it was cleaner than the site around CF. Curing condition was considered strictly until the new concrete reached the desirable strength.



Figure 3.6. The working space of two frames when waiting for the age of concrete.

3.4.1.3. Shaker setup

The Shaker test was installed to both of structures to examine the dynamic characteristics of both structures. The test was done in two perpendicular horizontal

directions (x and z) of each structure. Besides that, for accuracy reasons, there were two sources of digital information collected in every direction by mounting shaker at two positions, particularly at the top of two columns (Figure 3.7). It is interestingly noting that, the position of shaker is at one corner of the spatial frames in order to extract the desired mode shapes of structures that are easily to be predicted.



Figure 3.7. The working space of two frames when waiting for the age of concrete.

At the beginning of the test, some forms of vibrating force such as sine, random, impulse and pink were applied respectively. The forces that applied to the structures were controlled by SignalCalc Dynamic Signal Analyzer software and their information was stored to the computer's hard disk. In the next step, electronic data is collected from three accelerometers that were attached to the top of the three other columns. The accelerometers must be parallel to the considered axis and mounted carefully at the top of columns to avoid inexact signal. A DSA system collected and computed the electronic signal completely and saved them to the computer.

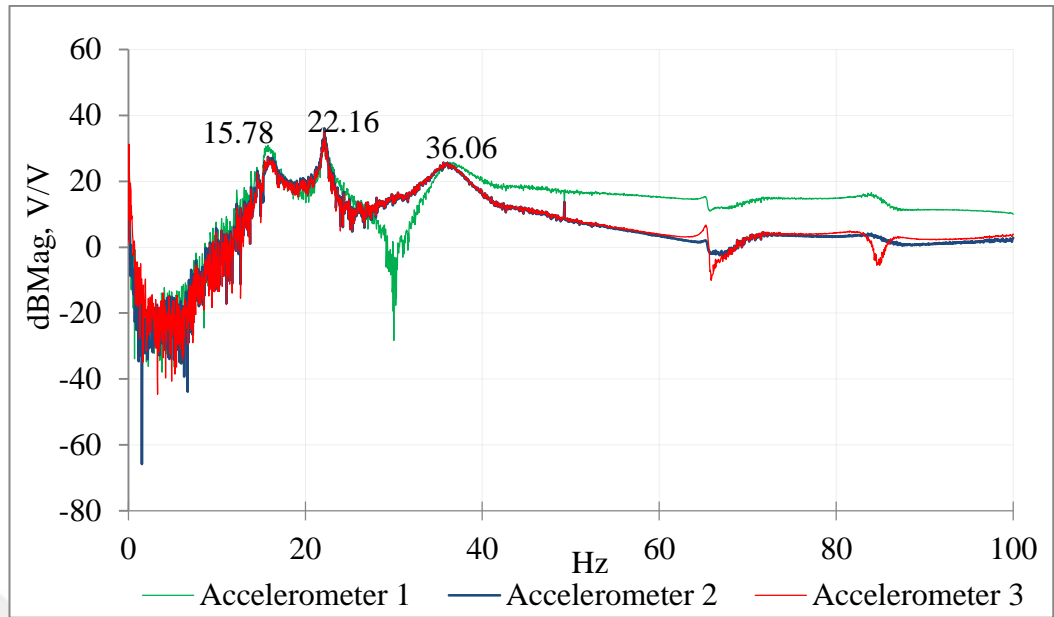
4. RESULTS AND DISCUSSION

4.1. Shaker Test

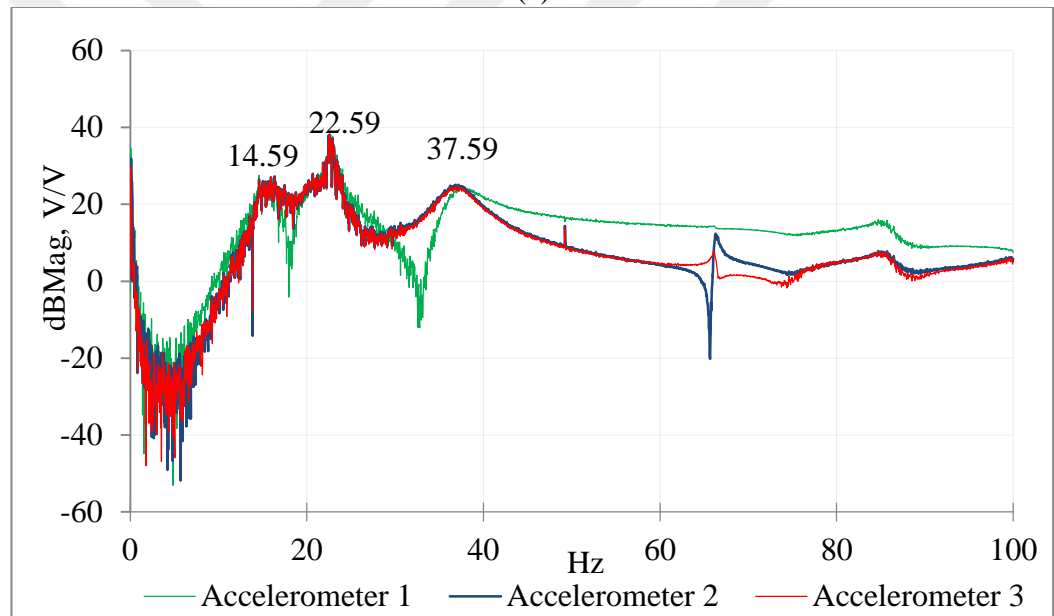
The electronic signal collected in terms of the magnitude of displacement, velocity or acceleration from three accelerometers is analyzed using SDSA software throughout external excitations. In SDSA software, Fast Fourier Transfer function (FFT) is applied to digitize the input data. Besides that, although both of two frames are symmetric, the experiment is observed carefully in two perpendicular directions namely x and z in order to control the results effectively so that there are two results for each direction corresponding to x and y directions. It is worth reminding here that in one direction, there are two output data corresponding to two positions of shaker but the deviation is not meaningful so that there is one output data shown in one direction for simplicity purpose.

Each colorful line representing digitalized results based on the response of the point stick to an accelerometer is displayed in a Cartesian coordinates consisting of the value of magnitudes shown in vertical axis and natural frequency values on horizontal axis. The overlay of the three colorful lines on the Cartesian coordinates is called the frequency response functions (FRFs) of structures.

There is no doubt saying that there are three meaningful values of frequency able to be derived based on the clearly seen by eyes three peaks that in each FRFs (Figure 4.1 and Figure 4.2). Then the exact values of natural frequencies are extracted based on the values of horizontal component of coincided peaks. Base of the FRFs, after the third peaks, no natural frequency is able to be extracted because no convergence is witnessed from the three lines as a consequence of the fact the latter external vibrating forces caused by the shaker are not able to excite the different natural frequencies of the structures. It strongly suggests that the results taken from shaker test are reliable due to the approximately identical output data from both of directions, x and z.

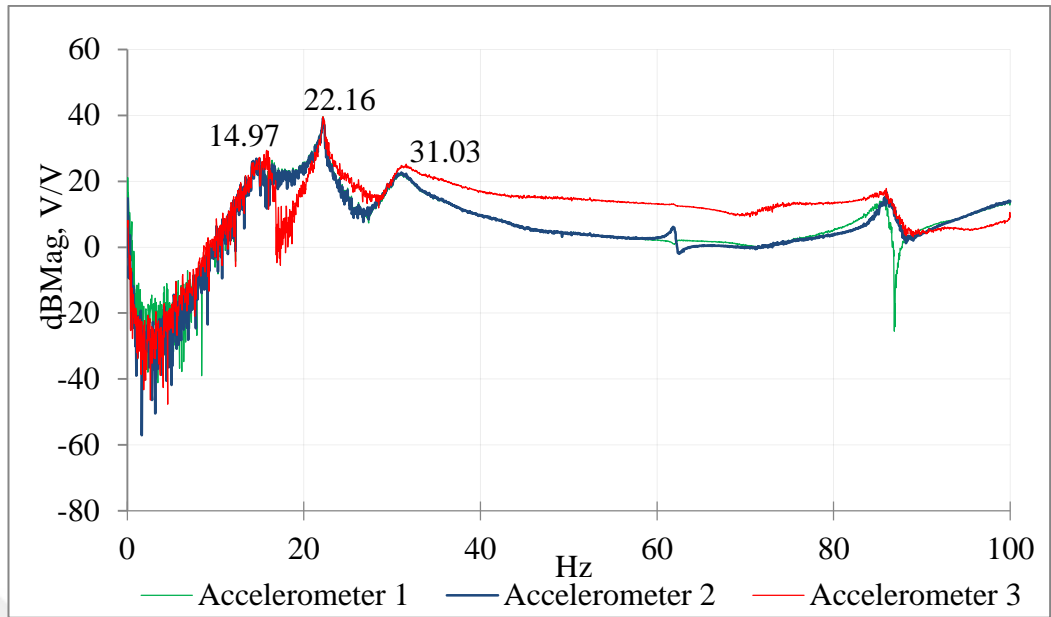


(a)

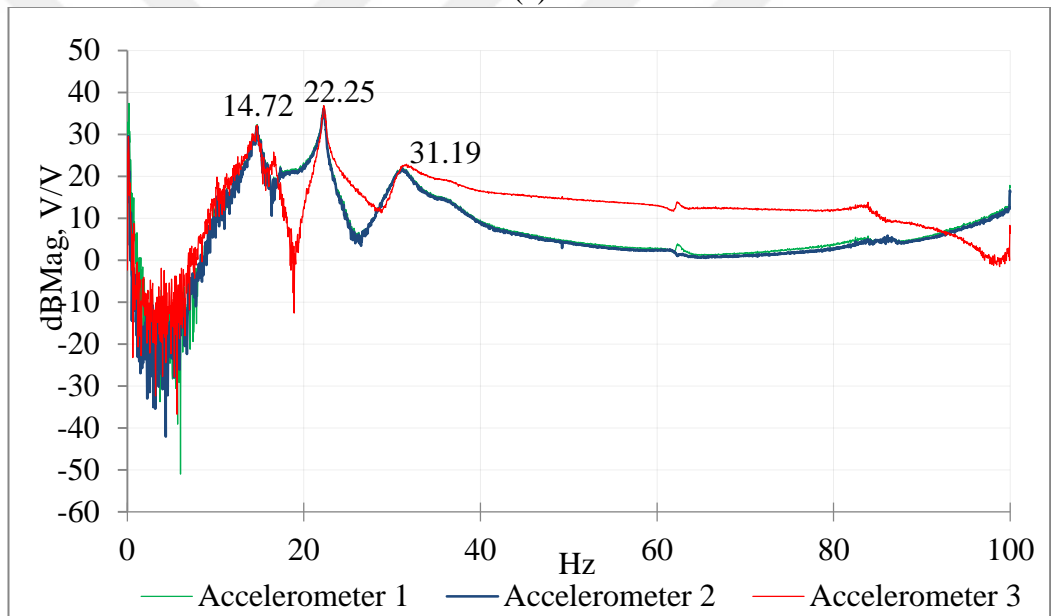


(b)

Figure 4.1. The frequency response function of Classical Frame respect to (a) x direction (b) z direction



(a)



(b)

Figure 4.2. The frequency response function of New Frame respect to (a) x direction; (b) z direction.

4.2. Modal Analysis-FEM

In Abaqus, two simulative models are built according to the realistic ones in terms of materials as well as dimensions. As applying shaker test, the main objective of modelling is figuring out the deviation between CF and NF. However, it is noted that, the simulative models defines perfectly materials models for concrete and steel while in

practice, there are many reasons affecting the strength of specimen even under strict curing condition. Consequently, the simulative results maybe deviate from empirical ones but it is not the major target.

4.2.1. Assembly

Based on the realistic dimensions, two frames CF and NF are modelled in Abaqus environment (Figure 4.3). First of all, 30mm thickness formworks prepared for beams and columns are modelled and localized to accurate positions. Besides that, the positions of longitudinal reinforcement, stirrups are localized accurately (Figure 4.4).

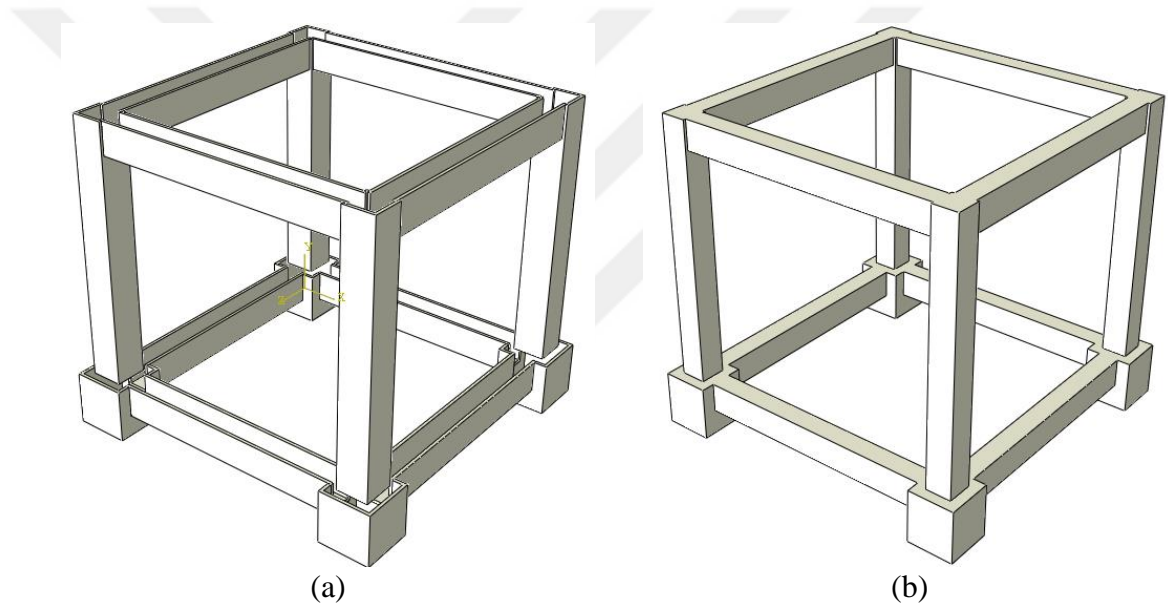


Figure 4.3. Components of NF. (a) Finished position of formworks; (b) Core part.

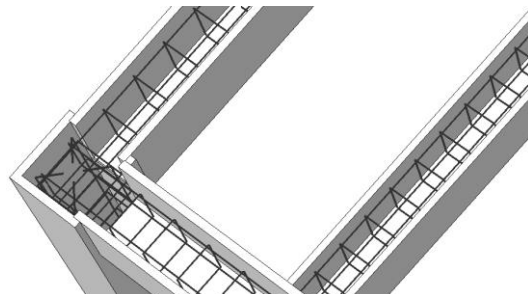


Figure 4.4. Localization of reinforced steel in NF.

4.2.2. Step selection

In Abaqus, the procedure type namely “linear perturbation” is chosen to extract the natural frequencies of structures.

4.2.3. Meshing

3D eight-node solid C3D8 elements are applied to concrete while reinforcement is defined as T3D2 elements. 50mmx50mm size meshing is applied to solid elements and 50mm is defined for truss elements.

4.2.4. Results of model analysis

The first three natural frequencies as well as corresponding mode shapes obtained by modal analysis using Abaqus are depicted (Figure 4.5 and Figure 4.6).

It is worth nothing that, the first and second modes of both structures working on lateral axes, x and z, have the same natural frequency due to the symmetric properties while the third mode shape rotates around y axis.

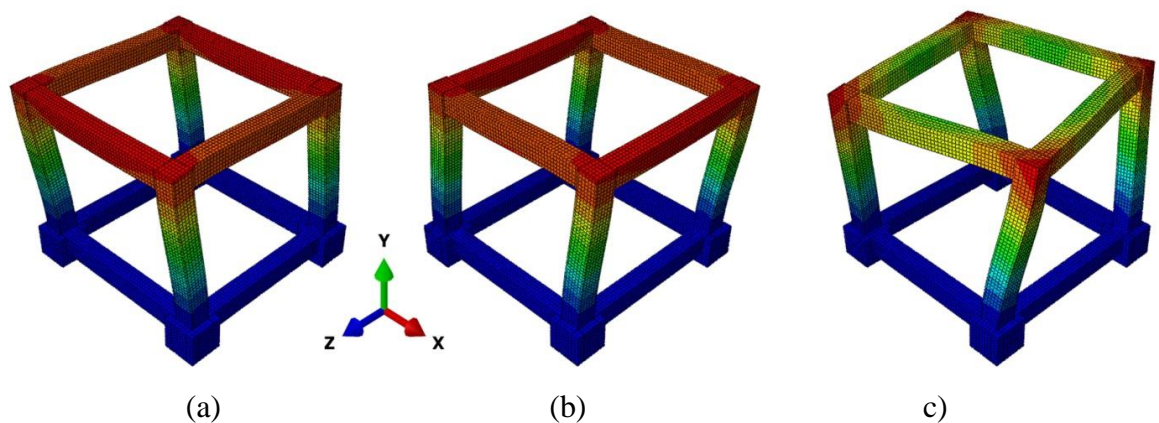


Figure 4.5. Mode Shapes for classical frame. (a) Mode 1: 19,88 Hz (b) Mode 2: 19,88 Hz (c) Mode 3: 25,02 Hz

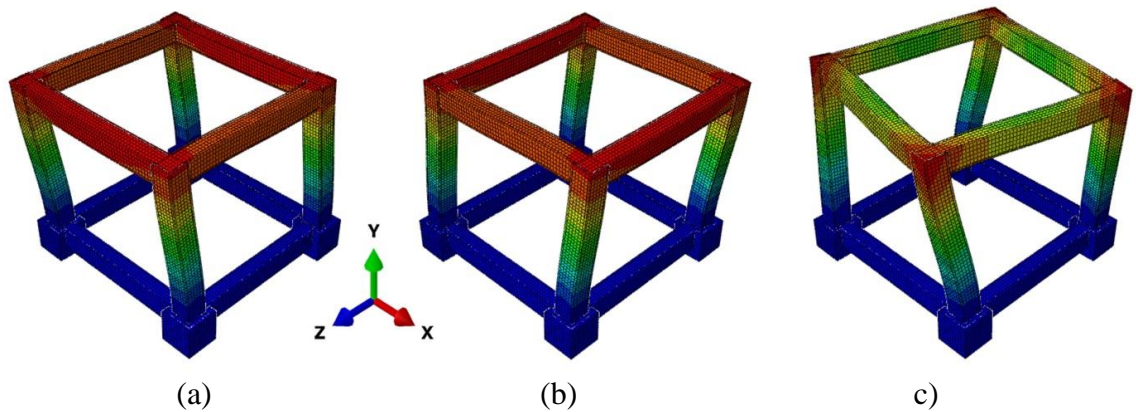


Figure 4.6. Mode Shapes for new frame. (a) Mode 1: 19,85 Hz (b) Mode 2: 19,85 Hz c) Mode 3: 24,95 Hz

4.3. Discussion of Natural Properties

According to experimental and simulative results, the predominant frequencies corresponding to Mode 1 is compared together (Table 4.1). It is worth noting that, the first frequencies obtained from FRFs correspond to Mode 1 or Mode 2 taken from Abaqus. Based on the effective mass (EM) extracted by modal analysis, Table 4.1 only focuses on the predominant frequency of each structures. Particularly, Mode 1 and Mode 2 with more than 95% of EM as well as the first frequencies determined by Shaker test are observed herein.

Table 4.1. A comparison of dynamic characteristics

Direction	Mode	Modal Analysis				Experiment		Different rate, %			
		CF		NF		CF	NF	B vs A	D vs C	C vs A	D vs B
		A		B		C	D				
		f, Hz	EM, %	f, Hz	EM, %	f, Hz	f, Hz				
x	1	19,88	95,99	19,95	95,91	15,78	14,97	0,3	-5,1	-20,6	-25,0
z	2	19,88	95,99	19,95	95,91	14,59	14,72	0,3	0,9	-26,6	-26,2

Table 4.1 statistically illustrates a comparison of natural dynamic characteristics between CF and NF based on simulative and empirical results as well as the deviation of modeling and experimental results. In both experimental and simulative results, there

is no meaningful deviation between CF and NF. However, natural frequencies obtained by experimental tests are always lower than those derived from simulation.

Natural dynamic characteristics of NF and CF are considered to be approximately similar to each other with a deviation of 0,3% in both mode shapes in the simulative environment and different rates of 5,1% and 0,9% in case of experimental tests for Mode 1 and Mode 2 respectively. It can be concluded that the structure built using RC formworks results in similar natural frequencies and mode shapes to those of the monolithic one. First of all, it can be explained that the modal analysis applied in FEA only considers elastic behavior of materials as well as the interaction between layers. Secondly, in the empirical experiment, external shaking forces are considered to be low and not enough to cause large deformation. In other words, the structure covered by RC jackets is considered to work similarly to the monolithic one. However, the natural frequencies of NF are slightly higher than those of CF based on simulation. Work under the elastic regime, the interface between substrates is considered to not effect on the behavior of elements, columns and beams, as well as the whole structure, NF works monotonically. Moreover, higher ratio of reinforcement in components results in higher stiffness of NF compared to CF. A converse trend is witnessed in case of the experimental test as a probably consequence of the inaccuracy of workmanship when building CF.

The simulative frequencies are remarkably higher than the empirical results with divergent rates of more than 20% in general. In case of the predominant frequency, correspondingly Mode 1, a dissimilar rate of 20,6% and 25% for CF and NF respectively. The deviations could be caused by the input parameters used to define materials in numerical analysis causing the frames not comparable completely to the realistic specimens as expected. Particularly, the quality of materials used in sites, and unsatisfied curing condition especially for RC formworks etc. are possibly the reasons. Moreover, the inaccuracy caused by workmanship possibly leads to the different dimensions of the realistic specimens and simulative models. Furthermore, the weight of shaker attached to systems is significant smaller than the considered system but still

effect on the results. Finally, under practical conditions, the structures work with the contribution of damping while modal analysis ignores this factor.

4.4. Base Shear-Displacement Curve – FEM

4.4.1. Left as-cast concrete-to-concrete interface

4.4.1.1. Step selection

In the present dissertation, “general static” step is chosen for pushover analysis. The analysis procedure consists of two steps. Step 1 is used to define the constant normal loading while step 2 is used for monotonic pushing displacement procedure. It is noted that, step 1 works separately from step 2 in order to account for the effect of normal loading on columns. After that, step 1 is propagated to step 2, it means that step 2 initiates based on the results caused by normal loading in Step 1.

4.4.1.2. Loads and boundary conditions

Simulative models CF and NF are subjected pushover analysis. The 4 feet are constrained spatially, normal loading is applied on top of four columns while laterally pushing displacement is applied on two columns (Figure 4.7).

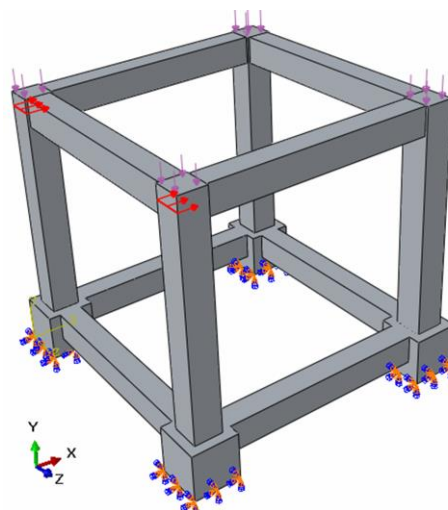


Figure 4.7. Pushover analysis procedure.

Firstly, both simulative models, CF and NF, are applied a restraint at four feet using “encastre boundary condition”. Secondly, during pushover analysis, a value of axial load equal to 30% of the normal capacity of the structure according to Truong et al. (2017) is applied constantly at the top of the four columns. It is noted that, in the present thesis, normal load is laterally contributed on the top of columns using “pressure” type. It is worth noting that in case of NF, normal load is applied only on core part of columns due to the fact that, the cross sectional dimensions of columns are smaller than in. consequently, the value of normal pressure of two frames is different from each other. Thirdly, a displacement-based load pattern is determined based on the predominant mode shape of structures obtained by modal analysis done in the above chapter. It is noted that, the predominant period of structures obtained numerically by Abaqus is considered in this chapter. Particularly, based on Mode 1, pushover analysis is established for CF and NF. There are two ways to apply pushover analysis, displacement and load controlling procedure. The first one is chosen because of the models are so complicated to predetermine lateral loading pattern. A monotonic pushing displacement procedure is applied symmetrically at the top of two columns of CF and NF. The lateral displacement is applied incrementally until the drift ratio is equal to 3,5% as stipulated by ACI Committee 374-05 (2005). In the present thesis, in order to compare the deviation between CF and NF, a same mass and same lateral displacement are applied to both structures (Table 4.2). It is noted that the normal load is applied to the core part of NF whose columns have smaller sectional areas. Consequently, the normal pressure applied to NF is bigger than the case of CF.

Table 4.2. The parameters of pushover analysis.

Component	CF	NF
Normal pressure, N/mm ²	5,97	9,33
Target lateral displacement, mm	87,75	87,75

When bonding between reinforcement and concrete is concerned, embedded constraint in which the reinforcement is considered to be embedded the host parts, particularly concrete elements. In order words, reinforced bars are bounded by and completely obey the translations and rotations of the host parts. It means that there is no occurrence of

de-bonding between concrete and steel bar, however the bonding mechanism can be seen as the damage of concrete interactively surrounding bars.

4.4.1.3. Meshing

It is noting that meshing plays an important role in computational cost. However, the mesh size dependency does not considerably affect the overall response of the structures in FEA and it is 40 mm mesh size causes the closest result to experiments due to the fact that most damage processes, causing concrete cracking propagation usually involve length scales in the order of two to three dominant aggregate sizes of the base concrete material according to Najafgholipour et al. (2017). Besides that, Abbas et al. (2014) modelled concrete with a dense mesh of 8-node brick finite elements with 50 mm size meshing. Invariant 40mm size meshing assumed as the optimum choice based on previous tests re applied to both concrete and reinforcement according to Najafgholipour et al. (2017). In the present study, the mesh size is chosen automatically by Abaqus with the maximum size as 50mm for 8-node brick in case of concrete and 50 mm length in case of reinforcement defined as truss elements. However, in some special cases, the maximum mesh size is changed in order to be suitable to the specific situation, especially when meshing RC formworks applied complicatedly geometrical irregularities. Ren et al. (2014) used element sizes of 25,4 mm x 38,1 mm x 12,7 mm in FEA. In the present thesis, 3D eight-node solid (C3D8) elements are applied to concrete while reinforcement is defined as truss elements (T3D2). Besides that, all of elements are meshed using 50mm size.

4.4.1.4. Results

Roof-displacement versus base shear force graph of the frame built using RC formworks and the traditionally constructed frame obtained using monotonically lateral pushing are plotted (Figure 4.8).

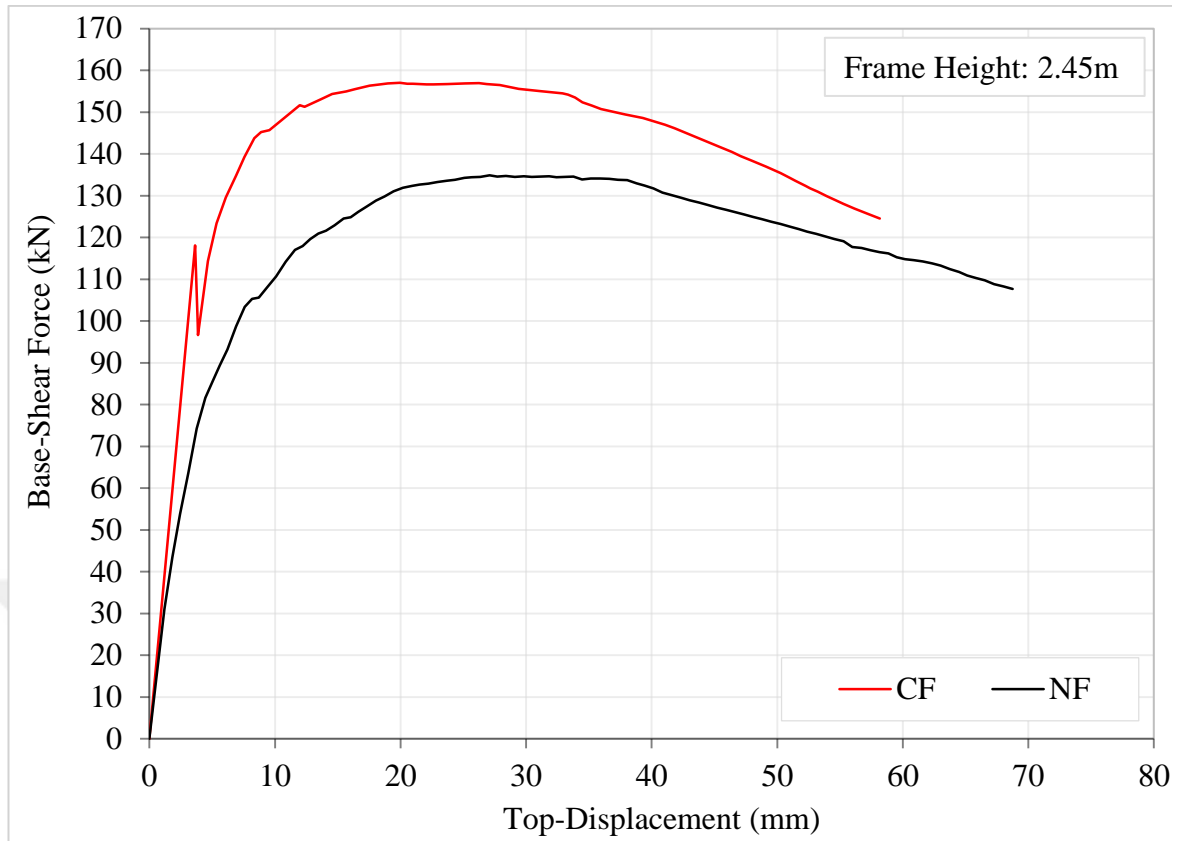


Figure 4.8. Flexural behavior of CF and NF

The line graph sheds light on a comparison of the flexural performance of a single story spatial RC frame formed using RC formworks prefabricated to a reference monolithic frame. One of the more prominent takeaways of the line graph is that although two structures surveyed through a same pushover analysis procedure demonstrate a similar trend of base shear versus top displacement curves, the structure covered by RC formworks is not only weaker but also less ductile than the monolithic one.

The product of pushover analysis initiates by a linearly increasing trend at elastic stage followed by another increasing regime but with continuously reduced stiffness until hitting peaks starting a declined curve ending up at a base shear-force of 80% of the peak value. The elastic regime of NF, particularly, ends up at 7,26mm when reaching a base shear-force of 101,14kN compared with the value of 117,73kN transpiring at 4,92mm for CF. In other words, the bending elastic stiffness of NF is about 58,27% of

CF. A similar situation takes place in the inelastic regimes, where NF hits a peak of 134,85kN reduced by an amount of 14,1% from the ultimate value of CF and the peak is captured at 27,08mm later than the latter peak about 7,13mm before tailing off and completely collapsed at 68,48mm while CF ruptures at 57,29mm. Similarly to the lower bending capacity, NF is considered as a less ductile structure by performing a ductility factor of 9,44 compared with 11,64 in case of CF even the destination of the monolithic structure is reached sooner than. Designed a same sectional dimension as the monolithic structure and owning a higher value of longitudinal reinforcement, the nonlinear performance of NF is degraded remarkably compared with the monolithic one as a consequence of the fact that the occurrence of slippage at the inter-concrete surfaces between the core and cover parts causes a lower bending stiffness of NF when forced to experience lateral displacements. Even working under an assumed elastic condition, the cover concrete parts separate immediately from the base surfaces because there is no tensile strength is defined at the interface while the peripheral concrete elements of CF at the tensile sides of columns and beams contribute to the strength of the whole structure until the tensile strength is reached. The degradation is witnessed more profoundly when the structures fall into the nonlinear stage. It can be seen that although the main reinforcing bars at tensile and compressive sides of structural elements as well as concrete parts of RC formworks contribute to the strength of NF throughout the process of forming plastic hinges, the contribution is limited because sliding at the interface leads to the absence of the shear transferability of the interconnection, especially when the maximum value of shear stress is exceeded.

4.4.2. Application of surface treatment methods

Aim at monolithic behavior the shear strength at interconnection is enhanced using steel shear-links, shaping geometric irregularities, and a combination of them. For the purpose of simplicity, an increasingly adjusted friction coefficient is accounted for corresponding to each surface treatment method.

Besides that, in case of pure concrete-to-concrete interface surfaces, Vandoros and Dritsos, (2008) concludes that jacketing without surface roughening method leads to significant stiffness degradation, the separation of jackets, premature failure, and a

lower ductility because of a poor bond at the interface surface. For the purpose of simplicity, Lampropoulos and Dritsos, (2011) concludes that the bending capacity of RC jacketed columns is equal to 80% of the strength of a respective monolithic specimen. Moreover, the strength is reduced to 70% according to Thermou et al. (2007).

In the present thesis, there are two surface treatment methods that are applied in order to enhance the shearing strength at the interface as well as the bending capacity of the structure built using RC formworks.

4.4.2.1. Steel Connectors

Based on an experimental test on jacketed columns, Vadoros and Dritsos (2008) indicated that the capacity of strengthened specimens applied about 0,29% ratio of 20 mm diameter grade S500 L-shaped dowels of dimensions 150 mm by 100 mm is about 9,1% and 14,9% less than a monolithic one at yield and ultimate point respectively. Moreover, Mazizah and Izni (2015) set up a “push-off” test in order to compare the shearing strength at the interconnection of specimens made by two concrete layers. According to the experimental results, the joint using approximate 0,565% ratio of shear connectors (6 mm diameter grade S250 Π -shape) performs higher shearing strength, particularly 2,8, 1,12, and 1,59 times, than the left as-cast (smooth) interface in case of 0, 0,5 and 1,5 N/mm^2 laterally distributed pressure applied on the top parts. Furthermore, in order to evaluate the effect of the shape of connectors on load-slip relation at old-new concrete layers, Wang et al., (2011) placed at interface surface three types of 6,5mm diameter shear link, I, Γ , and Π shape. Obtained load-slip curves indicate that the two latter types improve not only the shearing strength capacity but also the ductile behavior of the interconnection more effectively than I shaped shear links. In the present study, Π shaped tie connectors placed at concrete-to-concrete substrates with a variety of ratios are observed using simulative modeling a single story spatial frame formed using RC formworks in order to figure out the effect as well as the suitable ratio of shear connectors.

On the other hand, the planar property consisting of concrete-to-concrete smooth surface and shear links (Figure 4.9 and 4.10). In Figure 4.9, the length of 15mm of

connectors is placed in the core part while the 20mm part belongs to the RC formworks. The value of f_y used for design of shear friction reinforcement shall not exceed 60,000 psi, approximately equal to 414 MPa, according to ACI 318-08 (2018). 4mm diameter Π shaped steel connectors of dimensions 35x30x35mm with 520MPa yielding strength are placed at the concrete-to-concrete substrates with a variety of shear link ratios at the interaction surface. It is noted that NF_014, NF_028, NF_048 and NF_062 are named for three RC formworks covered frames corresponding to the ratio of placed shear connectors, 0,14, 0,28, 0,48, and 0,62% respectively (Table 4.3).

Table 4.3. FE models applied shear connectors

Name	Connector ratio (%)
NF_014	0,14
NF_028	0,28
NF_048	0,48
NF_062	0,62

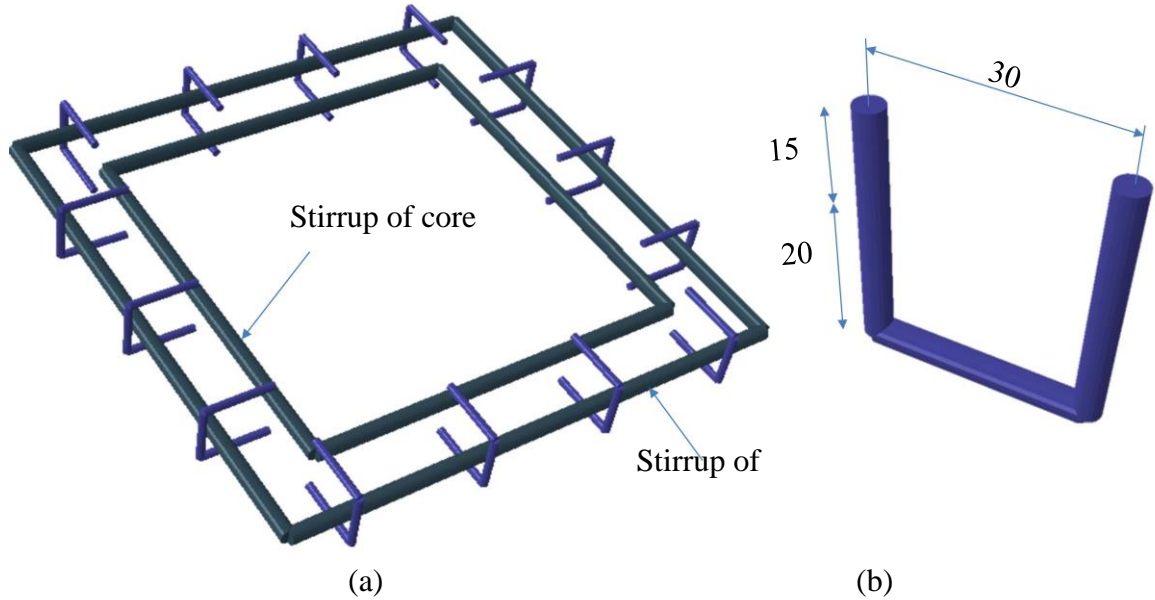


Figure 4.9. Π shaped steel connectors. (a) Predetermined location (b) Detailed dimensions in mm.

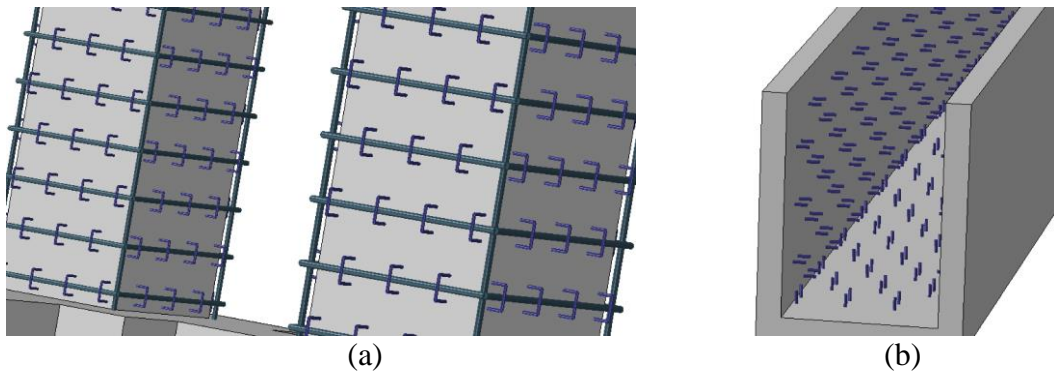


Figure 4.10. Application of Π shaped shear links. (a) on columns; and (b) on RC formwork.

Four structures whose surfaces are treated shear connectors with different ratio on surface are applied to pushover analysis and base shear versus top displacement curves are plotted (Figure 4.11) and the enhancement brought by each ratio of shear links are displayed (Figure 4.12).

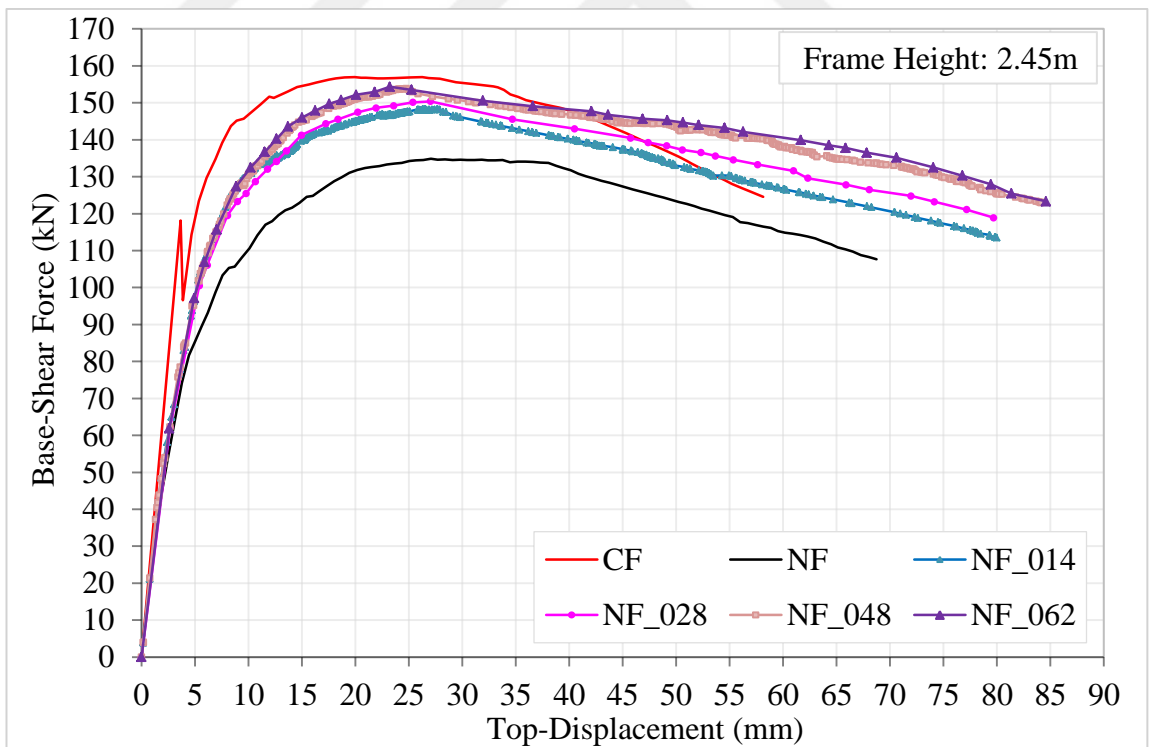


Figure 4.11. Flexural behavior of NF with connectors in compared with CF and NF.

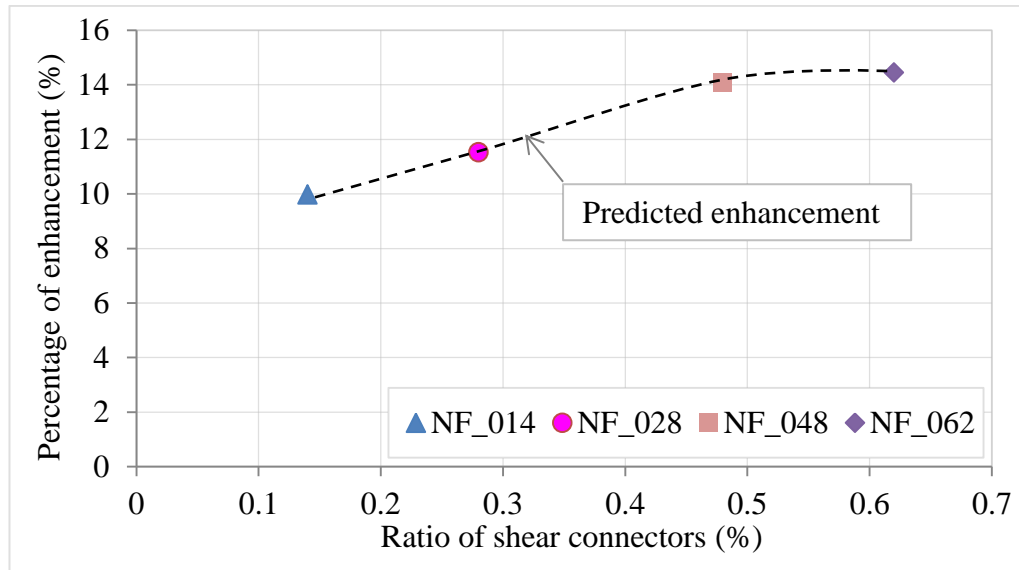


Figure 4.12. Percentage of enhancement of shear connectors

The graphs in Figure 4.11 and Figure 4.12 shed of light on a comparison of the flexural strength when falling into nonlinear regime, of a single story spatial RC frame, formed using prefabricated RC formworks without and with a variety of shear connector ratios placed at concrete-to-concrete interface to a reference monolithic frame. The surface treatment method by shear connectors plays a remarkably effective role in improving the shearing strength at the formwork-to-cover concrete layers, the bending capacity of whole structures in other words.

Initially, it is evident saying that the shear connectors play an important role in increasing the bond strength between cover and core parts and possibly upgrade a composite structure to a monolithic one in terms of bending capacity. Based on the base-shear force versus top lateral displacement curves, when the ultimate bending strength is concerned, a series of NF whose interface surfaces are treated placing shear connectors perform higher peaks than the specimen with left as-cast surfaces, up to approximate 14,44% as well as 98,315% the bending capacity of the monolithic one. The ultimate bending moment of NF_014, NF_028, NF_048, and NF_062 are calculated as 363,345kNm, 368,442kNm, 376,902kNm, and 378,118kNm respectively that is remarkably enhanced in comparison with the flexural capacity of NF, particularly 330,388kNm. It is assumedly said that bending is considered to be predominant so that

the substrates tend to slide on each other. However, the shear connectors are able to prevent the situation of slippage until yield stress in steel connectors is reached due to a mechanism called dowel action. Yield stress in connectors, in practice, can be caused by bending, axial load as well as torsion. However, in simulative modeling, shear connectors are defined as truss elements due to a simplification purpose so that they work under tension or compression only.

Due to the benefit brought by dowel action, ductility factor, known as one of the major parameters when evaluating the nonlinear performance of structures, is also for the series of NFs. The structures applied the surface treatment using shear connectors perform more ductile behavior than NF whose ductility factor is about 9,439%. Particularly, the evaluated factor is upper than 11% for NF_014 and NF_028. Those values closely approach the 11,642% ductility factor of the monolithic one that is exceeded by the ductility factor of NF_048 and NF_062 calculated as 11,883% and 12,013% respectively. Graphically saying that the fracture point is prolonged from a value of 68,482mm belonging to NF to a distance of 84,394mm of NF_062 considered remarkable compared to the modest maximum journey of CF, about 57,293mm. The situation can be explained that the higher ratio of bending carrying bars and the contribution of shear connectors are considered as the backbone of the ductile behavior of NFs. It is noted that although the bending enhancement of NF_062 is not only countably higher compared with NF048 but also the ductility is not improved basing their descending branches after reaching the peaks and the structures seems to be collapsed at a same lateral displacement, at about 123mm.

Based on aforementioned comparison there is no doubt saying that the improvement in terms of bending capacity as well as ductility factor profoundly increases in proportion to the increase the shear connector content on the concrete-to-concrete interface but an extremely high amount of shear ties seems to not to be effective as expected. Surface crossing steel shear links contribute tremendously to the overall bending capacity of the series of NF, particularly 9,975%, 11,518%, and 14,0784% when being applied from a ratio of 0,14%, 0,28% and 0,48% respectively. Meanwhile a ratio of 0,62% shear links only possibly improves 14,446% compared with the one working with left as-cast

surfaces or 0,368% in compared with NF_048 in other words. As a result, a suitable content of shear connectors placed on concrete-to-concrete surface in case of bending predominant RC structures should be recommended herein is a value not exceeding 0,48%.

4.4.2.2. Indented construction joints

Patton (1966) introduces geometrical configurations on plaster specimens (2,95 inches long, 1,75 inches wide, and 2,0 inches high) consisting of two layers. The geometrical textures, called "teeth" were shaped as rectangular with different types of inclined teeth with slopes of 25°, 35°, 45°, and 55°. All of the "teeth" had a height of 0,5 inches (about 5,08mm). Observe the results, it can be concluded that the inclination of "teeth" plays an important role in increasing the slipping shearing strength at interconnections. In the range of lower normal stress, irregularities which have inclinations of 55° improve the shearing strength more effectively than lower ones. Besides that, the enhancement of shearing strength is more profound by increasing the ratio of geometrical irregularities on surfaces.

Theoretically assume that in flexural behavior, structural elements as columns and beams, at any longitudinal layers, the normal stress is zero in event of monolithic behavior. Following that, in case of composite members, at the interface, the normal stress is assumed not large so that based on the research of Patton (1966) on plaster specimens and the stipulation of EN 1992-1-1 (2004), in the present thesis, irregularities are geometrically shaped in rectangular teeth in order take advantage of cohesion intercept situation. That means the inclination i defined by Patton (1966) is 90°. Furthermore, no sliding mechanism is expected in rectangular asperities because the asperity inclination angle is 90° according to Kwon et al. (2009). In this thesis, the detailed geometrics of teeth are designed with $h = 5$ mm and $a = 37,5$ mm (Figure 4.13). It is noted that, the inter-concrete surfaces is left as completely smooth (Figure 4.14).

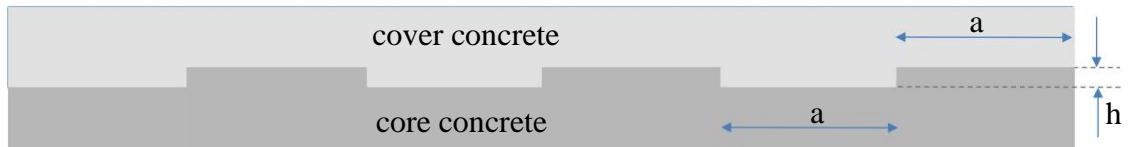


Figure 4.13. Properties of irregularities.

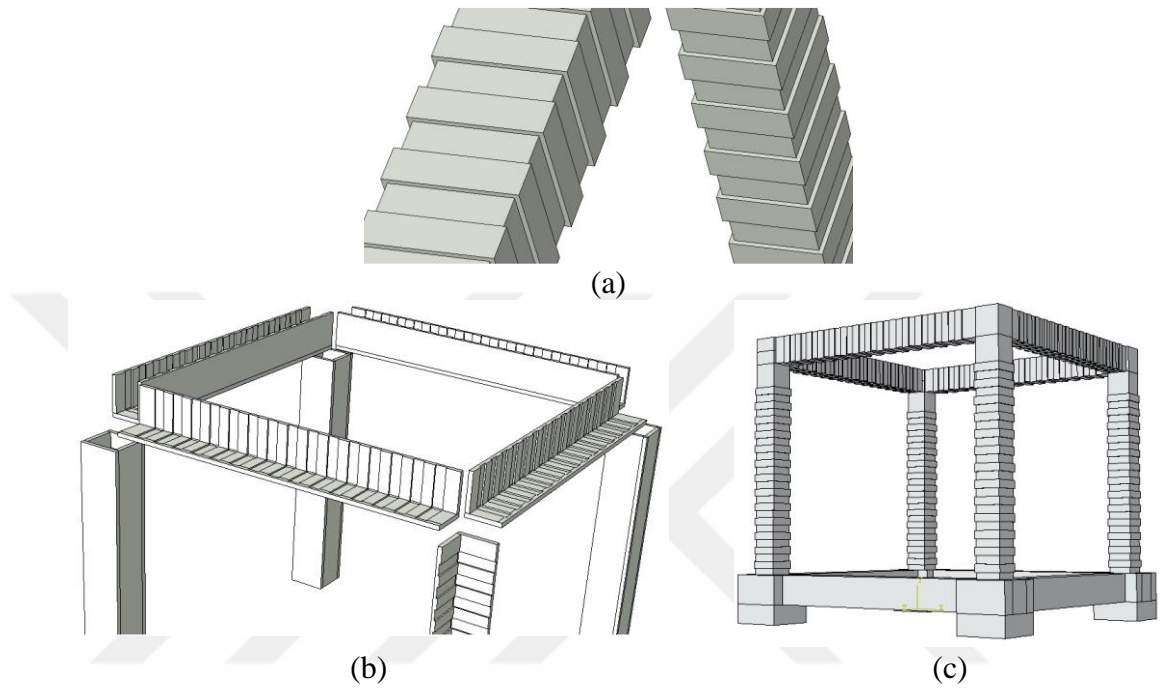


Figure 4.14. View of saw teeth. (a) On elements; (b) On formworks; and (c) On frame.

The performance of NF applied geometrical asperities at the inter-concrete surface is obtained by subjected the lateral pushing procedure is plotted in order to compare the improvement resulted by the present method with other models (Figure 4.15).

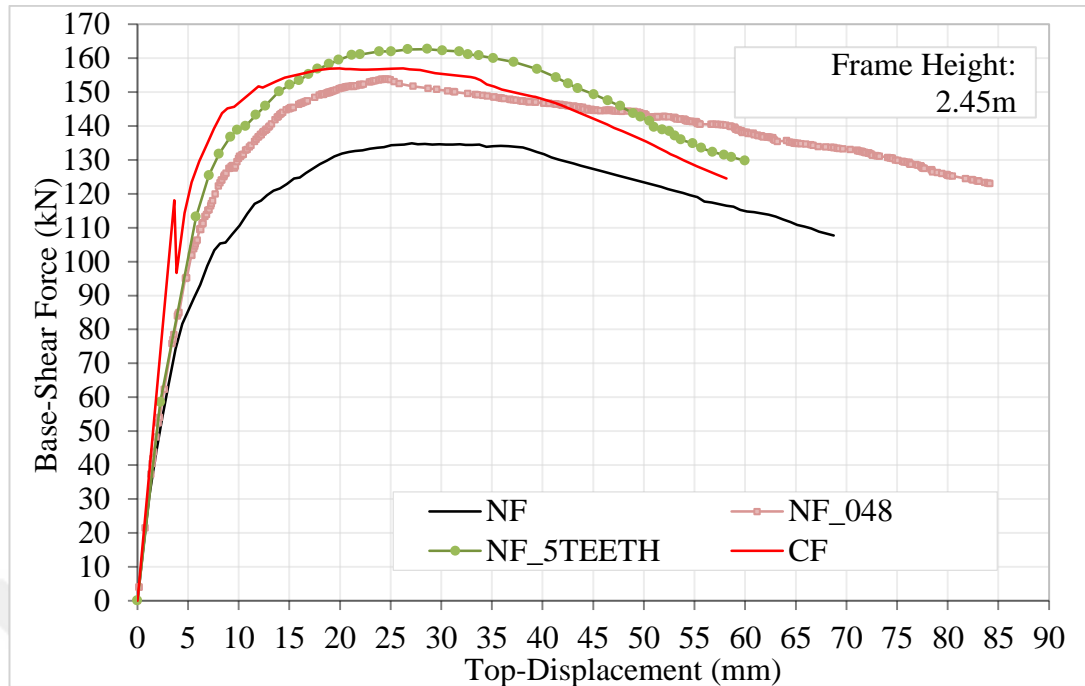


Figure 4.15. Flexural behavior of NF with connectors in compared with CF and NF.

The line graphs in Figure 4.15 highlight the flexural capacity improvement brought by applying geometrically shaped irregularities. Despite working not as a monolithic structure, the structure formed using RC formworks with the interface surfaces, treated using asperities with dimensions of 5mm height, 37,5 mm width, and 37,5mm distance, performs a tremendous flexural capacity equal to 1,206 times and 1,036 times the performance of the one with smooth surfaces and the monolithic one respectively.

The application of asperities appears as the most effective surface treatment method. The bending enhancement contributed by 5mm height asperities on the interface surfaces is about 26,06% and 5,75% compared with NF and NF_048. It indicates that rectangular shaped irregularities are able to prevent more effectively planar sliding caused by shear force at the interface than shear connectors. When slippage between concrete substrates is eliminated strictly, the structural members such as columns and beams behave monolithically. Shear stress is assumed to be transferred completely at the interface. It should be noted that the bending capacity of NF_5TEETH is also higher than the performance of the monolithic structure, CF, about 1,036 times. With a higher ratio of longitudinal reinforcement, NF_5TEETH hits a higher peak of 162,8kN at a later

lateral displacement of 28,613mm while the capacity of CF is determined as 156,98kN at 19,953mm. Notwithstanding the higher performance, NF_5TEETH performs identically to a series of NF that is considered as less stiff than CF at the elastic regime. At the first intervals of lateral pushing, the concrete parts at tensile sides contributes to the capacity of CF until the tensile strength is reached while in case of NFs, the concrete of cover separates immediately under tension.

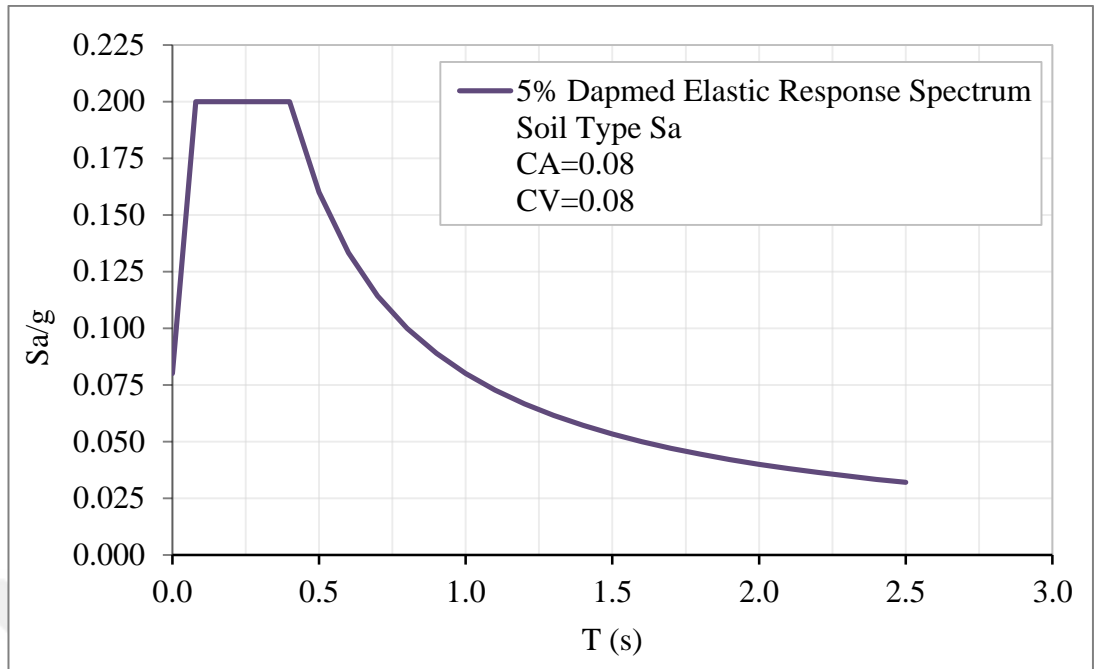
4.5. Performance Point

4.5.1. Selection a specific seismic conditions

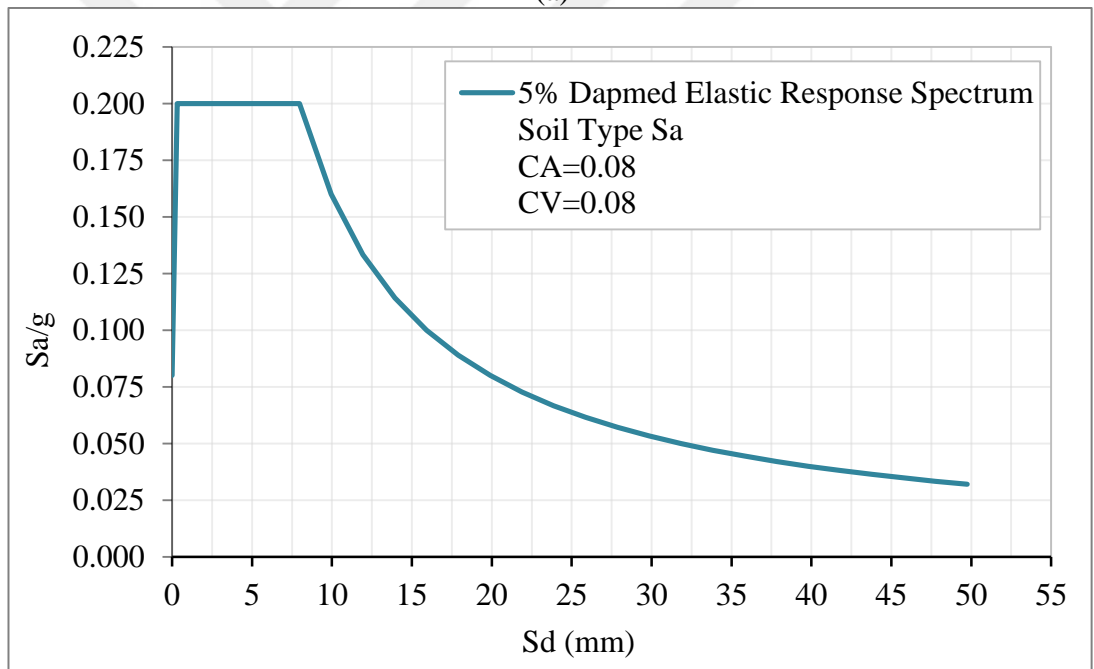
In the present thesis, a specific seismic condition is chosen in order to figure out the performance point of each model according to ACT 40 (1996) (Table 4.4). The relative parameters are taken from Chapter 1 based on the selected specific condition. The 5% damped elastic response spectrum in terms of S_a -T and S_a - S_d built based on the parameters in Table 4.4 is depicted below (Figure 4.16).

Table 4.4. Summary of seismic parameters

Specific Condition	Parameter	
Seismic Zone Factor (Z2A)	0,15	
Near Source Factor (>15km)	$N_A=1$	$N_V=1$
for the Design Earthquake	$E=1,0$	
Z^*E^*N product	0,075	
Soil Profile Type S_B	$C_A=0,08$	$C_V=0,08$
Type of structure (Type C: Average Existing Building)	$k=0,33$	



(a)



(b)

Figure 4.16. 5% Damped elastic response spectrum of Soil S_a . (a) S_a versus T ; and (b) ADRS format

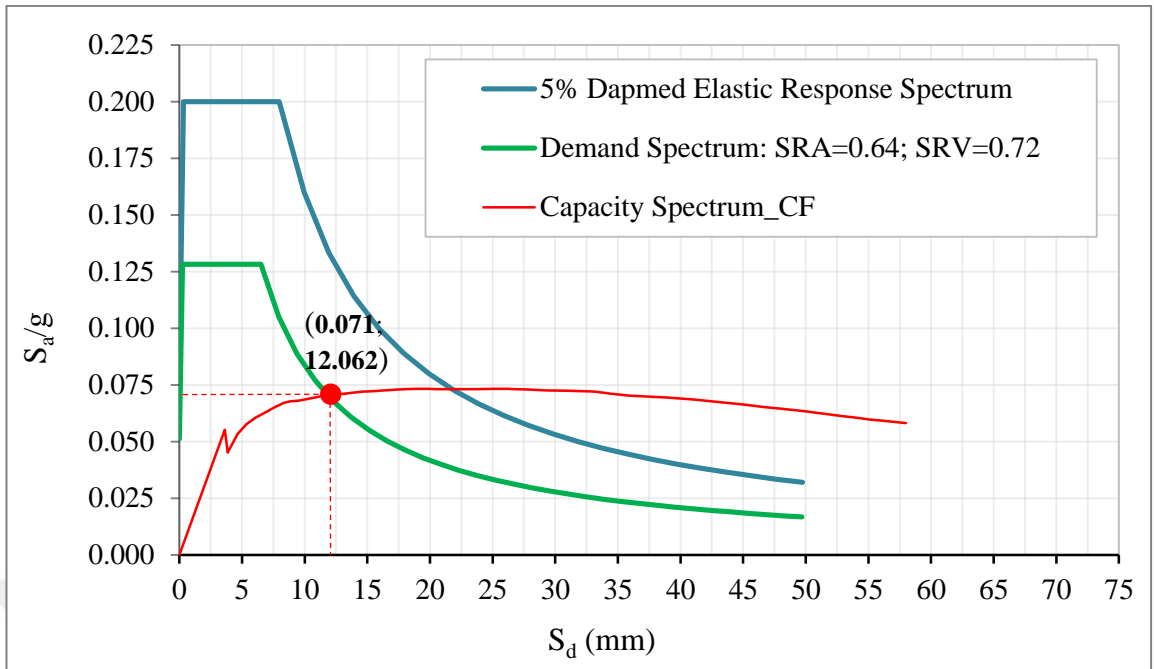
4.5.2. Determination of performance point

In order to figure out the performance point of a structure when being applied to the specific seismic conditions its dynamic characteristics is extracted again here based on

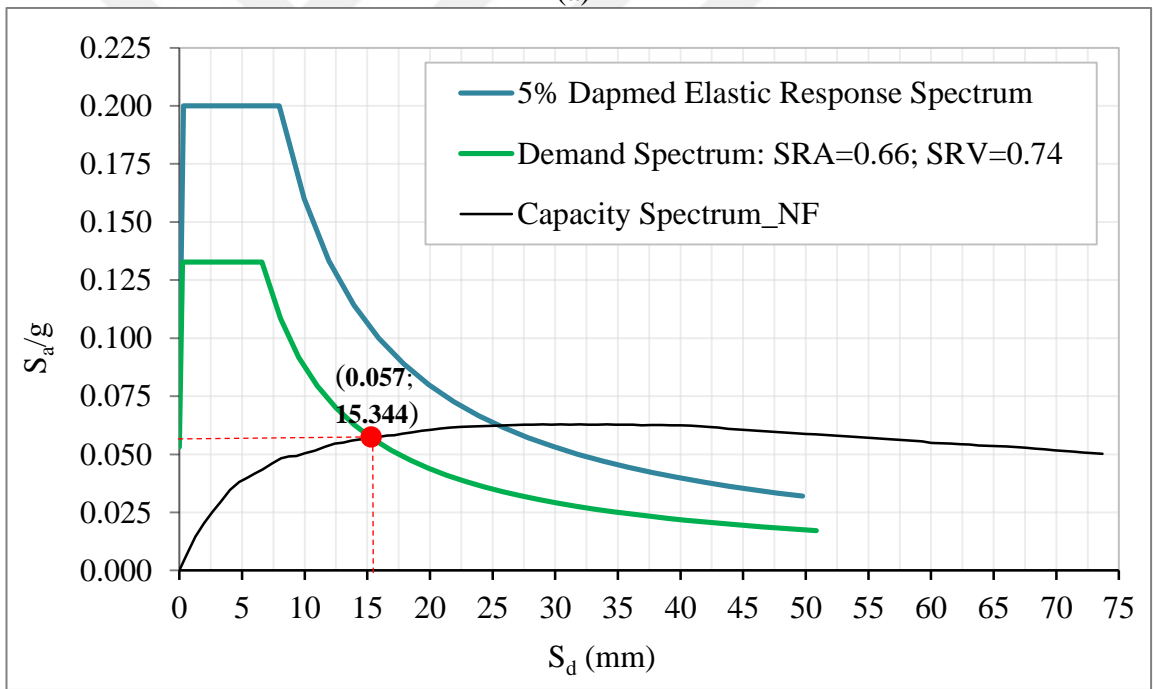
the modal analysis done using FEM. Besides that, the base shear force versus lateral displacement ($V-\Delta$) of the model is transferred into a coordinate of capacity spectrum (S_a-S_d). Afterward, the performance point of the structure subjected to the specific seismic condition can be rapidly indicated based on the procedure described in Chapter 2. The relevant parameters used to find out the performance point are listed (Table 4.5).

Table 4.5. Determination of Performance Point

Parameter	Unit	Model				
		CF	NF	NF_048	NF_5TEETH	
Fundamental Period, T	s	0,384	0,381	0,381	0,381	
Participation factor, PF		1,003	0,933	0,933	0,933	
Effective mass, α		0,999	0,930	0,930	0,930	
Gravitational acceleration, g	mm/s ²	9810	9810	9810	9810	
Total mass W	Ton	219	219	219	219	
C_A	g	0,080	0,080	0,080	0,080	
C_V	g	0,080	0,080	0,080	0,080	
a_{pi}	g	0,071	0,057	0,070	0,073	
d_{pi}	mm	12,062	15,086	13,856	13,229	
a_v	g	0,056	0,037	0,045	0,052	
d_v	g	3,679	3,179	3,410	4,279	
β_o	%	30,973	27,766	25,639	24,877	
κ		0,330	0,330	0,330	0,330	
β_{ff}	%	15,221	14,163	13,461	13,209	
SR_A		0,641	0,664	0,680	0,686	
SR_V		0,723	0,741	0,754	0,759	
S_a	g	0,128	0,133	0,136	0,137	
T_S	s	0,452	0,447	0,443	0,442	
S_d at T_S	mm	6,501	6,589	6,652	6,676	
Performance Point	S_a	g	0,071	0,057	0,069	0,072
	S_d	mm	12,062	15,344	13,159	12,721
Maximum Total Drift (TD)		0,0049	0,0063	0,0054	0,0052	
Maximum Inelastic Drift (ID)		0,0029	0,0031	0,0023	0,0023	



(a)



(b)

Figure 4.17. *To be continued*

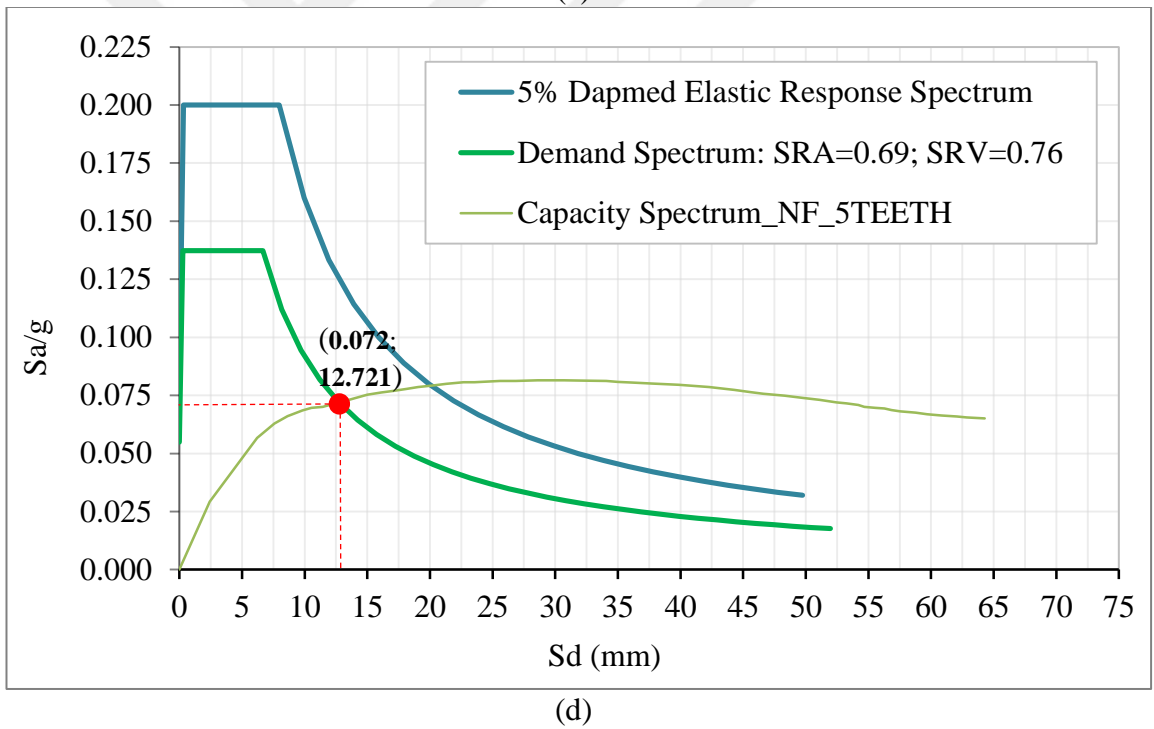
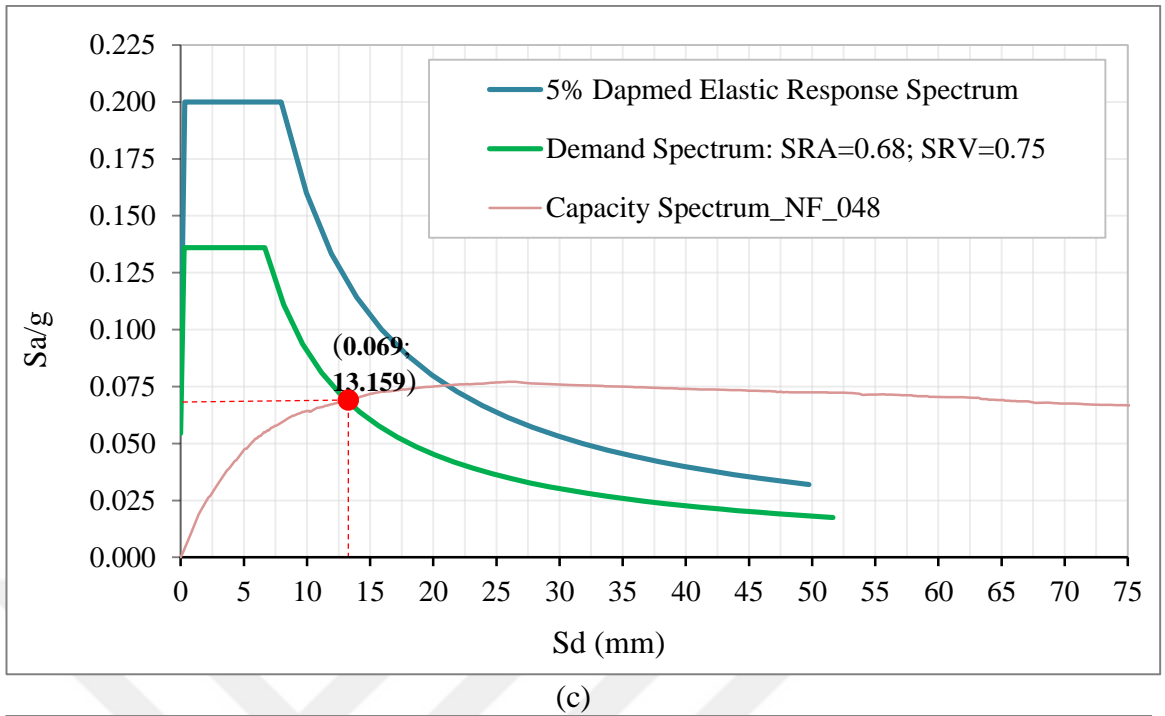


Figure 4.17. Performance Point. (a) CF; (b) NF; (c) NF_048; and (d) NF_5TEETH

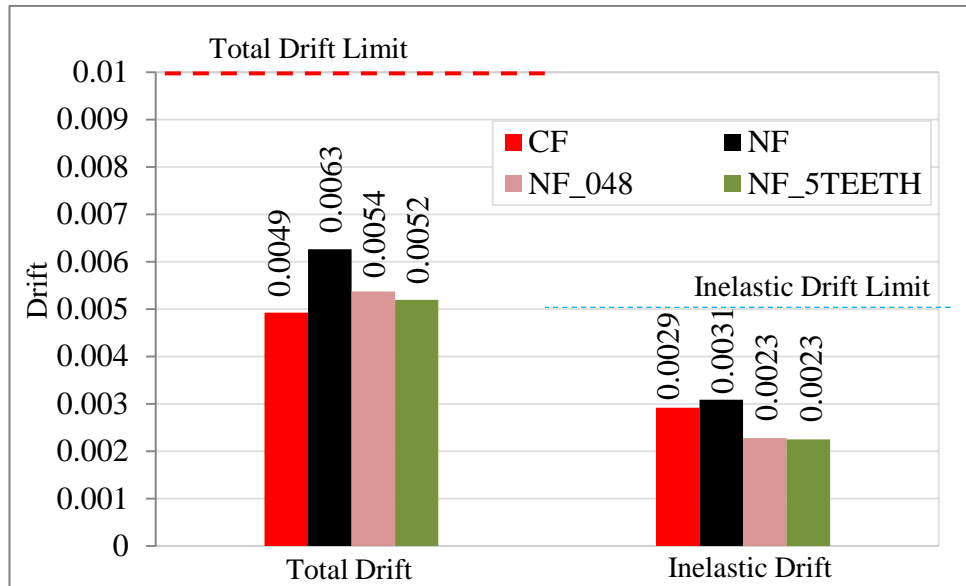


Figure 4.18. Drift Comparison.

The graphical presentation in Figure 4.17 and bar chart in Figure 4.18 provide a clear comparison of the nonlinear performance of structures built using RC formworks with and without surface treatment method and the monolithic one based on performance points. Key simulative findings suggest that the structure formed using RC formworks performing a lower capacity than the reference monolithic one is able to be tremendously enhanced by using surface treatment methods.

Performance points determined under a same seismic condition indicate that NF is weaker than its reference specimen CF. NF performs a lower value of spectral acceleration 0.057g, about 80% of the performance of CF. Besides that it experiences larger lateral displacement up to 15,344mm compared with the value of 12,062mm for CF. Slippage between concrete substrates leads to the degradation of stiffness followed by a lower flexural capacity for NF compared to CF.

The performance of the structure working with RC formworks is enhanced remarkably when the interface surfaces are treated. Firstly, the structure applied steel shear connectors with a ratio of 0,48% meets a performance point closer to the one of CF than NF with left as-cast surfaces. The spectral acceleration of NF_048 is about 0,069g, about 97,439% of the one of CF, compared to 0,057g of NF. Compare to the

performance of NF, a tremendous enhancement of about 20,878% benefitted by applying 0,48% shear connectors is exceeded by the improvement contributed by shaping rectangular asperities at the interface surface. Irregularities not only enhances the spectral acceleration of NF_5TEETH up to 26,25% compared with the case of smooth surface but also behaves as a slightly stronger structure than the monolithic one CF when performing 0,072g spectral acceleration compared with 0,071g of CF. Secondly, Performance point is determined at larger value of lateral displacement for NF in comparison with the performance of the monolithic one but the considered parameter is shortened remarkably by treating surfaces. NF experiences a maximum lateral displacement of 15,344mm, 3,282mm larger than the assumed collapsed point of the monolithic one. The exceedance, however, is shortened to 1,097mm and 0,695mm in case of NF_048 and NF_5TEETH. It can be concluded from these statistics that under seismic condition the performance of the structure formed using RC formworks does not deviate significantly from the monolithic specimen.

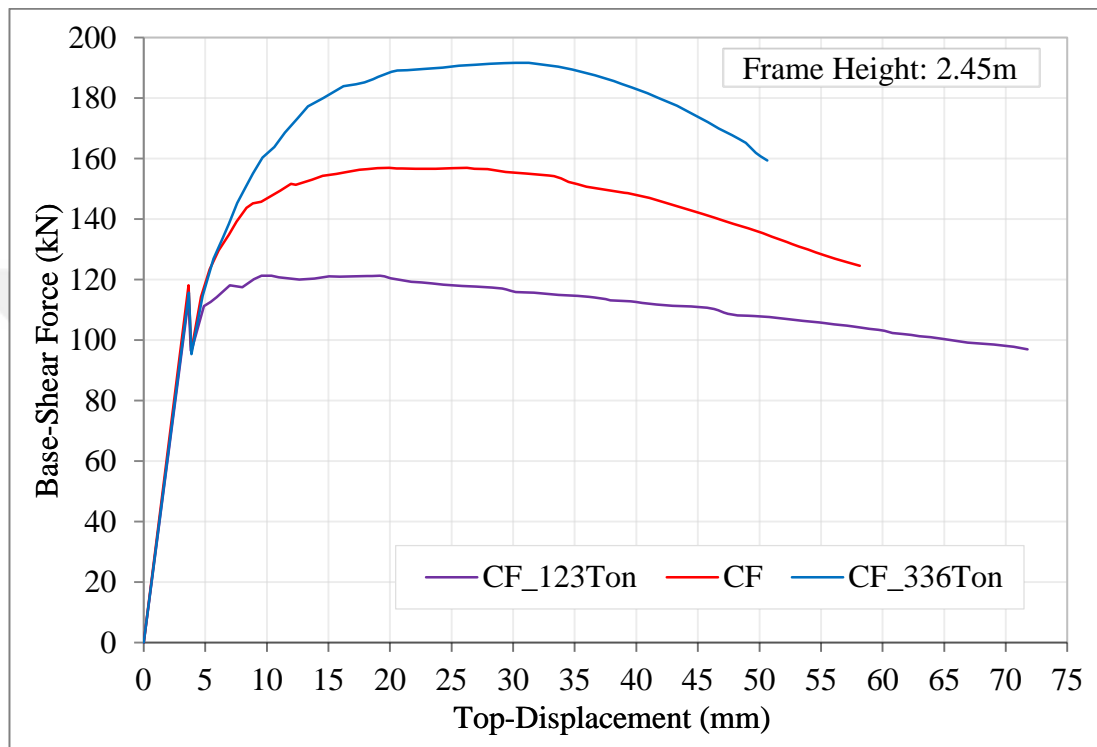
When applied to code ATC 40 (1996), particularly IO level, as seen in Figure 4.18, NF, the weakest structure, is still able to withstand the certain earthquake condition. The maximum total drift and maximum inelastic drift are 0,0063 and 0,0031 is smaller than the relative limitation, 0,01 and 0,005 respectively. The couple parameter is considered as smaller, 0,0054 and 0,0023, and 0,0052 and 0,023, for NF_048 and NF_5TEETH, respectively. After applying surface treatment methods, the structure using RC formworks performs approximately as strong as the monolithic one.

4.6. The Influence of The Intensity of Normal Load on Performance Point

In the present study, the influence of the intensity of normal load on the nonlinear performance of structures is also evaluated. It is worth noting that in the previous parts, a mass of 219 Ton has been applied constantly on all of structures during pushover analysis. In this part, normal loads comparable to 123Ton and 336 Ton are applied on both of CF and NF. In order to prevent misleading situation, the models names comprise two parts, letter and number. The first part falls into CF or NF while the latter is set as 123, 219, or 336 representing to the relative mass that is set in Ton unit us applied on considered structures.

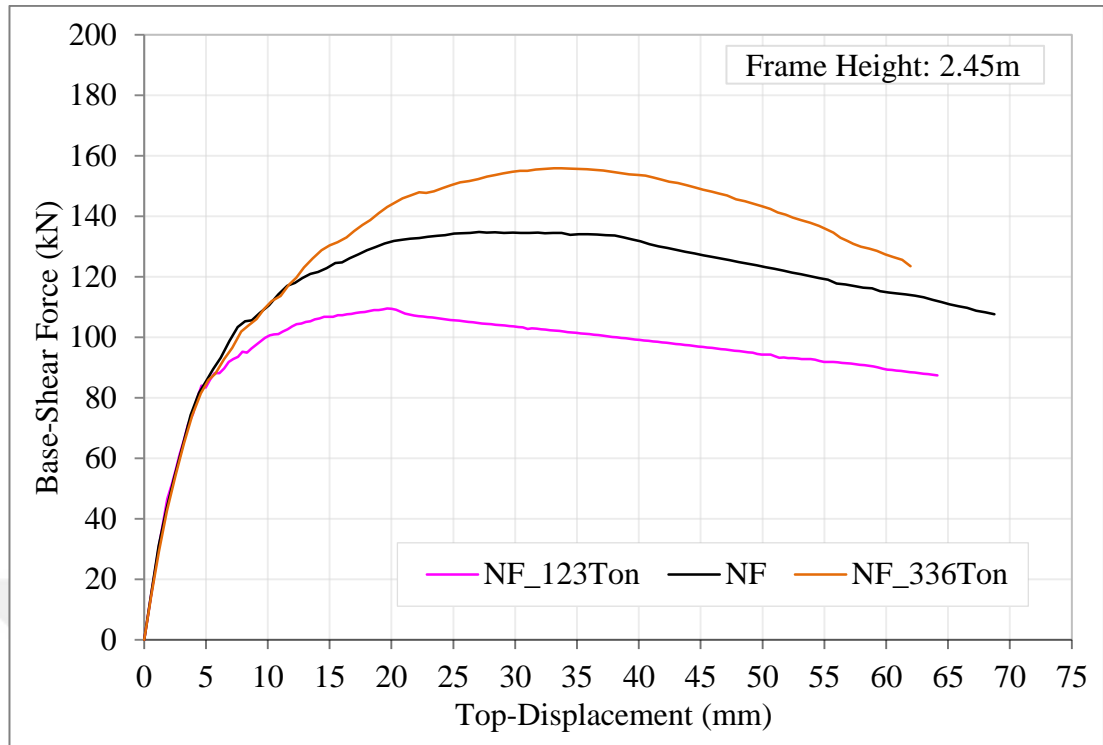
4.6.1. Flexural capacity

First of all, recalling the procedure of pushover analysis that has been carried out before, the base shear versus top displacement curves of six simulative models is determined (Figure 4.19).

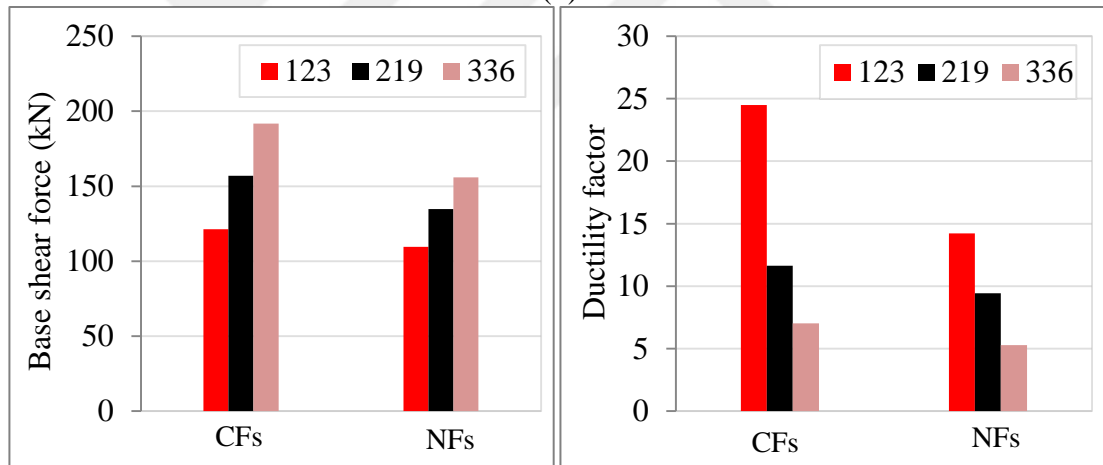


(a)

Figure 4.19. To be continued



(b)



(c)

Figure 4.19. Flexural performance. (a) CF series (b) NF series (c) a comparison

Presented for consideration in the line graphs as well as bar charts detailing figures for the nonlinear behavior of CF and NF during laterally pushing according to pushover analysis procedure. In both cases of CF and NF, $V_{base}-\Delta_{roof}$ curves graphically demonstrate that heavier mass resulting in higher value of flexural capacity observed occurring more lately leads to a lower ductile performance shown through ductility factor.

Although the flexural behavior of three cases of applied normal loads is identical approximately in the elastic regime, significant deviations initiate at lateral displacements of about 3,6mm and 4,6mm in case of CF and NF respectively. Afterward, each curve hits peak whose value increases in proportion to the increase in the intensity of normal pressure on columns, particularly 121,285kN, 156,979kN, and 191,698kN for CFs and 109,506kN, 134,852kN, and 155,936kN for NF. Increasing applied mass, in other words increasing normal load, upgrades the flexural behavior of structures due to the fact that the compressive stress applied on elements on the tensile side eliminates the negative influence of normal tensile stress. It means that cracking of concrete and yielding of longitudinal reinforcing bars are prevented somewhat and then occur later than the elements only working under tensile sides. Besides that the normal load causes the expansion in its perpendicular direction of all compressed elements. That leads to the increasing of the contribution of confined concrete parts covered by stirrups.

The statistics show that the amount of the flexural strength enhancement based on the increase in normal load is considered is higher than for CF. When comparing to the case of 123Ton, the bending capacity improvement brought by a mass of 219Ton and 336Ton are about 29,429% and 58,055% for CF while the respective values for NF are 23,146% and 42,399%. It means the normal load upgrades the bending capacity more effectively for a monolithic structure than a structure with RC formworks. It can be straightforwardly explained that the normal load is applied on whole areas of columns surfaces in case of CF while it is only subjected to the core parts surfaces of the columns of NF. The situation causes larger deviation of the bending capacity between CF and NF when applying heavier masses. Particularly a downward trend in flexural behavior of NF compared to those of CF is illustrated by statistic data of 90,288%, 85,905%, and 81,344% when applying masses of 123Ton, 219Ton, and 336Ton respectively.

Graphically observe that the ultimate value of bending strength of the structure occur later when a heavier mass is applied. The peak is witnessed at 9,558mm, 19,953mm, and 30,206mm for CF and 19,666mm, 27,082mm, and 33,131 when applying 123Ton,

219Ton, and 336 Ton respectively. The prompt descending of a structure carrying lighter mass compared to the one applied more intense load is the negative influence of normal stress. The compressive stress brought by applied mass combine with compressive stress caused by bending results in more premature crushing of element in compressive sides, especially the element in perimeters. After touching peak, the descending branch of structures carrying heavier mass is steeper and end up more promptly. Consequently, the ductility factor of those structures is assumedly smaller.

Carrying lighter mass leads to higher ductile performance. The ductility factor of CF_123 is 24,5% compared with 11,64% and 6,79% for CF_219 and CF_336 respectively. Similarly to the behavior of CFs, NF performs the highest ductility factor, 14,214%, when being applied to the lightest mass and the value is decreased to 9,439% and 5,293% corresponding to the increase of mass. Besides that, compared to the monolithic frame, NF always performs lower value of ductility factor. However, this deviation is considered to become lighter when higher mass is applied. A mass of 336Ton results in a difference of 1,743% whereas the percentage of 2,203 and 10,286 is witnessed when decreasing the applied mass to 219Ton and 123 Ton respectively.

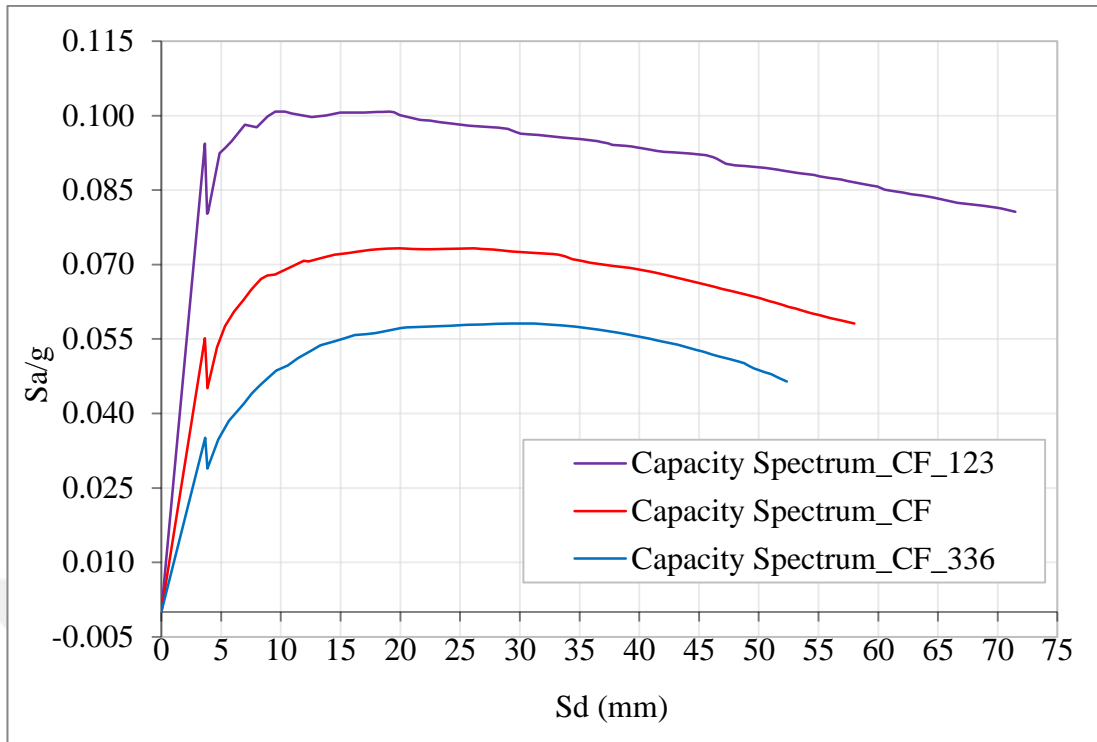
It can be said that although the structures carrying lightest mass, 123Ton performs the lowest flexural capacity, they are considered as the most ductile structures. When seismic conditions are applied, the ductility factor of a structure plays an important role in figuring out its performance point.

4.6.2. Performance point

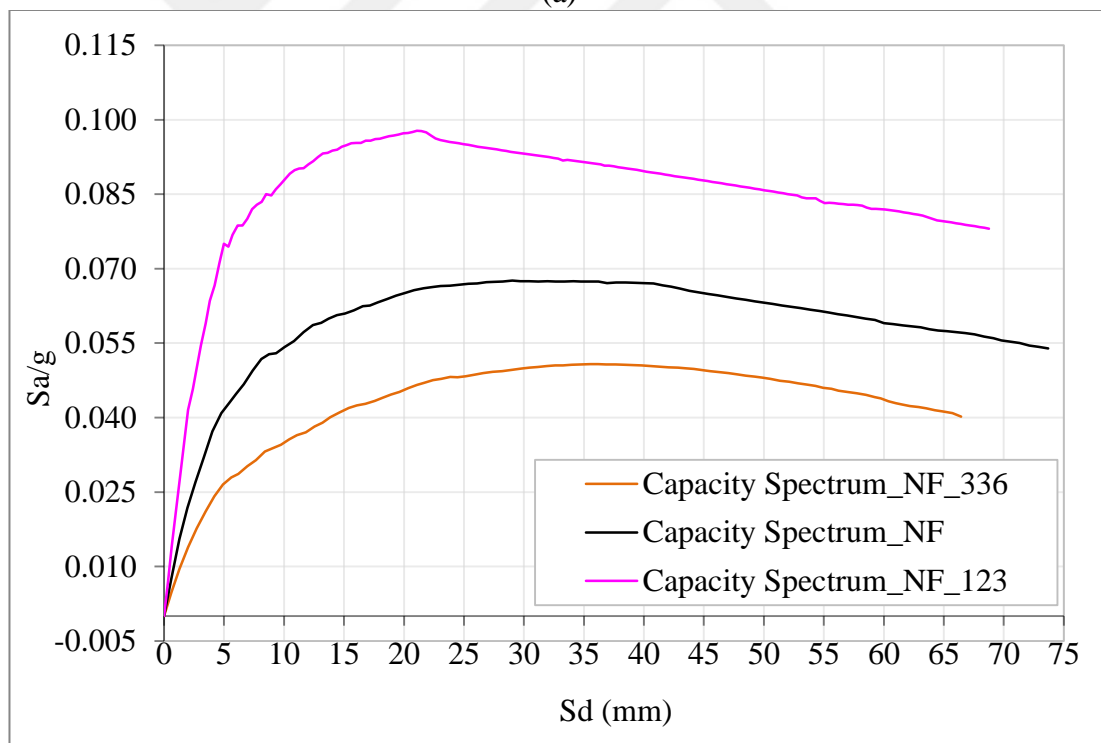
Recalling ACT 40 (1996) from Chapter 2, the capacity spectrum of each structure is rapidly obtained by conversing from its base shear versus top displacement curve obtained above.

4.6.2.1. Capacity spectrum

First of all, the capacity spectrum of models is compared to each other (Figure 4.20).

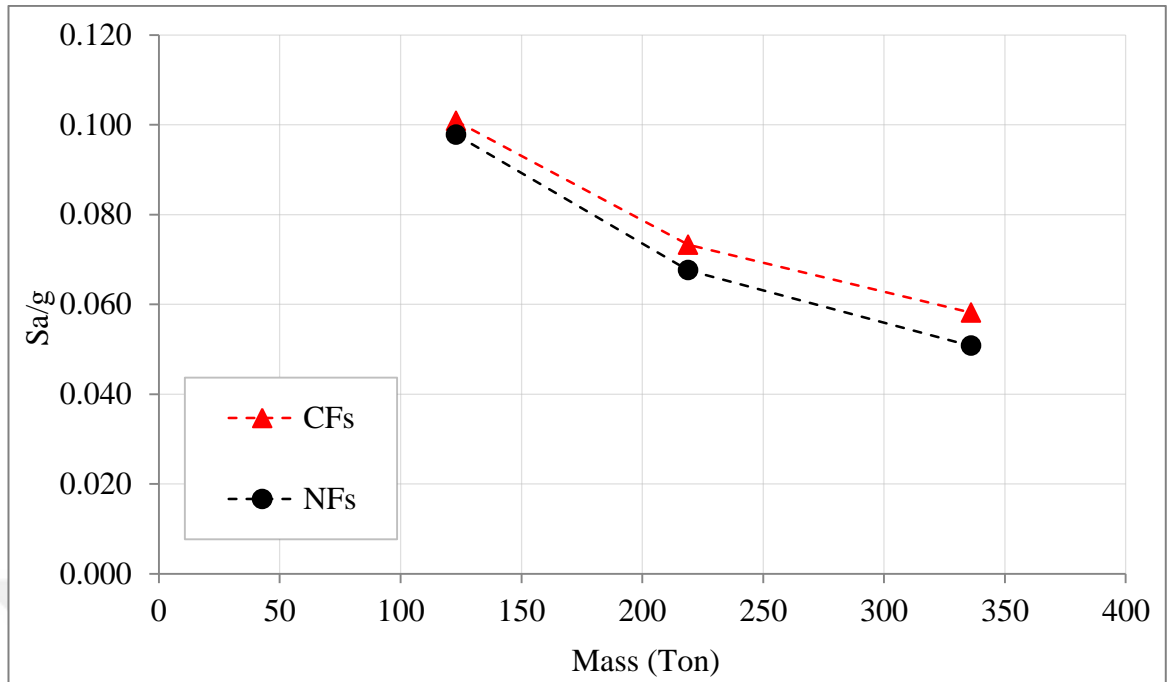


(a)



(b)

Figure 4.20. *To be continued*



(c)

Figure 4.20. ADRS. (a) CFs; (b) NFs; and (c) an overall comparison

The ADRS of the series of CF and NF in Figure 4.20 shows the remarkable influence of normal loading on the seismic capacity of RC structures. Contrary to the bending capacity enhancement brought by the increase of applied mass that has been discussed before, in both cases of F and NF, heavier masses causes a significant decrease of spectral acceleration of structure, known as the most important factor to dedicate whether a structure can stand a specific seismic condition or not. Besides at, the spectral capacity of NFs is always lower than the performance of CFs at a same level of mass.

RC structures subjected to lighter mass perform strongly than ones carrying higher intensity of normal load. The maximum value of spectral acceleration is witnessed as 0,101g and 0,098g for CF₁₂₃ and NF₁₂₃. The considered value is reduced to 0,073g, 0,058g for CF and 0,068g and 0,051g for NF corresponding to the application of 219Ton and 336Ton mass respectively.

As discussed before, higher mass causes larger deviation between NF and CF in terms of flexural capacity and the tendency consequently is witnessed again here in case of spectral capacity. There is no doubt explaining that the value of spectral acceleration is

calculated directly from the value of base shear force. In comparison with the monolithic frame, the spectral acceleration of NF under the loading of 123Ton is degraded from 96,956%, to 92,235% and 87,332% when the applied mass is levelled up to 219Ton and 336Ton respectively.

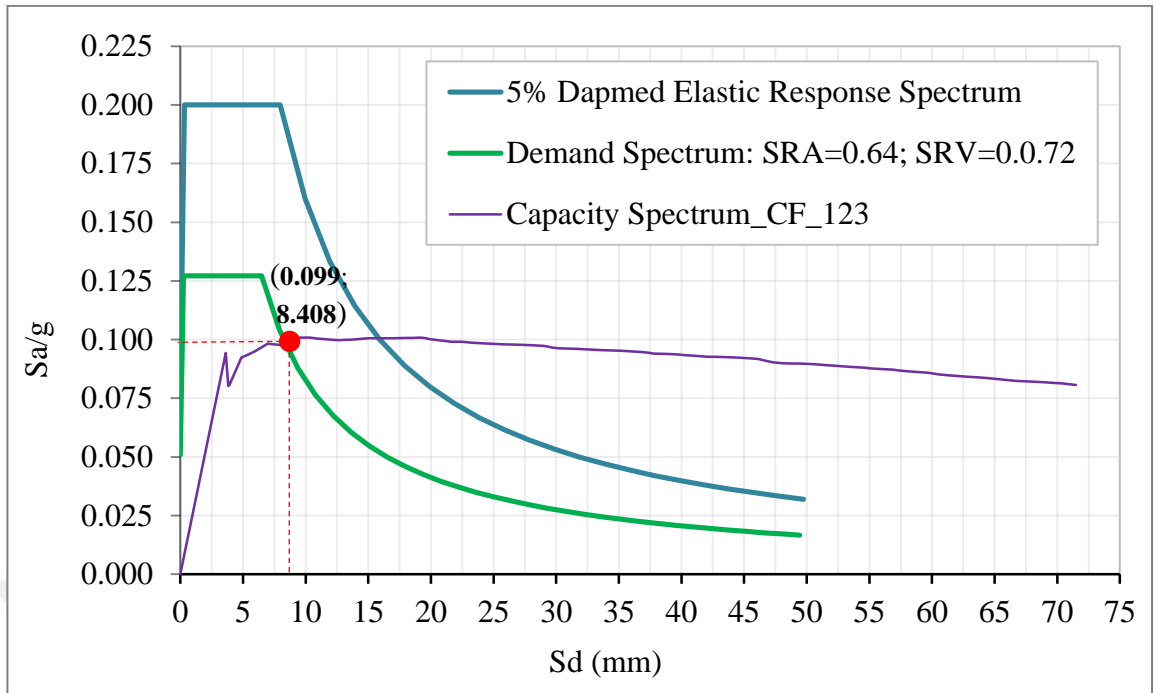
4.6.2.2. Performance point

Afterward, the performance point of structures subjected to the selected seismic condition can be figured out straightforwardly (Table 4.6, Figure 4.21, and Figure 4.22).

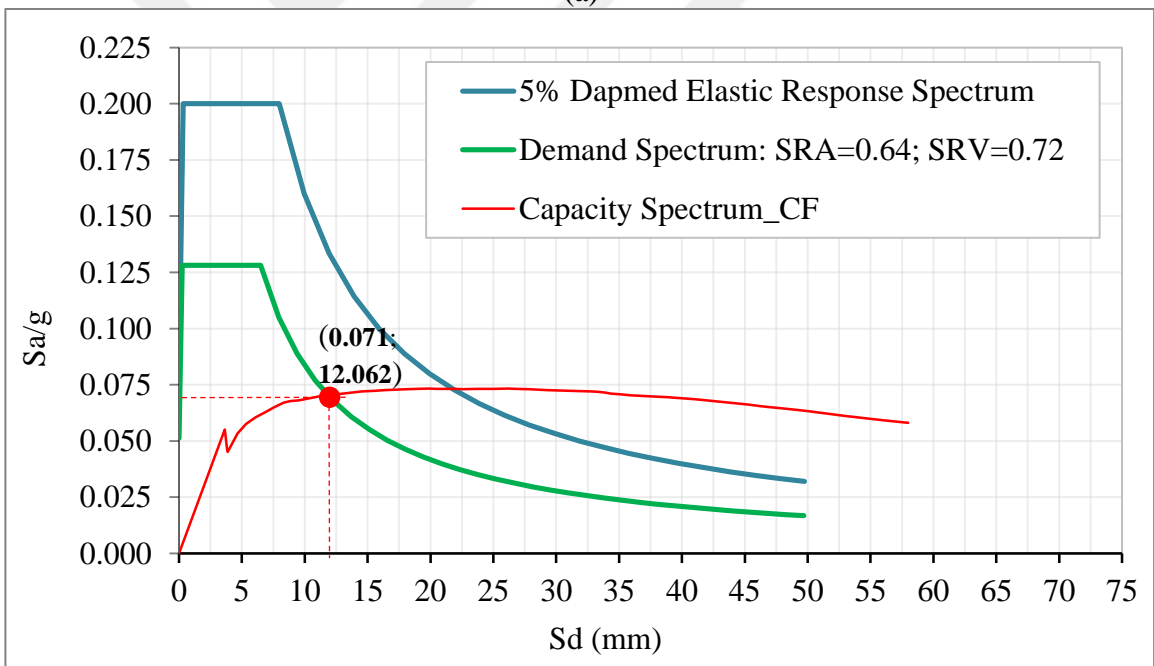
Table 4.6. Performance Points

Parameter	Unit	Model						
		CF_123	CF	CF_336	NF_123	NF	NF_336	
T	s	0,287	0,384	0,476	0,285	0,381	0,472	
PF		1,004	1,003	1,002	0,932	0,933	0,932	
α		0,998	0,999	0,999	0,930	0,930	0,931	
g	mm/s ²	9810	9810	9810	9810	9810	9810	
W	Ton	123	219	336	123	219	336	
C _A	g	0,080	0,080	0,080	0,080	0,080	0,080	
C _V	g	0,080	0,080	0,080	0,080	0,080	0,080	
a _{pi}	g	0,099	0,071	0,053	0,089	0,057	0,046	
d _{pi}	mm	8,675	12,062	15,500	10,430	15,086	20,489	
a _y	g	0,088	0,056	0,038	0,063	0,037	0,026	
d _y	g	3,408	3,679	3,967	2,868	3,179	3,416	
β_o	%	31,686	30,973	29,603	27,611	27,766	25,948	
κ		0,330	0,330	0,330	0,330	0,330	0,330	
β_{ff}	%	15,456	15,221	14,769	14,112	14,163	13,563	
SR _A		0,636	0,641	0,651	0,665	0,664	0,678	
SR _V		0,720	0,723	0,731	0,742	0,741	0,752	
S _a	g	0,127	0,128	0,130	0,133	0,133	0,136	
T _S	s	0,453	0,452	0,449	0,446	0,447	0,444	
S _d at T _S	mm	6,482	6,501	6,538	6,594	6,589	6,643	
Performance Point	S _a	g	0,099	0,071	0,055	0,088	0,057	0,045
	S _d	mm	8,408	12,062	15,413	10,026	15,344	19,848
Maximum Total Drift (TD)		0,0034	0,0049	0,0063	0,0041	0,0063	0,0081	
Maximum Inelastic Drift (ID)		0,0022	0,0029	0,0033	0,0021	0,0031	0,0030	

Table 4.6 displays crucial parameters used to determine the performance point of a series model of CFs depicted in Figure 4.21. A comparison among them is set up herein in order to evaluate the influence of the rate of normal load on structures prone to earthquake events. In general, the capacity spectrum of models intersects a demand spectrum reduced from 5% damped elastic design spectrum multiplying a couple parameters SR_A and SR_V considered to be approximately identical to each other. Besides that, notwithstanding the fact that the energy dissipated by damping E_D to the maximum strain energy E_{so} does not change significantly when CF and NF are loaded by different masses. It can be observed from Table 4.6 that although applied mass causes structures reach remarkably different performance points but the equivalent viscous damping β_o , around 30% for CF and 27% for NF, as well as the effective viscous damping β_{ff} around, 15% for CF and 14% for NF, and spectral reduction factors SR_A and SR_V does not significant different from each other in each case of structure. It can be seen graphically the performance of three structures of CF lie on demand spectrum approximate close to each other because they are reduced from 5% damped elastic multiplying approximate same value of SR_A and SR_V . The tendency is witnessed again in case of NF. However, the effective damping of CF in any case of mass is higher than those of NF, more than 1%, due to the fact that under seismic conditions, the monolithic frame, CF dissipates energy more effectively than NF built using RC formworks.

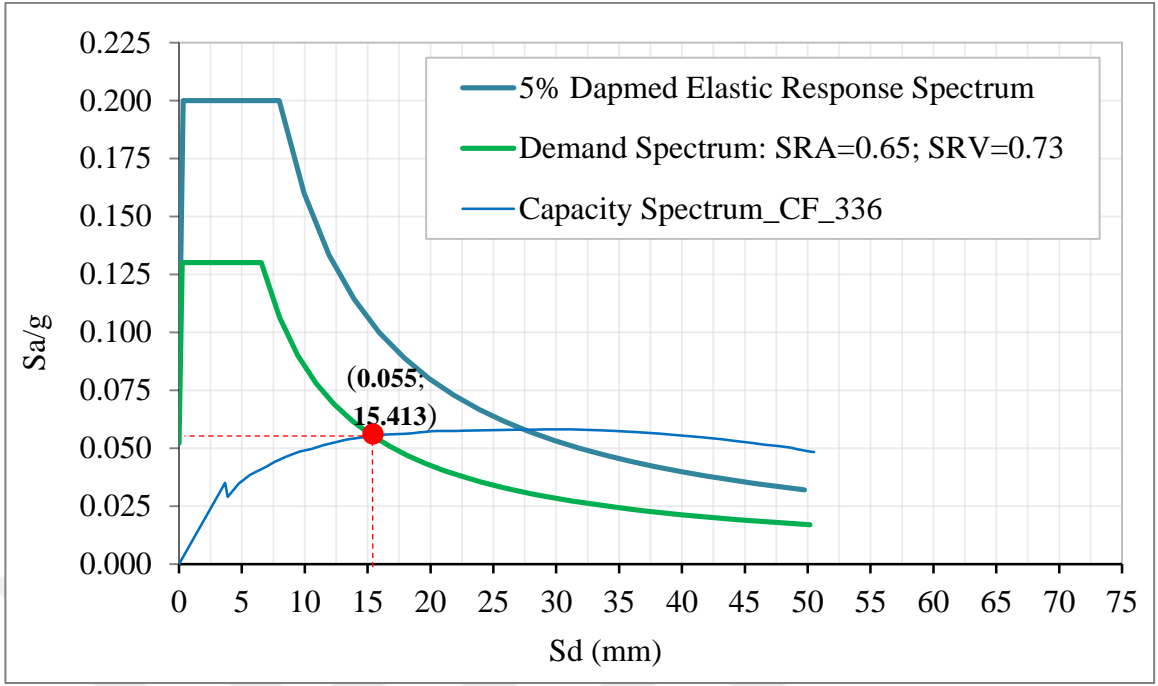


(a)



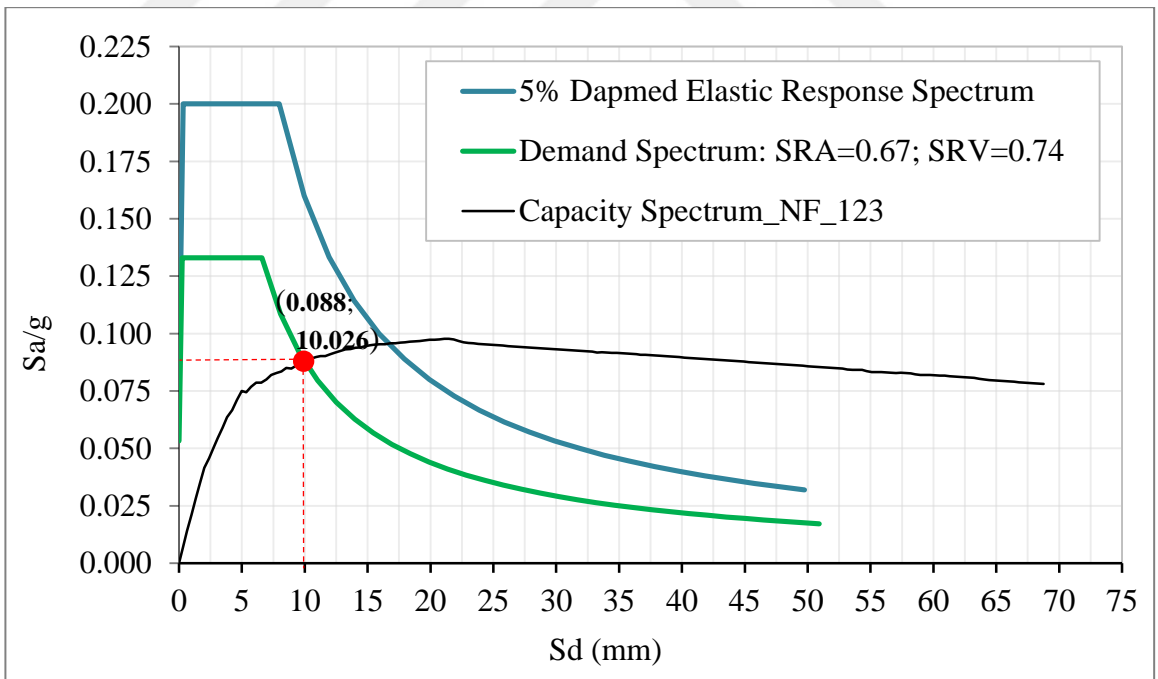
(b)

Figure 4.21. *To be continued*



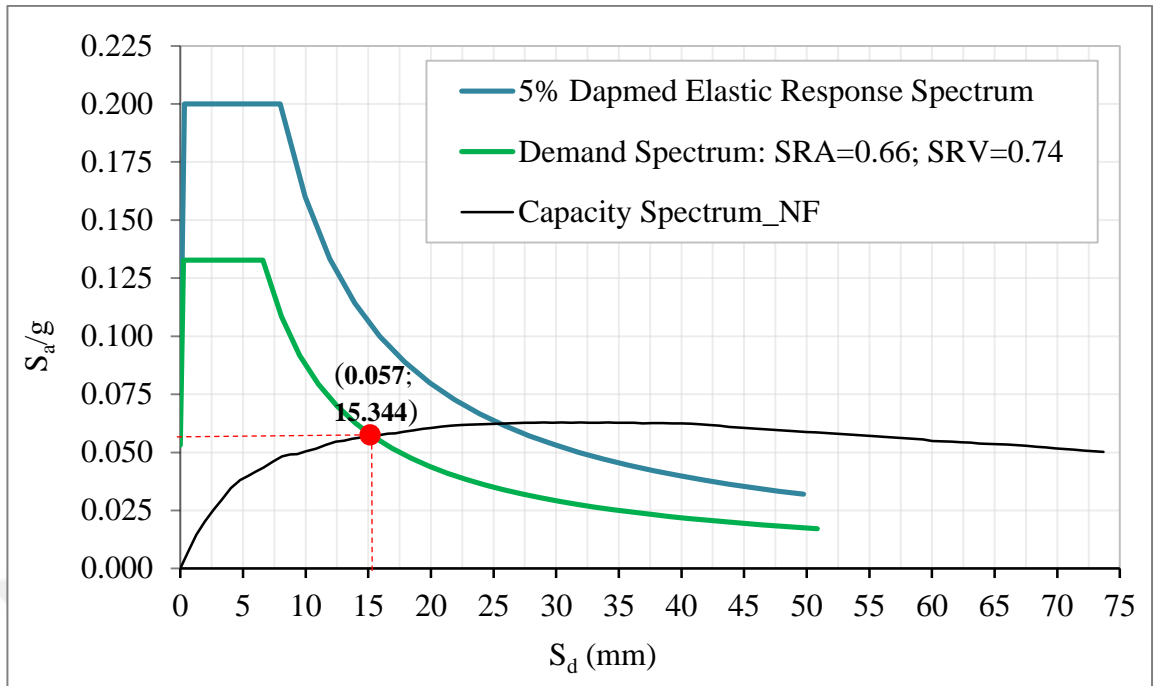
(c)

Figure 4.21. Performance Point. (a) CF_123 (b) CF_219 (c) CF_336

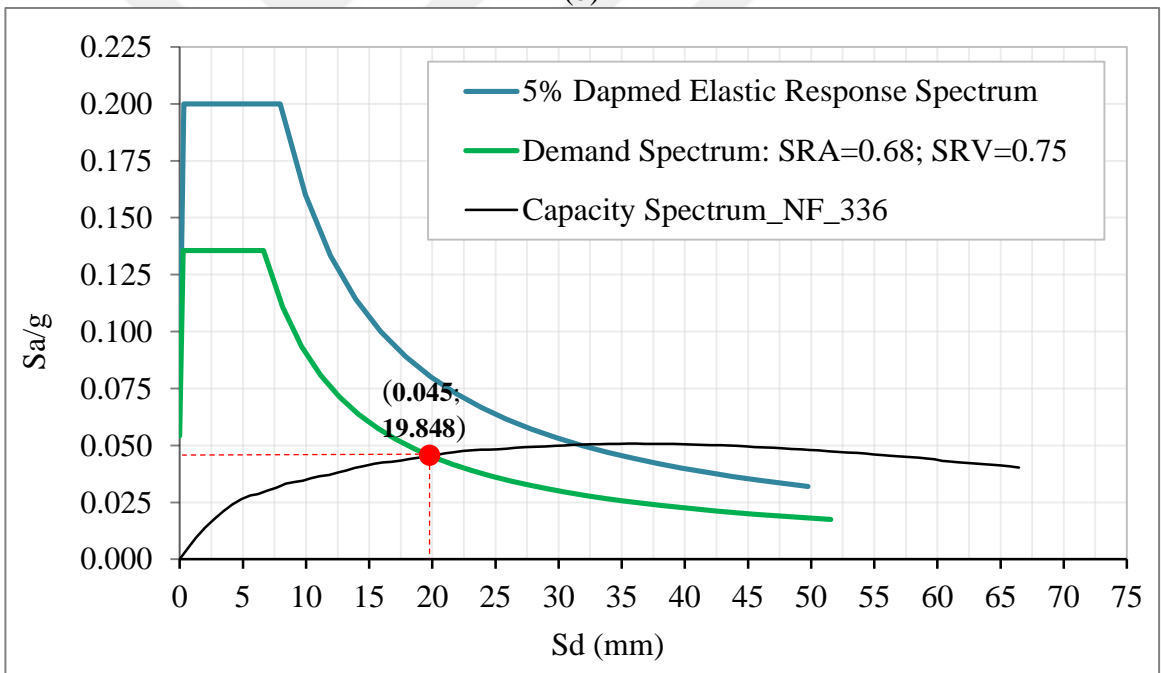


(a)

Figure 4.22. *To be continued*



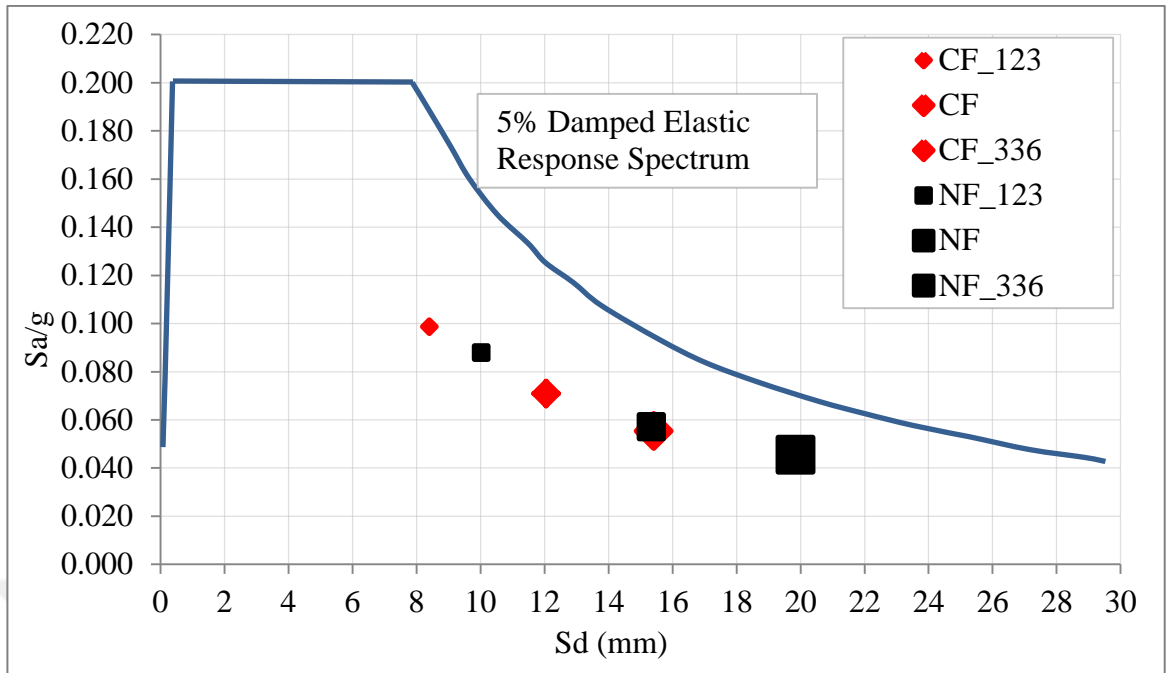
(b)



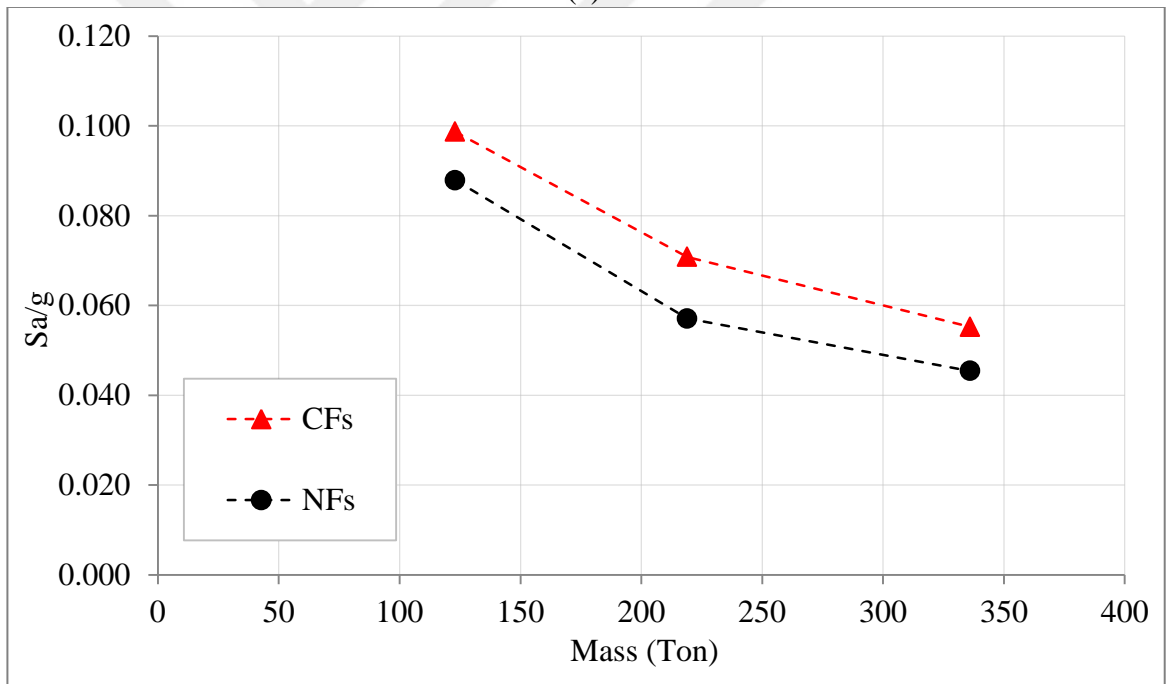
(c)

Figure 4.22. Performance Point. (a) NF_123 (b) NF_219 (c) NF_336

After that in order to take an overlook at the performance point of each structure, a detailed overlay is depicted (Figure 4.23).

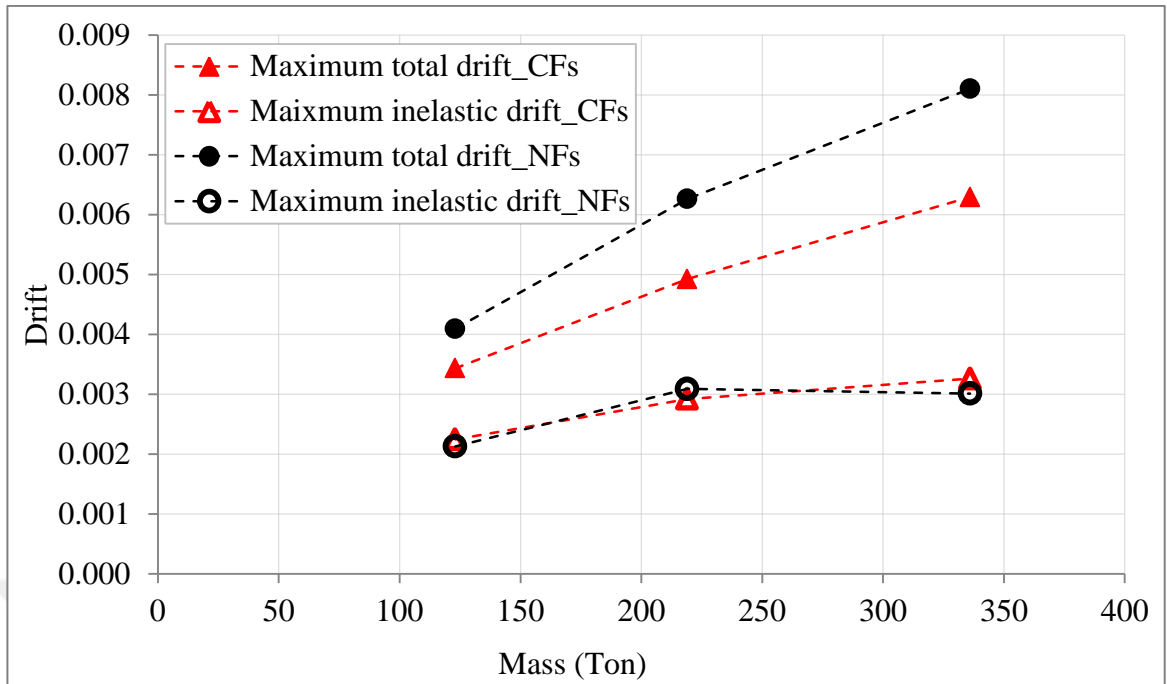


(a)



(b)

Figure 4.23. To be continued



(c)

Figure 4.23. A comparison of performance point.

Displayed on Figure 4.22 and 4.23 are data about the performance point of structures which is determined under the specific seismic condition. One of the more prominent takeaways of the figure is that heavier mass causes weaker earthquake resisting capacity of both of CF and NF, as meeting performance point at a lower value of spectral acceleration and a higher value of spectral displacement. Besides that, remarkable information pointed out from the figure is that under the same seismic conditions NF is suffered more significantly when the reduced amount of spectral acceleration at each level of mass is always more than the factor obtained for CF.

Figure 4.23.a and 4.23.b show clearly about a weakening process of CF and NF when increasing the level of applied mass. It is straightforwardly understood basing modal analysis theory that the value of spectral acceleration opposes the applied mass. In case of CF, when 123Ton mass is applied the value of spectral acceleration is about 0,099g followed by a value of 0,071g corresponding to a reduction of 28,262%, and a degraded amount up to 44,301% is a consequence of a mass of 336Ton. A similar event transpired in NF, in which the inclination of 35,069% witnessed when increasing the mass from 123Ton to 219Ton is accumulated to become 48,325% when applied mass

reaches 336Ton. The statistics lead to a conclusion that the strength against earthquake events of NF decreasingly deviates from the capacity of CF when more intense of mass is applied.

Nonetheless the performance point of each structure is determined at a lower level than its capacity in terms of spectral acceleration, particularly a reduced quantity of $2,153.10^{-03}g$, $2,482.10^{-03}g$, and $2,913.10^{-03}g$ for CF under a mass of 123Ton, 219 Ton, and 336 Ton respectively. The reduction is more remarkable in case of NF, as $9,880.10^{-03}g$, $1,052.10^{-02}g$, and $5,364.10^{-03}g$ for NF_123, NF_219, and NF_336 respectively. That is a consequence of selecting a light earthquake motion compared with the capacity of structures. Observe that, if a more intense of earthquake were applied, the ground motion resistance of NF could be improved to be closer to the one of CF.

In terms of spectral displacement, a trend of substantial increase is plainly discernible in CF as well as NF. Based on the performance point where a spectral capacity intersect demand response spectrum, maximum lateral displacement is about 15,413mm and 19,848mm for CF and NF when working under a mass of 336Ton. A lighter mass resulting in a higher value of spectral acceleration makes the structure carrying it meets the corresponding performance point at a smaller distance of lateral journey, as 12,062mm and 8,408mm is witnessed in case of CF while NF always experience larger distance, particularly 15,33mm and 10,026mm when decreasing the mass to 219Ton and 123Ton respectively.

In order to determine whether a structure is able to survive or not under a specific ground motion the maximum total drift and maximum inelastic drift are check based on the deformation limits stipulated by ACT 40 (1996). First of all, based on Figure 4.23.c it is strongly concluded that the certain ground motion seems to not strong enough to cause extreme damage of a series model of CFs and NFs. All of structures are able to withstand the specific ground motion due to the fact that the limitation of maximum inter-story drift, 0,01 as well as maximum inelastic drift, 0,005 at IO level are satisfied. In other words, the structures can be damaged during the ground motion but not be collapsed and there is no problem for habitation inside. The structures carrying heavier

mass like CF_336 and NF_336 would fall into dangerous range if more intense ground motion were applied. As a consequence of the fact that performance point is determined at larger later displacement, under each value of mass, NF is always closer than to the limitation of drift. Furthermore, it is foreseeing from Figure 72.c that if more extreme earthquake motions were applied and then the structures absolutely would perform higher values of maximum lateral displacements leading to higher value of maximum drift. Consequently, the performance level of DC would be applied to check the satisfaction of the structures. Based on the deviation between the value of maximum total drift and maximum inelastic drift, the structure loaded by heaviest of load, CF_336 and NF_336 possibly would fail the limitation of maximum inelastic drift even though the condition of maximum inelastic drift is satisfied as a consequence of the fact that the heavier mass applied on structures leads them fall more deeply into inelastic regime. That can be seen graphically and numerically the ration of maximum total drift to maximum inelastic drift is higher for NF, 2,691, 2,027, and 1,923 corresponding to an applied mass of 336Ton, 219Ton, and 123Ton while the relative statistics of CF is lower, 1,931, 1,686, and 1,531.

Notwithstanding the fact that the energy dissipated by damping E_D to the maximum strain energy E_{so} does not change when a RC structure is loaded by different masses. It can be shown that mass causes structures reach remarkably different performance points but the equivalent viscous damping β_o (about 30%) as well as the effective viscous damping β_{ff} (around 15%) and spectral reduction factors SR_A (0,64) and SR_V (0,72) in three structures are considered really close to others. It can be seen graphically the performance of three structure lie on demand spectrum approximate close to each other because they are reduced from 5% damped elastic multiplying approximate same value of SRA and SRV. Following that, the effective damping is about 15% for all of them. It can be concluded that the influence of the intensity of normal load on the total dissipated energy is not significant as that has been seen the capacity spectrum as well as the flexural behavior.

4.7. Discussion

This thesis contributes an overview of the application of RC formworks on RC structures. However, the results obtained mostly base on simulation and should be compared with experimental tests.

The proposed Coulomb friction model possibly is not the perfect model that is fit completely with real surfaces. First of all, in practice, there are some shear transfer mechanisms at the concrete-to-concrete interface that cannot be recognized as well as defined in Abaqus. The ignored mechanisms possibly contribute to the shear strength of the interface as well as to the nonlinear behavior of the whole structure. Consequently, the numerical results may underestimate the strength of structures built using RC formworks. Secondly, a more exact shear resisting mechanism consisting of cohesion is assumed to play an important role in eliminating the lateral slippage and in increasing the monolithic behavior of composite elements.

The remarkable improvement due to shear connectors is observed. However it may be possibly overestimated due to following reasons. According to dowel action mechanism, in the numerical frictional model, the effectiveness is maximized when the interface surfaces are considered to be completely smooth. As mentioned before, a realistic interface cannot be left completely smooth. Consequently, the enhancement may decrease because of the natural roughness of the inter-concrete layers.

Shear connectors in the present thesis are placed uniformly on the interface surface. Another inclination of shear links should be tried in order to figure out the most effective one on dowel action mechanism. For instance, when the friction coefficient is 0,6 as estimated according to ACI 318-08 (2018) an inclination of 31° of shear connectors considered as the optimal value should be applied in order to make contribution of shear links most effective. It is noted that, under real earthquake events, the structure oscillates so that placing shear connectors with an angle different from 90° should be investigated too. Besides that, the areas placed shear connectors should be taken into account to avoid wasteful situation.

An investigation about the optimum ratio of shear links is performed for the studied frames in the present thesis. The author has recognized that the optimum ratio is extremely difficult to specify for a purpose of wide application. For instance, the quality of concrete used for RC formwork as well as for core parts can influence the effectiveness of shear links.

The thickness of RC formworks in the present study is chosen as 30 mm, with the presence of longitudinal reinforcement, the height of irregularities is only chosen as 5 mm. Different asperities should be tested in order to determine proper dimensions for considered frames.



5. CONCLUSION

The thesis has picturized an overview about the influence of the concrete-to-concrete interface on the nonlinear behavior of RC structures built using RC formworks. Some of valuable conclusions are summarized as follows

- The RC structure built using RC formworks performs a lower flexural capacity compared with the monolithic one, about 86%.
- Under same seismic conditions, when performance point is concerned, the structure covered by formworks and the monolithic frame approximately meets one demand spectrum. The RC formworks covered frame reached a spectral acceleration of 0,057g equal to 80% of the value of the monolithic one. Besides that, the fracture point of the weaker frame is about 15,344mm higher than the maximum lateral displacement of CF, about 12,062mm.
- Shear connectors plays a tremendous role in improving the shear strength of the inter-concrete substrates as well as the nonlinear behavior of whole structures. The amount of enhancement is proportional to the ratio of shear connectors placed laterally on the concrete-to-concrete surfaces. However, the improvement is not profound when applying a high amount of shear ties. The author suggests a suitable ratio of shear connectors should be around 0,48%.
- As required by ACI 318-08 (2008) rectangular shaped asperities whose dimensions of 5 mm height, 37,5 mm width, and 37,5 mm apart slightly upgrades the nonlinear behavior of NF to a higher level than the monolithic one.
- The flexural strength of structures increase in proportion to the increase of the axial force applied on columns. A force of 336 ton increases the lateral load capacity of the structure 58,1% compared to when it is loaded by 123 ton. However, under a specific seismic condition, heavier mass causes the structure becomes weaker. A normal force calculated equal to 26% of the normal compressive capacity of the structure causes a decrease of 44,4% in comparison with the case of 9,6%, or 123 ton. Besides that, a mass of 336 ton results in a larger lateral displacement. Its maximum total drift ratio is 0,0063 equal to 1,85 times the value obtained by the structure with 123 ton.

REFERENCES

- Abbas, A.A., Mohsin, S.M.S., Cotsovos, D.M. 2014.** Seismic response of steel fiber RC beam–column joints. *Engineering Structures*, 59: 261-283.
- ACI Committee 318. 2008.** ACI 318-08 Building Code Requirements for Structural Concrete. American Concrete Institute. MI 48331, USA.
- Alhadid, M.M.A., Youssef, M.A. 2016.** Analysis of RC beams strengthened using concrete jackets. *Engineering Structures*, 132: 172-187.
- Altun, F. 2004.** An experimental study of the jacketed reinforced-concrete beams under bending. *Construction and Building Materials*, 18: 611-618.
- Applied Technology Council (ATC). 1996.** Seismic Evaluation and Retrofit of Concrete Buildings. American Concrete Institute. California 94065, USA.
- Aslani, F., Jowkarmeimandi, R. 2012.** Stress-strain model for concrete under cyclic loading. *Magazine of Concrete Research*, 64(8): 673-685.
- ASTM Committee C09. 2014.** Designation: C39/C39M – 14 Standard Test Method for Compressive Strength of Cylindrical Concrete Specimens. ASTM International, 100 Barr Harbor Drive, PO Box C700, West Conshohocken, PA, 19428-2959 USA.
- A-Z PREZIP a.s. 2014.** Precast reinforced concrete structures. <http://www.azprezip.cz/en/precast-reinforced-concrete-structures/> (Date: 31.05.2018).
- Badoux, J.C., Hulsbos, C.L. 1965.** Horizontal shear connection in composite concrete beams under repeated loading. PhD Thesis. The Department of Civil Engineering at Fritz Engineering Laboratory, Lehigh University, USA.
- Beer, F.P., Johnston, E.R.J., Dewolf, J.T., Mazurek, D.F. 2009.** Mechanics of Materials. The McGraw-Hill Companies, Inc. New York City, USA, 838pp.
- Belejo, A., Bento, R., Bhatt, C. 2012.** Comparison of different computer programs to predict the seismic performance of SPEAR building by means of Pushover Analysis. The 15th World Conference on Earthquake Engineering, 24-28 September, 2012, Lisbon, Portugal.
- Caballero, F.L., Razavi, A.M.F., Stamatopoulos, C.A. 2016.** Numerical Evaluation of Earthquake Settlements of Road Embankments and Mitigation by Preloading. *Int. J. Geomech.*, 16(5): C4015006.
- Carlo, F.D., Meda, A., Rinaldi, Z. 2017.** Numerical cyclic behavior of un-corroded and corroded RC columns reinforced with HPFRC jacket. *Composite Structures*, 163: 432-443.
- Cheong, H. K., Macalevey, N. 2000.** Experimental behavior of jacketed reinforced concrete beams. *J. Struct. Eng.*, 126(6): 692-699.
- Chopra, A.K. 2012.** Dynamics of Structures Theory and Applications to Earthquake Engineering, Pearson Education, Inc., Boston, USA, 944 pp.
- Cook, R.D. 1995.** Finite Element Modeling for Stress Analysis. John Wiley & Sons, Inc. New York City, USA, 320pp.
- Dassault Systèmes. 2013.** Abaqus Analysis User's Guide, Dassault Systèmes Simulia Corp., Providence, RI, USA.
- Drucker, D.C. 1953.** Technical Report No.85 Coulomb Friction, Plasticity, and Limit Loads. Armed Services Technical Information Agency. Brown University, Providence, R.I.
- European Committee for Standardization-CEN. 2004.** EN 1992-1-1 (2004) (English): Eurocode 2: Design of concrete structures - Part 1-1: General rules and rules

for buildings. The European Union per Regulation 305/2011, Directive 98/34/EC, Directive 2004/18/EC. Avenue Marnix 17, B-1000 Brussels.

Federal Highway Administration. 2016. FHWA-HRT-05-062 Users Manual for LS-DYNA Concrete Material Model 159. Office of Research, Development, and Technology, Office of Safety, RDT.

Genikomsou, A.S., Polak, M.A. 2015. Finite element analysis of punching shear of concrete slabs using damaged plasticity model in ABAQUS. *Engineering Structures*, 98: 38–48.

Gohnert, M. 2000. Proposed theory to determine the horizontal shear between composite precast and in situ concrete. *Cement & Concrete Composites*, 22: 469-476.

Gopalaratnam, V.S., Shah, S.P. 1985. Softening response of plain concrete in direct tension. *Journal of the American Concrete Institute*, 82: 310-323.

Gromysz, K. 2008. Model of vibrations damping and friction in joint surface of composite concrete structures loaded with bending moment. *Architecture Civil Engineering Environment*, 3/2008: 57-66.

Hassanean, Y.A., Assaf, K.A., Raheem, S.E.A., Arafa, A.N.M. 2013. Flexural behavior of strengthened and repaired RC beams by using steel fiber concrete jacket under repeated load. *International Journal of Civil and Structural Engineering*, Volume 3, No 3, 564-578.

He, Y., Zhang, X., Hooton, R.D., Zhang, X. 2017. Effects of interface roughness and interface adhesion on new-to-old concrete bonding. *Construction and Building Materials*, 151: 582-590.

Hindo, K.R. 1990. In-place bond testing and surface preparation of concrete. *Concrete International*, 12: 46-48.

Hsu, L.S., Hsu, C.T.T. 1994. Complete stress-strain behavior of high-strength concrete under compression. *Magazine of Concrete Research*, 46, No. 169: 301-312.

Huang, W., Gould, P.L. 2007. A case study considering a 3-D pushover analysis procedure. Structures Congress 2007. May 16-19, 2007. Long Beach, California.

Hutchings, I. M. 2016. Leonardo da Vinci's studies of friction. *Wear*, 360-361: 51–66.

Ismail, A. 2014. Nonlinear static analysis of a retrofitted RC building. *HBRC Journal*, 10: 100-107.

Júlio, E.N.B.S., Branco, F.A.B, Silva, V.D. 2004. Concrete to concrete bond strength. Influence of the roughness of the substrate surface. *Construction and Building Materials*, 18: 675-681.

Júlio, E.N.B.S., Branco, F.A.B. 2008. RC jacketing– interface influence on cyclic loading response. *ACI Structural Journal*, 105-S45.

Kang, J.Y., Park, J.S., Jung, W.T., Keum, M.S.. 2015. Connection between Concrete Layers with Different Strengths. *Engineering*, 7, 365-372.

Karsan, A.I., Jirsa, J.O. 1969. Behavior of Concrete under Compressive Loadings, *Journal of the Structural Division, ASCE*, Vol. 95: 2535-2563.

Khalil, A.E., Etman, E., Atta, A., Essam, M. 2016. Nonlinear behavior of RC beams strengthened with strain hardening cementitious composites subjected to monotonic and cyclic loads. *Alexandria Engineering Journal*, 55: 1483–1496.

Kothari, P., Parulekar, Y.M., Reddy, G.R., Gopalakrishnan, N. 2017. In-structure response spectra considering nonlinearity of RC C structures: experiments and analysis. *Nuclear Engineering and Design*, 322: 379-396.

Kupfer, H., Hilsdorf, H.K., Rusch, H. 1969. Behavior of Concrete under Biaxial Stresses. *ACI Journal*, No. 66-52: 656-666.

- Kwon, T.H., Hong, E.S., Cho, G.C. 2009.** Shear Behavior of Rectangular-shaped Asperities in Rock Joints. *KSCE Journal of Civil Engineering*, 14(3):323-332.
- Lampropoulos, A.P., Dritsos, S.E. 2011.** Modeling of RC columns strengthened with RCjackets. *Earthquake Eng. Struct. Dyn.*, 40:1689-1705.
- Lee, C.H., Polycarpou, A.A. 2007.** Static Friction Experiments and Verification of an Improved Elastic-Plastic Model Including Roughness Effects. *Journal of Tribology*, 129: 754-760.
- Lee, J., Fenves, G.L. 1998.** Plastic-damage model for cyclic loading of concrete structures. *J. Eng. Mech.*, 124: 892-900.
- Lubliner, J., Oliver, J., Oller, S., Oñate, E. 1989.** A plastic-damage model for concrete. *Int. J. Solids Structures*, Vol. 25 No. 3: 299-326.
- Mahmoud, M.A., Elafandy, T.H., Okail, H.O., Abdelrahman, A.A. 2013.** Interfacial shear behavior of composite flanged concrete beams. *HBRCJournal*, 10, 206–214.
- Mazizah, E.M., Izni S.I. 2015.** Interface shearing strength of concrete-to-concrete bond with and without projecting steel reinforcement. *Jurnal Teknologi*, 75:1, 169–172.
- McCrum, D.P., Amato, G., Suhail, R. 2016.** Development of seismic fragility functions for a moment resisting RC framed structure. *The Open Construction and Building Technology Journal*, 10: 42-51.
- Minafò, G. 2015.** A practical approach for the strength evaluation of RCcolumns reinforced with RCjackets. *Engineering Structures*, 85: 162-169.
- Münger, F., Wicke, M., Jirsa, J.O. 1995.** Connection of old concrete with new concrete-overlays. IABSE reports. ETH Zürich, Rämistrasse 101, 8092 Zürich, Schweiz.
- Najafgholipour, M.A., Dehghan, S.M., Dooshabi, A., Niroomandi, A. 2017.** Finite element analysis of RC beam-column connections with governing joint shear failure mode. *Latin American Journal of Solids and Structures*, 14: 1200-1225.
- Nasersaeed, H. 2011.** Evaluation of behavior and seismic retrofitting of RCstructures by concrete jacket. *Asian Journal of Applied Sciences*, 4(3): 211-228.
- Oñate, E., Oller, S., Oliver, J., Lubliner, J. 1988.** A constitutive model for cracking of concrete based on the incremental theory of plasticity. *Eng. Comput.*, Vol. 5: 309-319.
- Park, R. 1988.** State of the art report Ductility evaluation from laboratory and analytical testing. Proceeding of Ninth World Conference on Earthquake Engineering, 2-9 August 1998, Tokyo-Kyoto, Japan.
- Patton, F.D. 1966.** Multiple modes of shear failure in rock. *1st ISRM Congress*, 25 September -1 October 1966, Lisbon, Portugal.
- Peter, A. 2001.** Experimental Modal Analysis – A Simple Non-Mathematical Presentation. Peter Avitabile – Rev 052700 DRAFT DOCUMENT for Sound&Vibration Magazine. Massachusetts.
- Poleswara, R.K., Balaji, K.V.G.D., Gopal, R.S.S.S.V., Srinivasa, R. 2017.** Nonlinear pushover analysis for performance based engineering design-a review. *IJRASET*, Volume 5 Issue III: 1293-1300.
- PLYTEC formwork. 2016.** Ply Tec Green Formwork. <http://www.plytecformwork.com/>. (Date: May 31 2018)
- Ren, W., Sneed, L.H., Yang, Y., He, R. 2015.** Numerical Simulation of Prestressed Precast Concrete Bridge Deck Panels Using Damage Plasticity Model. *International Journal of Concrete Structures and Materials*, Vol.9, No.1: 45–54.
- Santos, P.M.D., Júlio, E.N.B.S. 2010.** Assessment of the Shearing strength between Concrete Layers. 8th fib PhD Symposium in Kgs, 20–23 June, 2010, Lyngby, Denmark.

- Santos, P.M.D., Júlio, E.N.B.S., Silva, V.D. 2007.** Correlation between concrete-to-concrete bond strength and the roughness of the substrate surface. *Construction and Building Materials*, 21: 1688–1695.
- Santos, P.M.D.D. 2009.** Assessment of the Shearing strength between Concrete Layers. *PhD Thesis*, Faculty of Sciences and Technology, University of Coimbra, Portugal.
- Sengottian, K., Jagadeesan, D.K. 2013.** Retrofitting of columns with RCjacketing an experimental behavior. *Journal of theoretical and applied information technology*, Vol. 56 No.2: 349-354.
- Shehata, I.A.E.M., Shehata, L.D.C.D., Santos, E.W.F., Simões., M.L.D.F. 2009.** Strengthening of RC beams in flexure by partial jacketing. *Materials and Structures*, 42: 495-504.
- Tahsiri, H., Sedehi, O., Khaloo, A., Raisi, E.M. 2015.** Experimental study of RCjacketed and CFRP strengthened RCbeams. *Construction and Building Materials*, 95: 476-485.
- Tedesco, J.W., McDougal, W.G., Ross, C.A. 1999.** Structural Dynamics Theory and Applications. Addison Wesley Longman, Inc. California, USA, 816 pp.
- The Standing Committee on Concrete Technology (SCCT). 2010.** CS1:2010 Testing Concrete. The Government of the Hong Kong Special Administrative Region. Kowloon, Hong Kong.
- Thermou, G.E. 2015.** Strengthened Structural Members and Structures: Analytical Assessment. <https://www.researchgate.net/publication/272061500>. (Date: 2018).
- Thermou, G.E., Pantazopoulou, S.J. 2009.** Reinforced polymer retrofitting of substandard RCprismatic members. *Journal of Composites for Construction*, 13(6): 535-546.
- Thermou, G.E., Pantazopoulou, S.J., Elnashai, A.S. 2007.** Flexural Behavior of Brittle RCMembers Rehabilitated with Concrete Jacketing. *J. Struct. Eng.*, 133(10): 1373-1384.
- Thermou, G.E., Papanikolaou, V.K., Kappos, A.J. 2014.** Flexural behaviour of RC jacketed columns under reversed cyclic loading. *Engineering Structures*, 76: 270-282.
- Truong,G.T., Kim, J.C., Choi, K.K.. 2017.** Seismic performance of RC columns retrofitted by various methods. *Engineering Structures*, 134: 217-235.
- Vandoros, K.G., Dritsos, S.E. 2008.** Concrete jacket construction detail effectiveness when strengthening RCcolumns. *Construction and Building Materials*, 22: 264-276.
- Wahalathantri, B.L., Thambiratnam, D.P., Chan, T.H.T, Fawzia, S. 2011.** A material model for flexural crack simulation in RC elements using Abaqus. *In Proceedings of the First International Conference on Engineering, Designing and Developing the Built Environment for Sustainable Wellbeing*, 27-29 April, 2011, Qld, Australia.
- Walker, J. 2007.** Extended Fundamental of Physics. John Wiley & Sons, Inc. NJ 07030, USA.
- Wang, W., Dai, J., Li, G., Huang, C. 2011.** Long-Term Behavior of Prestressed Old-New Concrete Composite Beams. *J. Bridge Eng.*, 16(2): 275-285.
- Wittel, F. 2018.** Mechanics of Building Materials. <https://www.ethz.ch/content/specialinterest/baug/institute-ifb/instituteifb/en/education/msc-courses/msc-mechanics-building-materials.html> (Date: May 30 2018).
- Wosatko, A., Pamin, J., Polak, M.A. 2015.** Application of damage–plasticity models in finite element analysis of punching shear. *Computers and Structures*, 151: 73–85.
- Wu, J.Y., Li, J., Faria, R. 2006.** An energy release rate-based plastic-damage model

for concrete. *International Journal of Solids and Structures*, 43: 583–612.

Zhu, Z., Bai, Y., Liu, J. 2016. Mechanical performance of shear studs and application in steel-concrete composite beams. *J. Cent. South Univ.*, 23: 2676–2687.

Zou, X.K., Chan, C.M. 2005. Optimal seismic performance-based design of RC buildings using nonlinear pushover analysis. *Engineering Structures*, 27: 1289-1302.



APPENDICES

APPENDIX A. Dynamic Characteristics

APPENDIX B. Data of Pushover Curve and Capacity Spectrum



APPENDIX A. Dynamic Characteristics

The dynamic characteristics of structures including the first 7 modes extracted from Abaqus are listed herein.

Table A.1 Dynamic Characteristics Without Mass

Model	Mode	Frequency	Period	Effective Mass				Participation Factor	
				X		Z		X	Z
				(Ton)	(%)	(Ton)	(%)		
CF	1	19,860	0,050	5,0E-06	0,000	3,2E+00	95,982	-0,002	1,222
	2	19,883	0,050	3,2E+00	95,988	5,0E-06	0,000	1,222	0,002
	3	25,022	0,040	9,8E-07	0,000	3,7E-10	0,000	-0,001	0,000
	4	34,893	0,029	7,6E-08	0,000	9,6E-13	0,000	0,000	0,000
	5	56,444	0,018	4,0E-11	0,000	9,3E-12	0,000	0,000	0,000
	6	82,296	0,012	4,1E-09	0,000	3,1E-11	0,000	0,000	0,000
	7	85,453	0,012	8,9E-09	0,000	1,6E-10	0,000	0,000	0,000

NF	1	19,837	0,050	3,7E-04	0,011	3,3E+00	95,904	-0,013	1,219
	2	19,847	0,050	3,3E+00	95,911	3,7E-04	0,011	1,219	0,013
	3	24,949	0,040	3,3E-08	0,000	2,1E-08	0,000	0,000	0,000
	4	35,077	0,029	2,9E-10	0,000	1,0E-09	0,000	0,000	0,000
	5	57,152	0,017	3,3E-14	0,000	3,2E-11	0,000	0,000	0,000
	6	82,623	0,012	2,6E-09	0,000	1,9E-09	0,000	0,000	0,000
	7	85,864	0,012	7,7E-13	0,000	6,9E-11	0,000	0,000	0,000

Table A.2 Dynamic Characteristics With Mass

Model	Mode	Frequency	Period	Effective Mass				Participation Factor	
				X		Z		X	Z
				(Ton)	(%)	(Ton)	(%)		
CF	1	2,605	0,384	9,4E-02	0,043	2,2E+02	99,888	-0,021	1,003
	2	2,607	0,384	2,2E+02	99,888	9,4E-02	0,043	1,003	0,021
	3	20,936	0,048	2,6E-09	0,000	2,8E-09	0,000	0,000	0,000
	4	28,335	0,035	1,3E-07	0,000	1,1E-11	0,000	0,000	0,000

Table A.2 Dynamic Characteristics With Mass (Cont.)

	5	126,542	0,008	1,2E-07	0,000	4,1E-07	0,000	0,000	0,001
	6	134,222	0,007	7,3E-04	0,000	8,5E-01	0,389	-0,045	1,522
	7	134,237	0,007	8,5E-01	0,388	7,3E-04	0,000	1,522	0,045

CF_123	1	3,481	0,287	5,2E-02	0,043	1,2E+02	99,834	-0,021	1,004
	2	3,483	0,287	1,2E+02	99,834	5,2E-02	0,043	1,004	0,021
	3	27,976	0,036	1,6E-09	0,000	1,7E-09	0,000	0,000	0,000
	4	28,335	0,035	1,3E-07	0,000	1,1E-11	0,000	0,000	0,000
	5	126,542	0,008	1,2E-07	0,000	4,1E-07	0,000	0,000	0,001
	6	134,223	0,007	7,3E-04	0,001	8,5E-01	0,692	-0,045	1,522
	7	134,239	0,007	8,5E-01	0,691	7,3E-04	0,001	1,521	0,045

CF_336	1	2,099	0,476	1,4E-01	0,043	3,4E+02	99,912	-0,021	1,002
	2	2,100	0,476	3,4E+02	99,912	1,4E-01	0,043	1,002	0,021
	3	16,867	0,059	3,8E-09	0,000	4,2E-09	0,000	0,000	0,000
	4	28,335	0,035	1,3E-07	0,000	1,1E-11	0,000	0,000	0,000
	5	126,542	0,008	1,2E-07	0,000	4,1E-07	0,000	0,000	0,001
	6	134,221	0,007	7,3E-04	0,000	8,5E-01	0,253	-0,045	1,523
	7	134,236	0,007	8,5E-01	0,253	7,3E-04	0,000	1,522	0,045

NF	1	2,627	0,381	1,5E+01	6,889	2,0E+02	93,039	-0,254	0,933
	2	2,627	0,381	2,0E+02	93,039	1,5E+01	6,889	0,933	0,254
	3	21,074	0,047	2,6E-09	0,000	2,9E-09	0,000	0,000	0,000
	4	28,220	0,035	3,8E-11	0,000	2,6E-10	0,000	0,000	0,000
	5	126,718	0,008	1,2E-10	0,000	8,8E-11	0,000	0,000	0,000
	6	134,610	0,007	3,8E-08	0,000	8,8E-01	0,404	0,000	1,526
	7	134,638	0,007	8,8E-01	0,404	3,6E-08	0,000	1,526	0,000

NF_123	9	148,925	0,007	3,3E-08	0,000	5,5E-08	0,000	0,000	0,000
	10	149,026	0,007	5,0E-04	0,000	3,0E-07	0,000	-0,027	0,001
	11	149,117	0,007	3,1E-07	0,000	5,2E-04	0,000	-0,001	-0,027
	12	150,371	0,007	2,4E-07	0,000	1,7E-07	0,000	0,000	0,000
	13	153,677	0,007	3,9E-03	0,002	3,9E-01	0,178	-0,063	0,630
	14	153,684	0,007	3,9E-01	0,177	3,9E-03	0,002	0,631	0,063
	15	155,363	0,006	7,8E-07	0,000	1,0E-06	0,000	0,001	0,001

NF_36	1	2,117	0,472	2,3E+01	6,887	3,1E+02	93,066	-0,254	0,932
	2	2,117	0,472	3,1E+02	93,066	2,3E+01	6,887	0,932	0,254

Table A.2 Dynamic Characteristics With Mass (Cont.)

	3	16,978	0,059	3,6E-09	0,000	4,0E-09	0,000	0,000	0,000
	4	28,220	0,035	4,0E-11	0,000	2,7E-10	0,000	0,000	0,000
	5	126,718	0,008	1,2E-10	0,000	8,8E-11	0,000	0,000	0,000
	6	134,610	0,007	3,9E-08	0,000	8,8E-01	0,263	0,000	1,527
	7	134,637	0,007	8,8E-01	0,263	3,7E-08	0,000	1,527	0,000



APPENDIX B. Data of Pushover Curve and Capacity Spectrum

In this part, tables not only shows the base shear force versus roof displacement obtained by pushover analysis of frames but also their relative spectrum capacity curve calculated follow ACT 40 (1996).

Table B.1. Data of Pushover Curve and Capacity Spectrum of CF and NF

CF			
Δ_{roof}	V	S_d	S_a
(mm)	(kN)	(mm)	(g)
0,000	0,000	0,000	0,000
3,643	118,112	3,632	0,055
3,833	99,778	3,822	0,047
3,870	96,611	3,859	0,045
4,664	114,314	4,650	0,053
5,350	123,414	5,335	0,058
6,094	129,622	6,077	0,060
6,908	134,812	6,888	0,063
7,556	139,226	7,534	0,065
8,346	143,732	8,323	0,067
8,882	145,196	8,857	0,068
9,542	145,695	9,515	0,068
11,113	149,493	11,082	0,070
11,961	151,664	11,928	0,071
12,356	151,295	12,321	0,071
13,673	153,076	13,635	0,071
14,538	154,300	14,497	0,072
15,660	154,979	15,616	0,072
16,350	155,504	16,304	0,073
17,518	156,296	17,469	0,073
18,165	156,578	18,114	0,073
18,971	156,898	18,918	0,073
19,953	156,979	19,897	0,073
20,540	156,787	20,482	0,073
20,977	156,770	20,918	0,073
22,072	156,646	22,010	0,073
22,629	156,624	22,566	0,073
23,718	156,676	23,651	0,073

NF			
Δ_{roof}	V	S_d	S_a
(mm)	(kN)	(mm)	(g)
0,000	0,000	0,000	0,000
0,554	14,597	0,594	0,007
1,188	30,989	1,273	0,016
1,826	43,499	1,958	0,022
2,443	53,791	2,619	0,027
3,087	63,675	3,310	0,032
3,767	74,256	4,038	0,037
4,445	81,628	4,765	0,041
5,045	85,580	5,408	0,043
5,589	89,378	5,991	0,045
6,198	93,181	6,644	0,047
6,905	98,736	7,401	0,049
7,577	103,345	8,122	0,052
8,167	105,298	8,754	0,053
8,707	105,636	9,333	0,053
9,367	108,088	10,041	0,054
10,092	110,628	10,818	0,055
10,846	114,149	11,626	0,057
11,583	117,027	12,416	0,059
12,208	117,968	13,086	0,059
12,803	119,605	13,724	0,060
13,443	120,936	14,410	0,061
14,059	121,583	15,070	0,061
14,756	122,921	15,818	0,062
15,464	124,546	16,576	0,062
16,015	124,821	17,167	0,063
16,634	126,136	17,830	0,063
17,318	127,405	18,564	0,064

Table B.1. Data of Pushover Curve and Capacity Spectrum (Cont.)

25,137	156,882	25,066	0,073	18,037	128,785	19,334	0,065
26,249	156,968	26,175	0,073	18,727	129,831	20,074	0,065
26,855	156,687	26,779	0,073	19,438	131,049	20,837	0,066
27,910	156,505	27,831	0,073	20,187	131,849	21,639	0,066
29,406	155,590	29,323	0,073	20,912	132,332	22,417	0,066
31,121	155,014	31,034	0,072	21,507	132,644	23,054	0,066
32,902	154,467	32,809	0,072	22,233	132,857	23,833	0,067
33,337	154,191	33,243	0,072	22,940	133,264	24,590	0,067
33,886	153,474	33,790	0,072	23,683	133,595	25,387	0,067
34,486	152,315	34,388	0,071	24,343	133,775	26,094	0,067
35,233	151,570	35,134	0,071	25,074	134,289	26,877	0,067
35,962	150,751	35,861	0,070	25,664	134,397	27,510	0,067
37,890	149,425	37,783	0,070	26,346	134,499	28,241	0,067
39,038	148,727	38,928	0,069	27,082	134,852	29,030	0,068
39,297	148,550	39,186	0,069	27,706	134,580	29,698	0,067
41,063	146,962	40,948	0,069	28,387	134,702	30,429	0,068
41,840	146,101	41,722	0,068	29,101	134,509	31,194	0,067
46,383	140,442	46,253	0,066	29,813	134,628	31,957	0,067
47,070	139,472	46,937	0,065	39,431	132,387	42,267	0,066
47,892	138,463	47,757	0,065	40,137	131,718	43,025	0,066
49,108	136,919	48,970	0,064	40,858	130,760	43,796	0,066
50,269	135,377	50,127	0,063	42,330	129,488	45,374	0,065
51,008	134,227	50,864	0,063	43,037	128,915	46,132	0,065
51,440	133,579	51,295	0,062	46,638	126,038	49,993	0,063
52,244	132,370	52,097	0,062	47,342	125,491	50,747	0,063
52,629	131,722	52,481	0,061	48,079	124,920	51,537	0,063
53,216	130,963	53,067	0,061	58,856	116,167	63,090	0,058
53,930	129,926	53,778	0,061	59,509	115,277	63,790	0,058
54,557	129,016	54,404	0,060	60,186	114,823	64,515	0,058
55,254	128,057	55,098	0,060	60,865	114,552	65,243	0,057
56,155	126,923	55,997	0,059	67,284	108,822	72,124	0,055
57,134	125,776	56,973	0,059	68,016	108,246	72,908	0,054
58,159	124,534	57,995	0,058	68,750	107,672	73,695	0,054

Table B.2. Data of Pushover Curve and Capacity Spectrum of CF_123 and NF_123

CF_123			
Δ_{roof}	V	S_d	S_a
(mm)	(kN)	(mm)	(g)
0,000	0,000	0,000	0,000
3,651	113,494	3,637	0,094
3,832	96,508	3,817	0,080
3,916	96,853	3,901	0,081
4,886	111,190	4,866	0,092
5,426	112,617	5,405	0,094
5,921	114,167	5,898	0,095
7,002	118,112	6,975	0,098
8,016	117,499	7,985	0,098
8,935	120,088	8,900	0,100
9,558	121,285	9,521	0,101
10,378	121,266	10,337	0,101
10,975	120,806	10,932	0,100
12,629	119,974	12,580	0,100
13,852	120,343	13,797	0,100
15,043	121,054	14,984	0,101
15,941	121,005	15,879	0,101
17,038	121,026	16,971	0,101
18,160	121,161	18,089	0,101
18,543	121,215	18,471	0,101
19,177	121,281	19,102	0,101
19,546	121,084	19,470	0,101
20,039	120,442	19,961	0,100
21,746	119,241	21,661	0,099
22,561	119,100	22,473	0,099
27,017	117,655	26,912	0,098
28,284	117,401	28,173	0,098
29,121	117,082	29,007	0,097
29,450	116,711	29,335	0,097
29,784	116,281	29,668	0,097
30,209	115,887	30,091	0,096
30,874	115,767	30,753	0,096
33,695	114,958	33,563	0,096
35,254	114,574	35,117	0,095
36,151	114,279	36,009	0,095

NF_123			
Δ_{roof}	V	S_d	S_a
(mm)	(kN)	(mm)	(g)
0,000	0,000	0,000	0,000
0,284	7,520	0,305	0,007
0,602	15,784	0,645	0,014
0,919	23,632	0,985	0,021
1,236	31,467	1,325	0,028
2,571	56,344	2,757	0,050
2,862	61,050	3,070	0,054
3,221	66,072	3,454	0,059
3,565	71,189	3,824	0,064
3,941	74,615	4,226	0,067
4,290	79,734	4,601	0,071
4,641	83,999	4,978	0,075
7,583	93,511	8,132	0,083
7,946	95,205	8,521	0,085
8,321	94,905	8,924	0,085
8,677	96,324	9,305	0,086
9,044	97,467	9,699	0,087
9,403	98,611	10,084	0,088
9,778	99,838	10,486	0,089
11,222	101,944	12,035	0,091
11,594	102,704	12,433	0,092
11,967	103,593	12,834	0,092
12,339	104,377	13,233	0,093
12,714	104,550	13,635	0,093
13,080	105,088	14,027	0,094
13,446	105,298	14,420	0,094
14,925	106,793	16,006	0,095
15,293	106,792	16,400	0,095
15,664	107,286	16,798	0,096
16,038	107,268	17,200	0,096
16,410	107,663	17,598	0,096
16,765	107,705	17,980	0,096
17,117	108,013	18,357	0,096
17,483	108,294	18,749	0,097
17,846	108,415	19,139	0,097

Table B.2. Data of Pushover Curve and Capacity Spectrum of CF_123 and NF_123 (Cont.)

41,653	111,725	41,490	0,093
42,294	111,516	42,129	0,093
42,936	111,382	42,768	0,093
44,439	111,142	44,266	0,092
45,756	110,705	45,577	0,092
46,331	110,244	46,150	0,092
46,655	109,877	46,473	0,091
47,094	109,132	46,910	0,091
47,450	108,649	47,264	0,090
48,224	108,199	48,035	0,090
49,044	108,090	48,852	0,090
49,608	107,949	49,414	0,090
50,785	107,624	50,587	0,089
51,711	107,238	51,509	0,089
52,173	107,031	51,969	0,089
52,844	106,679	52,638	0,089
53,527	106,372	53,318	0,088
60,158	103,115	59,923	0,086
60,793	102,371	60,556	0,085
61,606	101,971	61,365	0,085
64,830	100,452	64,577	0,084
66,902	99,162	66,641	0,082
69,042	98,493	68,773	0,082
70,170	97,995	69,895	0,081
70,639	97,788	70,363	0,081
71,767	96,980	71,487	0,081

18,213	108,691	19,532	0,097
18,583	108,962	19,929	0,097
18,946	109,018	20,318	0,097
19,303	109,251	20,701	0,098
19,666	109,506	21,090	0,098
20,007	109,442	21,456	0,098
20,374	109,149	21,850	0,097
20,738	108,442	22,240	0,097
21,102	107,825	22,630	0,096
21,467	107,471	23,022	0,096
21,833	107,237	23,414	0,096
24,759	105,771	26,552	0,094
28,426	104,166	30,485	0,093
35,672	101,171	38,255	0,090
36,014	101,034	38,622	0,090
36,375	100,884	39,009	0,090
41,155	98,660	44,136	0,088
41,523	98,499	44,530	0,088
46,277	96,301	49,629	0,086
46,645	96,129	50,023	0,086
47,742	95,603	51,199	0,085
48,109	95,430	51,594	0,085
53,538	92,860	57,415	0,083
62,291	88,328	66,803	0,079
63,761	87,617	68,379	0,078
64,128	87,440	68,773	0,078

Table B.3. Data of Pushover Curve and Capacity Spectrum of CF_336 and NF_336

CF_336			
Δ_{roof}	V	S_d	S_a
(mm)	(kN)	(mm)	(g)
0,000	0,000	0,000	0,000
3,662	115,707	3,653	0,035
3,873	95,342	3,864	0,029
4,776	114,645	4,765	0,035
5,660	126,911	5,647	0,038

NF_336			
Δ_{roof}	V	S_d	S_a
(mm)	(kN)	(mm)	(g)
0,000	0,000	0,000	0,000
0,574	14,622	0,615	0,005
2,537	54,333	2,720	0,018
3,224	64,868	3,457	0,021
3,901	74,200	4,184	0,024

Table B.3. Data of Pushover Curve and Capacity Spectrum of CF_336 and NF_336 (Cont.)

6,417	133,747	6,402	0,041
6,931	138,461	6,915	0,042
7,597	145,323	7,580	0,044
8,262	150,539	8,242	0,046
8,876	155,001	8,855	0,047
9,649	160,310	9,627	0,049
10,599	163,810	10,574	0,050
11,463	168,649	11,436	0,051
12,508	173,374	12,479	0,053
13,333	177,232	13,302	0,054
14,587	180,036	14,553	0,055
15,469	182,139	15,433	0,055
16,221	183,905	16,183	0,056
16,553	184,115	16,514	0,056
17,240	184,577	17,200	0,056
17,943	185,252	17,902	0,056
18,643	186,331	18,599	0,057
19,027	187,017	18,983	0,057
20,117	188,692	20,070	0,057
20,599	189,169	20,551	0,057
21,407	189,251	21,357	0,057
22,109	189,448	22,057	0,057
22,803	189,659	22,750	0,058
24,271	190,096	24,215	0,058
25,610	190,686	25,551	0,058
26,947	191,058	26,884	0,058
28,091	191,335	28,026	0,058
29,284	191,560	29,216	0,058
30,205	191,698	30,135	0,058
31,286	191,682	31,213	0,058
33,654	190,368	33,576	0,058
34,800	189,470	34,720	0,057
36,653	187,545	36,568	0,057
38,197	185,643	38,108	0,056
38,816	184,734	38,726	0,056
39,655	183,544	39,562	0,056
40,915	181,595	40,819	0,055
41,736	180,167	41,639	0,055

6,462	92,726	6,930	0,030
7,133	96,464	7,650	0,031
7,840	101,920	8,408	0,033
8,481	104,006	9,095	0,034
9,086	106,023	9,745	0,035
11,703	117,348	12,551	0,038
12,308	119,696	13,200	0,039
12,917	123,114	13,852	0,040
13,637	126,013	14,624	0,041
15,642	131,426	16,775	0,043
16,359	133,076	17,544	0,043
16,989	135,118	18,219	0,044
17,651	137,178	18,929	0,045
18,291	138,745	19,616	0,045
18,985	141,045	20,360	0,046
19,661	143,115	21,085	0,047
20,246	144,442	21,712	0,047
20,905	145,964	22,419	0,048
21,556	146,903	23,118	0,048
22,824	147,753	24,477	0,048
23,432	148,317	25,129	0,048
24,139	149,304	25,888	0,049
24,804	150,322	26,601	0,049
25,543	151,204	27,393	0,049
26,278	151,619	28,181	0,049
27,737	153,101	29,746	0,050
28,400	153,654	30,457	0,050
29,031	154,208	31,134	0,050
29,765	154,737	31,921	0,050
30,392	155,094	32,593	0,050
31,000	155,090	33,245	0,050
31,662	155,450	33,955	0,051
32,396	155,640	34,742	0,051
33,131	155,936	35,530	0,051
33,730	155,909	36,173	0,051
34,360	155,809	36,849	0,051
35,076	155,727	37,616	0,051
35,794	155,582	38,387	0,051

Table B.3. Data of Pushover Curve and Capacity Spectrum of CF_336 and NF_336 (Cont.)

43,301	177,518	43,201	0,054
44,076	175,852	43,973	0,053
44,929	174,006	44,824	0,053
45,368	173,100	45,263	0,052
45,813	172,073	45,706	0,052
46,124	171,313	46,016	0,052
46,688	169,936	46,579	0,052
47,765	167,729	47,654	0,051
48,354	166,508	48,242	0,050
48,895	165,197	48,782	0,050
49,277	163,574	49,162	0,050
49,706	161,938	49,591	0,049
50,084	160,760	49,968	0,049
50,625	159,344	50,507	0,048
51,143	157,962	51,024	0,048
51,581	156,384	51,461	0,047
52,047	154,535	51,926	0,047
52,457	153,153	52,335	0,046

36,458	155,416	39,098	0,051
37,115	155,125	39,803	0,051
37,822	154,730	40,561	0,050
38,524	154,283	41,314	0,050
39,221	153,917	42,062	0,050
39,964	153,665	42,858	0,050
40,541	153,427	43,478	0,050
41,173	152,873	44,155	0,050
41,892	152,065	44,926	0,050
42,446	151,465	45,520	0,049
43,156	150,984	46,282	0,049
47,869	145,657	51,336	0,047
48,580	144,982	52,099	0,047
49,287	144,110	52,856	0,047
53,851	137,851	57,752	0,045
54,575	136,873	58,528	0,045
61,292	125,586	65,731	0,041
61,966	123,484	66,454	0,040

Table B.4. Data of Pushover Curve and Capacity Spectrum of NF_5TEETH

NF_5TEETH			
Δ_{roof}	V	S_d	S_a
(mm)	kN	mm	g
0,000	0,000	0,000	0,000
2,256	58,538	2,418	0,029
5,789	113,185	6,205	0,057
7,070	125,340	7,578	0,063
8,062	131,562	8,642	0,066
9,174	136,744	9,834	0,069
9,846	138,783	10,555	0,070
10,666	140,128	11,433	0,070
11,691	143,267	12,532	0,072
12,628	145,846	13,536	0,073
13,990	150,014	14,996	0,075
15,031	152,092	16,113	0,076

Table B.4. Data of Pushover Curve and Capacity Spectrum of NF_5TEETH (Cont.)

15,948	153,546	17,095	0,077
16,894	155,266	18,109	0,078
17,789	156,769	19,068	0,079
18,927	158,288	20,288	0,079
19,869	159,563	21,299	0,080
21,156	160,915	22,678	0,081
21,980	160,989	23,561	0,081
23,870	161,771	25,586	0,081
25,055	162,037	26,857	0,081
26,692	162,516	28,612	0,081
28,613	162,682	30,671	0,082
30,109	162,242	32,275	0,081
31,799	161,973	34,087	0,081
32,653	161,164	35,001	0,081
33,703	160,819	36,127	0,081
35,124	159,964	37,650	0,080
37,172	158,856	39,846	0,080
39,454	156,749	42,292	0,079
41,340	154,533	44,313	0,077
42,541	152,798	45,601	0,077
43,481	151,467	46,609	0,076
45,063	149,304	48,304	0,075
46,439	147,469	49,779	0,074
47,678	145,911	51,107	0,073
48,934	143,985	52,454	0,072
49,679	142,814	53,252	0,072
50,547	141,441	54,183	0,071
50,998	139,860	54,666	0,070

Besides that, the pushover results of NF strengthened using different ratio of shear connectors are also added herein.

Table B.5. Data of Pushover Curves of NF_014, NF_028, and NF_062

NF_014		NF_028		NF_062	
Δ_{roof}	V	Δ_{roof}	V	Δ_{roof}	V
(mm)	(kN)	(mm)	(kN)	(mm)	(kN)
0,000	0,000	0,000	0,000	0,000	0,000
0,158	3,937	2,670	62,215	2,604	61,847
0,158	3,937	5,391	100,492	4,917	97,095
3,939	82,978	6,148	106,096	5,887	106,879
4,914	96,251	8,030	119,512	7,017	115,695
5,484	104,224	8,957	123,288	10,206	132,481
5,542	104,037	9,779	125,490	11,521	136,695
5,800	106,687	10,634	128,689	12,626	140,270
8,689	126,202	11,798	132,069	13,699	143,574
11,949	134,204	12,611	134,087	15,022	146,029
12,002	134,235	13,556	137,005	16,246	147,895
12,105	134,484	14,942	141,228	17,561	149,702
13,798	136,983	17,224	144,317	18,672	150,798
23,428	146,666	18,371	145,547	20,088	152,152
23,826	147,061	20,221	147,430	21,819	152,966
26,446	148,212	21,929	148,628	23,227	154,334
26,557	148,277	23,582	149,222	25,246	153,493
26,702	148,003	27,035	150,384	36,590	149,090
26,914	148,126	34,698	145,554	42,087	147,699
26,933	148,100	40,495	142,992	43,652	146,755
27,161	148,177	45,737	140,468	46,880	145,674
27,422	148,173	47,388	139,246	49,170	145,261
27,683	148,304	49,104	138,365	50,632	144,690
28,230	147,589	52,328	136,544	54,552	143,194
28,501	147,449	53,683	135,631	56,267	142,149
29,142	146,523	55,352	134,565	61,662	139,928
29,410	146,346	57,624	133,295	64,294	138,514
31,751	144,939	60,981	131,592	65,848	137,778
31,858	144,830	62,317	129,594	67,845	136,506
32,251	144,630	65,892	127,833	70,610	135,144
32,387	144,546	68,071	126,476	74,073	132,511
79,331	114,225	71,976	124,807	76,777	130,292
79,377	113,925	74,145	123,209	79,454	127,913
79,830	113,715	77,171	121,092	81,370	125,458
80,001	113,474	79,702	118,891	84,603	123,329

RESUME

Name Surname : Quy Thue NGUYEN
Birth Place and Date : Vietnam / November 10, 1988
Foreign Language : English, Turkish

Educational Status (Institution and Year)

High school : THOAI NGOC HAU High School
(2003-2006)

Undergraduate : HCMC University of Transport,
Faculty of Construction Engineering
(2007-2012)

Institution / Organization and Year of Work : HCMC University of Transport,
Faculty of Construction Engineering
(2012-2015)

Contact (email) : nguyenthuequy@gmail.com

Publications :

Serhatoğlu, C., Nguyen, Q.T., Livaoğlu, R. 2018. Natural Characteristics and Nonlinear Behavior of a New RC Mold System. *Anadolu University Journal of Science and Technology B-Theoretical Sciences*, IN PRINT.

Serhatoğlu, C., Nguyen, Q.T., Livaoğlu, R. 2017. New Integrated Mold System Designed For Reinforced Concrete Structures. 4th International Conference on Earthquake Engineering and Seismology, 11-13 October 2017, Anadolu University, Eskişehir.